Draft version May 25, 2026
Typeset using LaTeX **twocolumn** style in AASTeX631

GWTC-5.0: Population Properties of Merging Compact Binaries

The LIGO Scientific Collaboration, the Virgo Collaboration, and the KAGRA Collaboration

ABSTRACT

We present the population properties of merging compact binaries inferred using 267 mergers from the cumulative Gravitational-Wave Transient Catalog 5.0. As this data set contains no new sources with a neutron star, we primarily focus on the properties of the binary black hole mergers. We infer the merger rate of binary black holes with component masses between $2.5\,M_\odot$ and $200\,M_\odot$ to be 27.5–49.4 $\mathrm{Gpc^{-3}\,yr^{-1}}$ (all intervals at 90% credible levels) at redshift $z = 0.2$. We find evidence for a subpopulation of binary black hole mergers that host a rapidly spinning black hole (dimensionless spins $\chi \sim 0.7$), consistent with signatures of hierarchical mergers. We find that these occur at two mass scales, the first at primary masses $\sim$ 10–20 $M_\odot$ and the second above $\sim 45\,M_\odot$, and we estimate their total rate at $z = 0.2$ to be 0.2–3.11 $\mathrm{Gpc^{-3}yr^{-1}}$. We infer that, above $40\,M_\odot$, the mass distribution of the less massive (secondary) black hole declines more steeply than that of the more massive (primary) one. This is consistent with a flatter mass-ratio distribution and indicates the prevalence of unequal-mass binaries with large primary masses. We find evidence for two features in the black hole mass spectrum: a peak around $10\,M_\odot$ and a change of slope at around $35\,M_\odot$. Black holes of $\sim 35\,M_\odot$ pair preferentially with companions of similar mass. Additionally, we find that the effective inspiral spin distribution of binary black holes is asymmetric about zero, based on which we infer that at least 9% of mergers occur in channels with some preference for spin-orbit alignment. We find evidence that the effective inspiral spin distribution is broader for unequal-mass binaries and that it also likely broadens with increasing redshift. Overall, our results support the presence of multiple subpopulations of merging black holes that can potentially arise from different formation pathways.

Keywords: KEYWORDS

1. INTRODUCTION

With LIGO (Aasi et al. 2015), Virgo (Acernese et al. 2015), and KAGRA (Akutsu et al. 2021) increasing in sensitivity over the last decade, the number of gravitational wave (GW) detections has rapidly increased and, with it, our ability to study the population of merging black holes (BHs) and neutron stars (NSs). This paper updates our inference on such populations with the latest iteration of the LIGO–Virgo–KAGRA Collaboration (LVK) transient catalog, GWTC-5.0 (Abac et al. 2026a,b), which includes data through the second part of the fourth observing run (O4b).

We analyze sources in GWTC-5.0 with false alarm rate (FAR) $< 1\,\mathrm{yr^{-1}}$ ($< 0.25\,\mathrm{yr^{-1}}$ for systems with NSs, see Sec. 2) using hierarchical Bayesian inference (Sec. 3). In O4b, 104 new binary BH (BBH) systems were detected with sufficient significance to be included in our population inferences. Furthermore, two new sources with sufficient significance from the first part of the fourth observing run (O4a) are also included following reanalysis (see App. A of Abac et al. 2026b). This brings the total number of detected compact binary mergers considered in this paper to 267, up from 161 reported in Abac et al. (2025a). No new NS–BH binaries (NSBHs) or binary NSs (BNSs) of sufficient significance were detected. The increased catalog size enables more robust population inference using both weakly and strongly-parameterized models; we list some key findings below. Throughout this paper, we denote the more massive and less massive compact object in the binary as primary (subscript 1) and secondary (subscript 2), respectively. All results are quoted at a symmetric 90% credible level unless stated otherwise.

1. **The inferred distribution of BBH systems is broadly consistent with previous results from Abac et al. (2025a) based on GWTC-4.0 (Sec. 4).** We find reduced evidence for the previously reported mass-ratio peak at $q \approx 0.7$, where $q = m_2/m_1$, and instead find a preference for equal masses. Spin measurements continue to indicate that most BBH mergers have non-extremal spins, with 69–84% of BHs inferred to have

Corresponding author: LSC P&P Committee, via LVK Publications as proxy
lvc.publications@ligo.org

dimensionless spin magnitudes $\chi \leq 0.5$. The effective inspiral spin ($\chi_{\rm eff}$, Racine 2008) distribution peaks near zero but is asymmetric, from which we infer that at least 9% of BBH mergers originate in formation channels with some degree of spin–orbit alignment. On the other hand, 30–46% have $\chi_{\rm eff} < 0$ indicating contributions from formation channels that can produce spins anti-aligned with the orbital angular momentum. In Sec. 4.4.4, we show that the larger dataset yields a more precise estimate of the BBH merger rate that remains statistically consistent with Abac et al. (2025a).

2. **We continue to find features in the BBH mass spectrum, at $\sim$10 $M_\odot$ and $\sim$35 $M_\odot$ in primary mass (Secs. 5 and 6).** We find less-clear, model-dependent evidence that the former contains a significant subpopulation of mergers with mass ratios peaking around $q \approx 0.7$. We find reduced support for the interpretation that the $\sim$35 $M_\odot$ feature represents a local peak in the distribution. Instead, we find it to be more consistent with a change in slope in both primary- and secondary-mass distributions. Binaries with $m_1 \approx 35\,M_\odot$ possibly have a preference for equal-mass pairing, and a $\chi_{\rm eff}$ distribution that peaks at or near zero.

3. **Binaries with $m_1 \gtrsim 40\,M_\odot$ likely have a different mass-ratio distribution than the rest of the population (Sec. 7).** The distribution of m_2 has a significantly sharper drop than m_1 at $\gtrsim 40\,M_\odot$, consistent with a flatter mass-ratio distribution for BBH mergers with $m_1 \gtrsim 40\,M_\odot$. Combined with the observed change in spin properties at that mass (Sec. 8), this shift in the mass-ratio distribution might indicate the presence of formation mechanisms like hierarchical mergers.

4. **We find evidence for a subset of BBH mergers with at least one rapidly-spinning BH (Sec. 4.4.3 and Sec. 8)**, using models of varying degrees of flexibility. With models motivated by the physics of hierarchical mergers in dense stellar clusters (Antonini et al. 2025), we locate the rapidly-spinning BBH mergers at two mass ranges: the first at $10\,M_\odot \leq m_1 \leq 20\,M_\odot$ and the second at $m_1 \gtrsim 45\,M_\odot$. We infer a merger rate density of 0.2–3.11 $\mathrm{Gpc^{-3}yr^{-1}}$ at redshift $z = 0.2$ for the rapidly-spinning BBH mergers.

5. **The width of the $\chi_{\rm eff}$ distribution likely exhibits correlations with other BBH properties (Sec. 9).** We find increased evidence that the structure of the joint q–$\chi_{\rm eff}$ distribution is driven more by the changing width of the $\chi_{\rm eff}$ distribution with mass ratio rather than by the changing mean. Concurrently, we still find that the $\chi_{\rm eff}$ distribution likely also broadens with redshift. The details of the broadening exhibit some degree of model dependence, suggesting that the structure of the correlation is complex.

Altogether, our analysis of GWTC-5.0 supports the presence of multiple BBH subpopulations, loosely defined as a subset of the population with some properties that are clearly distinct from the rest, and the possibility of multiple formation pathways contributing to the observed population. The rest of the paper presents details of the analyses and the results, followed by a short forward-looking summary in Sec. 10.

2. DATASET

This section describes the selection criteria used to include candidates in the population analyses of this paper, and how samples from their posterior distributions were produced. See also Abac et al. (2025a), which we closely follow.

2.1. *Data Collection*

We analyze compact binary coalescence (CBC) candidates from the cumulative GWTC-5.0 (Abac et al. 2026b), which includes previously reported GW events (Abbott et al. 2023a, 2021a, 2019) and new compact binary candidates from O4b and the 16th engineering run (ER16) preceding O4b (Abac et al. 2026a,b). We exclude ER16 data in our analyses to avoid potential human-selection bias; one candidate meeting our significance selection criteria, GW240406_062847, is thus omitted.

The candidates are statistically significant triggers identified by the template-based matched-filter analyses GstLAL (Messick et al. 2017; Sachdev et al. 2019; Hanna et al. 2020; Cannon et al. 2021; Ewing et al. 2024; Tsukada et al. 2023; Sakon et al. 2024; Ray et al. 2023; Joshi et al. 2025a,b), MBTA (Adams et al. 2016; Aubin et al. 2021; Andres et al. 2022; Alléné et al. 2025), and PyCBC (Usman et al. 2016; Nitz et al. 2017, 2018; Dal Canton et al. 2021), as well as the weakly modeled excess-power search performed by the cWB pipeline (Klimenko et al. 2005, 2008, 2016; Mishra et al. 2025; Abac et al. 2026c). Details of the detector instrumentation, network sensitivity, and data quality for O4b are described in Abac et al. (2026a). More details of the search algorithms and the their configuration are described in Abac et al. (2026c). The new candidates and corresponding search sensitivities are presented in Abac et al. (2026b).

2.2. *Event Selection*

Not all events from GWTC-5.0 are included here, as its statistical threshold is generally less stringent than that required for population inference (Abac et al. 2026b). To limit contamination from noise triggers, we impose a significance threshold for population analyses (Abbott et al. 2021b, 2023b; Abac et al. 2025a). Specifically, we require a FAR $< 1\,\mathrm{yr^{-1}}$ in at least one search pipeline for BBH-only analyses. Analyses that include both NSs and BHs are subject to a threshold FAR $< 0.25\,\mathrm{yr^{-1}}$ (Sec. 4). These criteria yield 267 (242) CBC candidates in GWTC-5.0 with FAR below $1\,\mathrm{yr^{-1}}$ ($0.25\,\mathrm{yr^{-1}}$), of which 104 (94) are identified in O4b. Due to catalog updates (App. A of Abac et al. 2026b), our 267 candidates below $1\,\mathrm{yr^{-1}}$ include 2 additional O4a events compared to Abac et al. (2025a), while our 242 candidates below $0.25\,\mathrm{yr^{-1}}$ include 4 additional O4a events whose FAR estimates were revised from above to below $0.25\,\mathrm{yr^{-1}}$.

Assuming statistically independent noise triggers, the expected number of triggers with FAR $<$ FAR$_{\rm threshold}$that are actually noise events can be estimated as (Farr et al. 2015; Ray et al. 2023) $N_{\rm noise} = \sum_k {\rm FAR}_{\rm threshold} \times T_k$ where T_k is an estimate of the time examined by the k-th search. For a threshold of 1 yr^{-1}, we expect $N_{\rm noise} \approx 9.6$ since the first observing run (O1) through O4b.

The O4b sample includes several notable BBH candidates new to population analyses, namely the high-signal-to-noise ratio (SNR) events GW250114_082203 (Abac et al. 2025b), GW240925_005809 and GW250207_115645 (Abac et al. 2026), as well as the high-spin systems GW241011_233834 (henceforth GW241011) and GW241110_124123 (henceforth GW241110) (Abac et al. 2025c). No new candidates involving NSs satisfy our selection criteria in GWTC-5.0.

Population inference requires consistent modeling of selection effects (see Sec. 3); we therefore exclude candidates from independent analyses (Venumadhav et al. 2019, 2020; Olsen et al. 2022; Mehta et al. 2025a; Wadekar et al. 2023; Zackay et al. 2019; Nitz et al. 2019, 2020, 2021, 2023; Kumar & Dent 2024; Mishra et al. 2025; Koloniari et al. 2025; Niu et al. 2025), which may alter the conclusions (Mehta et al. 2025b).

2.3. *Source Inference*

Posterior samples and associated simulation products used in this work are obtained from Abac et al. (2026b), with the analysis configurations described in Abac et al. (2026c). We employ Bayesian inference to generate posterior samples for each detection candidate, conditioned on the observed strain data and assumed signal and noise models (Thrane & Talbot 2019; Abac et al. 2026c).

The waveform choices employed by our analyses are detailed in App. A.1. All the waveforms we use are constructed for quasi-circular binary orbits and our analyses neglect orbital eccentricity in both source modeling and selection-function calculations. Although nonzero eccentricity has been claimed for some GW candidates (Romero-Shaw et al. 2020a; Gayathri et al. 2022; Romero-Shaw et al. 2022a; Gamba et al. 2023; Fei & Yang 2024; Gupte et al. 2025; McMillin et al. 2025; Planas et al. 2025; Morras et al. 2025; Jan et al. 2026; Phukon et al. 2025; Abbott et al. 2021c), conclusions about eccentricity in the literature vary (Romero-Shaw et al. 2019; Wu et al. 2020; Lenon et al. 2020; O'Shea & Kumar 2023; Iglesias et al. 2024; Ramos-Buades et al. 2023b; Bonino et al. 2023; Gamboa et al. 2025; Xu et al. 2025; Gupte et al. 2026; Abac et al. 2025b,c) and eccentricity is not incorporated in the GWTC-5.0 parameter-estimation products. All posterior samples are reweighted to a prior uniform in comoving volume and source-frame time following App. C of Abbott et al. (2021a).

3. METHODS

Population inference of GW sources is based on the framework of hierarchical Bayesian inference. Three main ingredients are needed for this method: posterior samples for each of the sources in the catalog, a method for calculating the selection effects of the detector network, and a model for the distribution of population parameters. With the assumptions of a Poisson process for the source population and that the data from each event are statistically independent, the population likelihood—i.e., the likelihood of all source-containing data—is

$$p(\{d_i\}|\Lambda) \propto N(\Lambda)^{N_{\rm obs}} e^{-\xi(\Lambda)N(\Lambda)} \prod_{i=1}^{N_{\rm obs}} \int {\rm d}\theta \, p(d_i|\theta) \, p(\theta|\Lambda) \, . \quad (1)$$

Details on this likelihood, including a full derivation, can be found in , e.g., Loredo & Lamb (2002); Farr et al. (2015); Mandel et al. (2019); Vitale et al. (2022); here we briefly describe its main elements.

Beginning with the integrand, for any given source, θ are the GW source parameters, such as masses, spins, redshift and orientation (Abbott et al. 2016). The last term, $p(\theta|\Lambda)$ is our model for the astrophysical distribution of source parameters, parametrized by a set of hyperparameters Λ, in whose values we are ultimately interested. For each source i, $p(d_i|\theta)$ is the likelihood of the corresponding stretch of data, usually estimated by Monte Carlo reweighing and importance sampling of precomputed posterior draws (cf. Sec. 2.3).

The prefactor to the integral accounts for selection effects; it depends on $N(\Lambda)$, which is the Poisson rate parameter controlling the total number of sources that merged over the data-taking period. Of those, $N_{\rm obs}$ were actually observed. Given an astrophysical model for the population, the fraction of sources expected to be detected is $\xi(\Lambda)$, which we numerically estimate by reweighting a large set of detectable simulated sources (App. A.2 and Tiwari 2018). In general, a higher number of such simulated sources is desired to reduce the uncertainty in the estimation of the instruments' selection effects, and hence in the population likelihood (Tiwari 2018; Talbot & Golomb 2023; Farr 2019; Essick & Farr 2022; Heinzel & Vitale 2025). Unless stated otherwise, throughout this work, we require a maximum variance of 1 on the population likelihood estimator; for some models, we also show results with a more relaxed variance cut in App. B. This is implemented as a sharp or smoothly-tapered cutoff (e.g., Callister & Farr 2024).

Following our previous work (Abac et al. 2025a), we employ two broad classes of population models. We use *strongly-parameterized* models where $p(\theta|\Lambda)$ is written as the product of compact generally-analytical distributions, e.g., combinations of power laws and Gaussians. Within this framework, we can allow for correlations between parameters by directly modeling their joint distributions rather than the marginals. Stronger models make rigid assumptions (e.g., that a distribution is Gaussian) that can yield narrower posteriors. However, when the model is a poor match to the data, they can be prone to systematic errors that are sometimes hard to uncover (Romero-Shaw et al. 2022b; Miller et al. 2026; Alvarez-Lopez et al. 2025; Cheng et al. 2023).

Table 1. Population models used in this work, in order of appearance. Whenever a parameter is not explicitly mentioned, it takes the value given in the "Default 1D distributions" section, following the same defaults as in Abac et al. (2025a). Strongly-parametrized models are marked with a dagger (†).

Name	Description	References
FullPop †	A model for all compact binary types (BNS, NSBH, and BBH). Uses two distinct secondary-mass-dependent pairing functions to write the joint mass distribution.	App. B.2, Farah et al. (2022), Fishbach et al. (2020), Mali & Essick (2025)
PixelPop	Measures the posterior distribution of 1 or 2 parameters as a binned Gaussian process with a smoothing hyper prior, using default 1D parametric distributions for all other parameters. For example, "(m_1, q)-PixelPop" flexibly models m_1 and q jointly, and use the default parametric 1D distributions for the rest.	App. B.1, Heinzel et al. (2025a), Heinzel et al. (2025b), Alvarez-Lopez et al. (2025)
Default BBH †	Uses the default 1D distributions for all parameters (see below).	App. B.4,Talbot & Thrane (2018); Abac et al. (2025a)
Truncated Gaussian Mixture Model (TGMM)†	Models the two component spins separately, while allowing for correlations between them using a mixture of two bivariate truncated Gaussians.	App. B.3, Hussain et al. (2026); Hussain et al. (2025)
Bivariate Skewed $\chi_{\rm eff}/\chi_{\rm p}$ †	Models the effective spins $\chi_{\rm eff}/\chi_{\rm p}$ as a bivariate skewed normal distribution truncated between -1 and 1 for $\chi_{\rm eff}$ and 0 and 1 for $\chi_{\rm p}$	App. B.6, Abbott et al. (2023a); Banagiri et al. (2025a); Miller et al. (2020)
Isolated Peak	Assumes two subpopulations. The primary mass is a normal distribution for one subpopulation ("peak") and a cubic spline for the other ("continuum"). Mass ratio, spins and redshifts are modeled as independent cubic splines, different for each subpopulation.	Godfrey et al. (2023); Abac et al. (2025a)
Binned Gaussian Process	Measures the joint distribution of 3 parameters jointly as a binned Gaussian process, coupling bins with a Gaussian process covariance, assuming an exponential quadratic kernel. Other parameters are fixed to their parameter estimation prior, except for the redshift, which is fixed to a power law $\propto (1+z)^{2.7}$.	Ray et al. (2023); Ray et al. (2025); Sridhar et al. (2025); Abac et al. (2025a)
$\chi_{\rm eff}$ Mixture, $\chi_{\rm eff}$ Three Transitions †	Parametrize $\chi_{\rm eff}$ as a mixture of a broad uniform component and a narrow. Gaussian. The branching ratio is either dependent on the primary mass via a Gaussian process prior ($\chi_{\rm eff}$ Mixture) or transitions sharply at three values of masses, measured from the data ($\chi_{\rm eff}$ Three Transitions)	App. G.1, Tong et al. (2025a); Antonini et al. (2025); Antonini et al. (2025)
Linear Correlation †	Model for $\chi_{\rm eff}$ as a truncated normal distribution whose location and standard deviation depends linearly on another parameter.	Callister et al. (2021); Biscoveanu et al. (2022a); Abbott et al. (2023b); Abac et al. (2025a)
Spline Correlation	Model $\chi_{\rm eff}$ as a truncated normal distribution whose location and standard deviation depends on another parameter via a cubic spline.	Heinzel et al. (2024); Abac et al. (2025a)
Copula Correlation †	Couple two marginal distributions into a joint distribution using a Frank copula, with a single parameter controlling the strength and sign of their correlation.	Adamcewicz & Thrane (2022); Adamcewicz et al. (2023); Abac et al. (2025a)
Three Subpopulation	Treats high-mass mergers as a subpopulation with separate spin and mass-ratio properties.	Banagiri et al. (2025b)
	Default 1D distributions	
Primary mass (m_1) †	A broken power law continuum between a minimum and maximum mass, plus two Gaussian peaks.	Talbot & Thrane (2018); Abac et al. (2025a)
Mass ratio (q) †	A power law between a mass-dependent minimum value and 1.	Talbot & Thrane (2018); Abac et al. (2025a)
Spin magnitude (χ) †	A normal distribution truncated at 0 and 1 for BBHs, or 0.4 for neutron stars in BNSs and NSBHs.	Abac et al. (2025a)
Cosine spin tilts ($\cos\theta$) †	A mixture of an isotropic component and a normal component truncated at ± 1.	Vitale et al. (2017); Vitale et al. (2022); Abac et al. (2025a)
Redshift (z) †	A simple power law, $(1+z)^{\kappa_z}$.	Fishbach et al. (2018)

We also rely on *weakly-parametrized models*, also known as agnostic models, for which all or some of the marginal distributions cannot be written in terms of simple probability distributions but are rather combinations of flexible bases such as B-splines or Gaussian processes. These allow for non-trivial correlations between parameters, usually in a way that is less prescriptive than what can be achieved with strongly-parameterized models. Typically, the extra flexibility of weakly-parameterized models comes at the expense of larger statistical uncertainties.

A list of the models used in the paper, each with a short qualitative description, is given in Tab. 1. More details are given in the works and appendices listed in the last column. We usually present results from both strongly- and weakly-parameterized models, so that modeling tradeoffs and impacts can be assessed.

A note on Figures: We report our measurements of event-level parameters by drawing posterior samples from the population hyperparameters Λ, to obtain the distribution $p(\theta|\Lambda)$. We refer to this as the posterior predictive distribution (PPD) (Abbott et al. 2023b). Most PPD plots of reconstructed populations (e.g., Fig. 2) show hatched areas corresponding to regions of the parameter space where we have under 1% of parameter estimation (PE) samples using default priors, equally weighted across all detections. This is intended as a heuristic proxy for parts of parameter space where the models may not be actively constrained by the data, and where modeling and prior choices may become particularly important. For example, the value of a power-law index may be mainly informed by a data-rich region, while the trend is extrapolated to a data-poor one. That said, regions with a dearth or absence of detections may be highly informative if the detector network is sensitive to those regions, so the hatching should not be overinterpreted.

4. POPULATION OVERVIEW

This section presents an overview of compact binary merger population properties, highlights prominent features in their global distribution, and establishes the basis for a deeper dive in the following sections.

4.1. *Full Spectrum Mass Distribution*

Figure 1 shows the median of the joint component-mass distribution of all compact binaries using the strongly-parameterized FullPop (left) and the weakly-parameterized (m_1, m_2)-PixelPop analyses (right). We direct the reader to Tab. 1 for details of the models. The upper triangles in Fig. 1 plot the fractional uncertainty of the merger rate density (in red). Both FullPop and PixelPop use the default spin magnitude, tilt and redshift models (Tab. 1). The two-dimensional distribution, $p(m_1, m_2)$ (in blue), displays three notable overdensities: first, an overdensity corresponding to BNS systems $(m_1, m_2) \approx (1, 1)\,\mathrm{M}_\odot$; second, a prominent overdensity centered at $(m_1, m_2) \approx (10, 10)\,\mathrm{M}_\odot$; and, last, a weaker overdensity at $(m_1, m_2) \approx (35, 30)\,\mathrm{M}_\odot$. Sections 5 and 6 provide a detailed investigation of systems into the last two features.

With GWTC-5.0, our models rule out a completely empty gap between 3–5 $\mathrm{M}_\odot$. Historically, Galactic observations suggested a dearth of compact objects in the ∼3–5 $\mathrm{M}_\odot$ range, potentially caused by the physics of supernova explosions (e.g., Bailyn et al. 1998; Farr et al. 2011; Kreidberg et al. 2012). Recently, this picture has been challenged, both by electromagnetic (van den Heuvel & Tauris 2020; Wang et al. 2024; Barr et al. 2024) and GW observations (Abbott et al. 2020b; Abac et al. 2024) of individual sources. Our previous study based on GWTC-4.0 (Abac et al. 2025a) also found that a completely empty gap is disfavored and this is reinforced by our analyses with GWTC-5.0. While the mass distribution inferred by FullPop is consistent with a dip in the merger rate between the NS peak and the ∼10 $\mathrm{M}_\odot$ BH peak, it rules out a completely empty gap. In this model, a parameter, A, controls the gap depth; with $A = 1$ indicating a completely empty gap between 3–5 $\mathrm{M}_\odot$. We instead find $A \leq 0.88$ at 99% credibility. PixelPop also finds a qualitatively flat mass distribution between the two peaks with no evidence for a pronounced dip. Figure 13 in App. B.2 shows the inferred primary mass distribution at the lower end of the mass range.

4.2. *Merger Rates*

The full mass spectrum models described above model the joint $m_1 - m_2$ distribution and allow us to self-consistently estimate the rates of stellar-mass BBH, BNS, NSBH, and intermediate-mass BH (IMBH) mergers. Following Abac et al. (2025a), we assume that the threshold between a NS and a black hole is 2.5 $\mathrm{M}_\odot$, consistent with both astrophysical observations and nuclear physics (Landry et al. 2020; Dietrich et al. 2020; Legred et al. 2021; Huth et al. 2022; Ai et al. 2023; Dittmann et al. 2024; Rutherford et al. 2024; Koehn et al. 2025; Margalit & Metzger 2017; Rezzolla et al. 2018; Ruiz et al. 2018; Abbott et al. 2020a; Nathanail et al. 2021; Cotturone et al. 2026; Mali & Essick 2026).

Table 2 shows the estimated rates for the different category of mergers using PixelPop and FullPop. In order to obtain a conservative merger-rate estimate that is less sensitive to modeling assumptions, we also calculate a joint merger rate interval estimated as the union of the 90% credible intervals of FullPop and PixelPop. Since GWTC-5.0 includes no new CBCs with significant support below a component mass of 2.5 $\mathrm{M}_\odot$, the upper bounds of the rates for NSBH and BNS mergers are lower than in GWTC-4.0.

We also define an IMBH source category comprising binaries with both $m_1, m_2 \in [100, 200]\,\mathrm{M}_\odot$. The most massive BBH in GWTC-5.0, GW231123_135430 (henceforth GW231123), has negligible support for source-frame masses above 200 $\mathrm{M}_\odot$ (Abac et al. 2025d) under standard parameter estimation priors; any rate estimate above this mass will therefore be driven either by priors or by model extrapolations from lower masses. While the detector network still has small but non-negligible sensitivity up to source-frame masses of 500 $\mathrm{M}_\odot$ (Abac et al. 2026c; Abbott et al. 2022), we find that our upper limits on merger rates in this regime are both highly dependent on modeling assumptions and as-

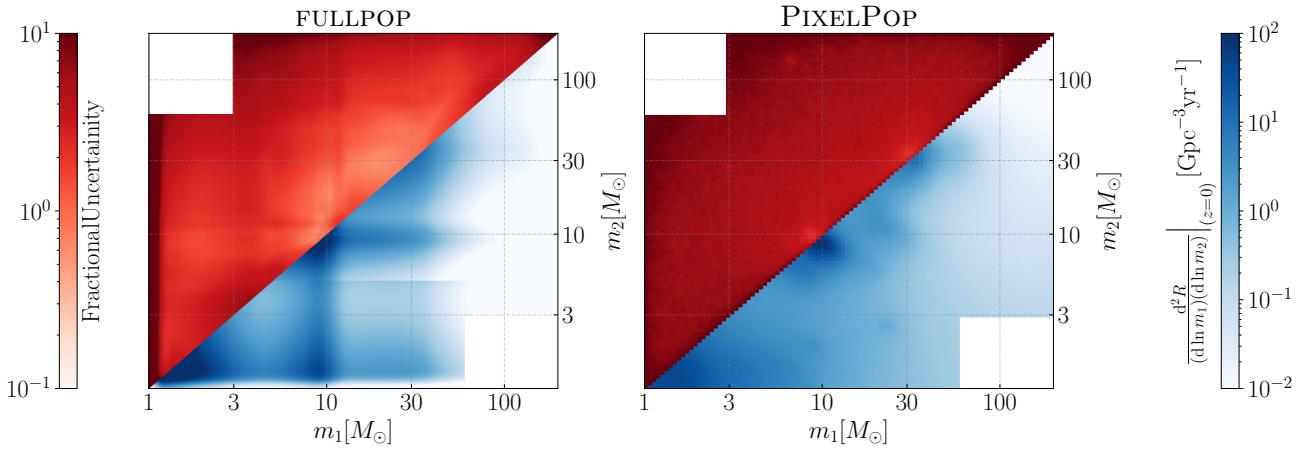

Figure 1. The differential merger rate distribution as a function of component masses for the full compact binary population inferred using FULLPOP (left) and (m_1, m_2)-PIXELPOP (right) models. The lower triangle in each subplot shows the median mass distribution while the upper triangle shows the corresponding fractional uncertainty, $\Delta R/R$, defined as the difference between the 95th and 5th percentile values divided by the median. Since $m_1 \geq m_2$ by definition, the axes are flipped for the upper uncertainty triangles (i.e., vertical axis is m_1 for the upper triangles). The overdense vertical stripe at $m_1 \sim 10\,\mathrm{M}_\odot$ in the FULLPOP plot arise because the common pairing function shared by BNS and NSBH mergers in the model is not well constrained, resulting in a median mass-ratio distribution that is approximately flat. The FULLPOP model uses different pairing functions for binaries with m_2 above and below $5\,\mathrm{M}_\odot$ explaining the apparently discontinuity there. The regions with $m_1 > 60\,\mathrm{M}_\odot, m_2 < 3\,\mathrm{M}_\odot$ have been cut out because of lack of simulated signals (cf. App. A.2) in that region in GWTC-3.0 which prevents a self-consistent accounting of selection effects at those masses.

Type	BNS*	NSBH*	BBH†	IMBH†
m_1 range	$m_1 \in [1, 2.5]\,\mathrm{M}_\odot$	$m_1 \in [2.5, 200]\,\mathrm{M}_\odot$	$m_1 \in [2.5, 200]\,\mathrm{M}_\odot$	$m_1 \in [100, 200)\,\mathrm{M}_\odot$
m_2 range	$m_2 \in [1, 2.5]\,\mathrm{M}_\odot$	$m_2 \in [1, 2.5]\,\mathrm{M}_\odot$	$m_2 \in [2.5, 200]\,\mathrm{M}_\odot$	$m_2 \in [100, 200)\,\mathrm{M}_\odot$
PIXELPOP	$23.4^{+54.7}_{-18.2}$	$15.9^{+16.9}_{-8.9}$	$37.5^{+11.9}_{-9.1}$	$3.8^{+16.1}_{-3.3} \times 10^{-3}$
FULLPOP	$59.3^{+95.4}_{-43.9}$	$14.2^{+12.0}_{-7.5}$	$36.0^{+11.1}_{-8.5}$	$6.4^{+16.7}_{-5.3} \times 10^{-3}$
Joint	5.1–154.7	6.7–32.8	27.5–49.4	$(0.6\text{–}19.9) \times 10^{-3}$

Table 2. Merger rates in units of $\mathrm{Gpc}^{-3}\,\mathrm{yr}^{-1}$ of the different categories of CBCs based on the FULLPOP and PIXELPOP. The bottom row shows the joint merger rate, calculated as the union of two 90% credible intervals. The columns marked with $*$ report the merger rates at $z = 0$, while those marked by a † report them at $z = 0.2$ as that is approximately the redshift at which we measure the BBH rates the best.

trophysically uninteresting when contrasted with theoretical models (e.g., Fragione et al. 2022).

4.3. *BNS and NSBH Properties*

We do not present analyses of BNS and NSBH systems and refer the readers to see Secs. 4.3 and 5 of Abac et al. (2025a), and Sec. 5 of Abac et al. (2024) for our latest analyses of NS population properties inferred using GW detections. Recent claims of eccentricity in the NSBH merger, GW200105_162426 (Fei & Yang 2024; Morras et al. 2025; Jan et al. 2026; Planas et al. 2025; Tiwari et al. 2025), if confirmed, might warrant revisiting the NS mass models used in previous studies (Landry & Read 2021; Biscoveanu et al. 2022b).

4.4. *BBH Properties*

We next focus on BBH mergers. Following GWTC-3.0 and GWTC-4.0 (Abbott et al. 2023b; Abac et al. 2025a), we only include events with FAR $\leq 1\,\mathrm{yr}^{-1}$ and for which both $m_1, m_2 \geq 3\,\mathrm{M}_\odot$ at 99% credibility with default parameter estimation priors (Abac et al. 2026c,b). This yields a cumulative catalog of 259 BBH candidates. The BBH mass-threshold here is more conservative than what is used in the full-spectrum analyses in Sec. 4.1 and Sec. 4.2. This is because the goal there is to model the whole CBC population and self-consistently estimate the rates of each category. The mass threshold here, instead aims to ensure that sources containing NSs do not contaminate our inference of BBH properties under population priors. Nevertheless, because our formalism for selection effects (see Sec. 3) does not account for this additional selection criteria, features of the BBH-only analyses below $\sim 8\,\mathrm{M}_\odot$ should be interpreted with caution. Following our previous papers (Abac et al. 2025a; Abbott et al. 2023b) we quote all BBH differential merger rates at $z = 0.2$.

4.4.1. *Primary Mass Distribution*

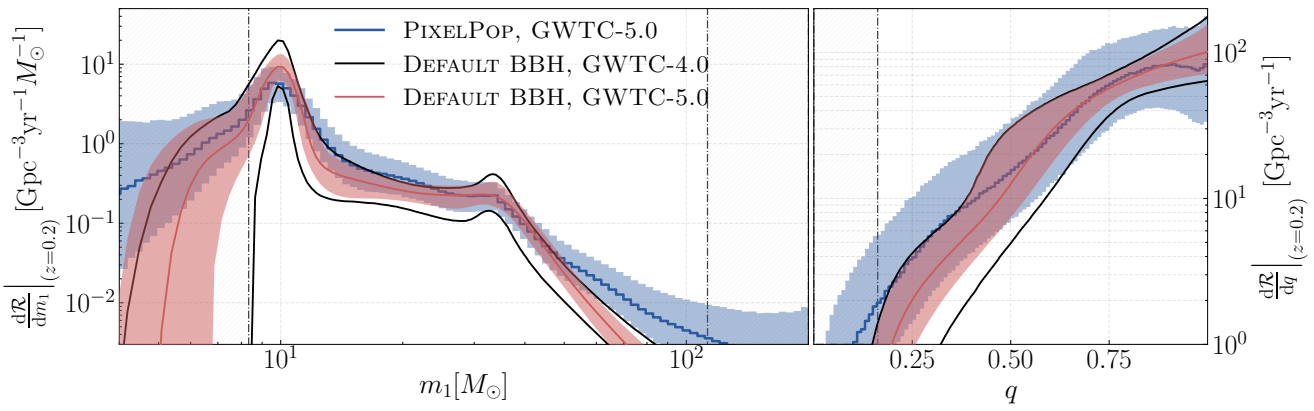

Figure 2. The distribution of the primary mass of the BBH population (left), and the mass ratio distribution (right). The solid lines show the median merger-rate density for each model, with the shaded bands depicting the 90% credible regions. The solid black lines show the 90% credible bounds for the strongly-parameterized model from GWTC-4.0. The hatched grey areas behind the dot-dashed lines—in this and all subsequent figures—correspond to regions at the edges of the parameter space with < 1% of BBH parameter estimation samples equally weighted across all detections. This is intended as a heuristic proxy for parts of parameter space where the models may not be actively constrained by the data, and where modeling and prior choices may become particularly important. See Sec. 3 for more details.

The left subplot of Fig. 2 shows the BBH merger rate distribution as a function of the primary mass. We use Default BBH as our strongly-parameterized model and a (m_1, m_2)-PixelPop, with the BBH selections described above, as our weakly-parameterized model. We find qualitatively good agreement between the weakly- and strongly-parameterized models for the primary-mass distribution.

We robustly find a global peak at $m_1 \sim 10\,M_\odot$ and a feature in the mass spectrum at $m_1 \sim 35\,M_\odot$, consistent with Abac et al. (2025a). We find that $72^{+7}_{-9}\%$ ($60^{+8}_{-10}\%$) of BBH mergers have $m_1 \in (8, 15)\,M_\odot$ with the Default BBH (PixelPop) model. Both models observe a clear drop in density on both sides of the peak. With the Default BBH model, we find a break in the power law at $m_{\rm break} = 37.5^{+10.9}_{-7.8}\,M_\odot$, where the slope changes from $\alpha_1 = 1.5^{+1.0}_{-1.4}$ to $\alpha_2 = 5.4^{+1.4}_{-1.6}$. This implies $\alpha_2 > \alpha_1$ at 99.6% credibility, consistently with (Abac et al. 2025a). However, it is possible that such steepening is dependent on our assumptions about the maximum mass (Mould et al. 2026).

Earlier analyses reported hints of additional peaks at $m_1 \sim 20\,M_\odot$ and $60\,M_\odot$ when using weakly-parameterized models (e.g. Tiwari & Fairhurst 2021; Edelman et al. 2023; Tiwari 2024; Magaña Hernandez & Palmese 2024; Abac et al. 2025a; Gennari et al. 2025; Pierra & Papadopoulos 2026). We do not find evidence for either of them in GWTC-5.0 based on the PixelPop primary-mass distribution. Recent works suggest the presence of a subpopulation of mergers with rapidly-spinning BHs, peaking around $16\,M_\odot$ (Plunkett et al. 2026; Farah et al. 2026; Tong et al. 2025a; also see Sec. 8). More targeted joint models of spins and masses might be able to tease out such substructure.

4.4.2. *Mass Ratio Distribution*

We find that the global BBH mass-ratio distribution is consistent with a peak at $q = 1$. The right subplot of Fig. 2 shows the mass-ratio distribution of the BBH population, taking a (m_1, q)-PixelPop analysis as our weakly-parameterized model. This is in-line with the results from GWTC-4.0: although the B-Spline model highlighted in Abac et al. (2025a) (App. C) finds evidence for a peak in the global distribution at $q \approx 0.8$, other flexible models explored there find that the distribution is consistent with a peak at $q = 1$ suggesting some degree of model dependence. When the mass-ratio distribution is fit with a power law, $p(q) \propto q^{\beta_q}$, we find $\beta_q = 1.0^{+0.8}_{-0.7}$. This is a somewhat flatter distribution than the value of $\beta_q = 1.2^{+1.2}_{-1.0}$ from GWTC-4.0, but still statistically consistent with it.

4.4.3. *Spin Distribution*

We first consider the individual spin magnitudes (χ_1, χ_2) and tilts $(\cos\theta_1, \cos\theta_2)$.[1] Figure 3 shows their distributions inferred using the Default BBH model, and the $(\chi, \cos\theta)$-PixelPop model. The former models both χ_1 and χ_2 as independently and identically distributed Gaussians truncated over the range of $[0, 1]$. The spin tilts, $\cos\theta_1$ and $\cos\theta_2$, are assumed to be non-independently distributed as a mixture model consisting of an isotropic and a non-isotropic component (see App. B.4). The $(\chi, \cos\theta)$-PixelPop model treats both component spins and spin tilts as independent and identically distributed draws from the same underlying distribution.

Both models infer BBH spin distributions that are consistent with our GWTC-4.0 inference in Abac et al. (2025a). The spin tilt distribution is broad, with the possibility of a

[1] Following Abac et al. (2025a), we define tilts at a fixed reference frequency, which is typically 20 Hz but differs for some events. Yet, tilts remain constant over the inspiral to leading order (Apostolatos et al. 1994) and we have checked that the reference point does not impact our conclusions.

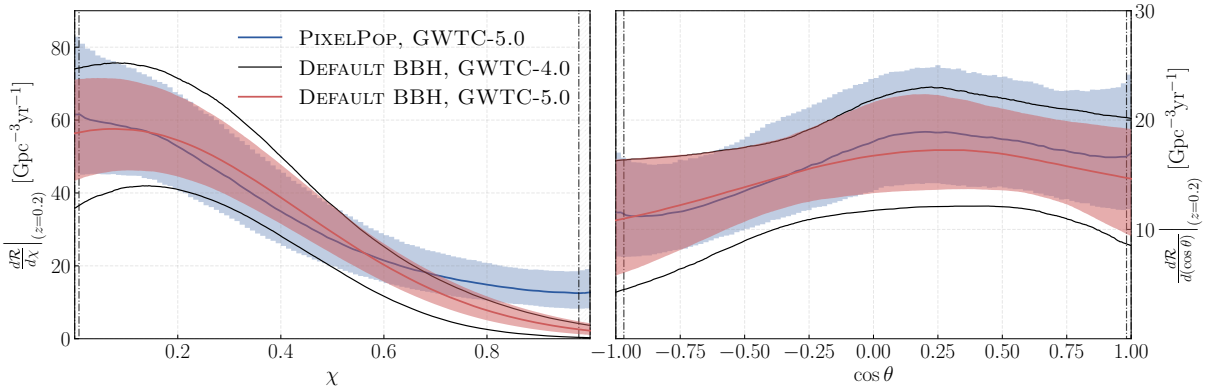

Figure 3. Differential BBH merger rate as a function of component spin-magnitudes (left) and tilts (right), assuming that the magnitudes and tilts of both components come from the same underlying distribution. The solid lines show the median merger-rate density for each model, with the shaded bands depicting the 90% credible regions. The solid black lines show the 90% credible bounds for the strongly-parameterized model from GWTC-4.0

peak in $\cos\theta$ between $[0, 0.5]$ or a broader plateau (right panel, Fig. 3). We find that $54^{+6}_{-4}\%$ ($57^{+5}_{-5}\%$) of BHs are aligned at some degree – i.e., $\cos\theta > 0$ with – the orbital angular momentum when using Default BBH (PixelPop). The spin-magnitude distribution, on the other hand, peaks at small values but with a tail extending beyond $\chi \sim 0.8$ (left panel, Fig. 3). Using the Default BBH (PixelPop) model, we infer that $80^{+4}_{-5}\%$ ($73^{+4}_{-4}\%$) of BHs have $\chi \leq 0.5$.

When modeling the component spin-magnitudes separately and allowing for correlations between them using TGMM analysis (App. B.3; Hussain et al. 2026; Hussain et al. 2025), we infer that the fraction of BBH mergers with small spins $\chi_{1,2} \lesssim 0.25$ is $0.85^{+0.06}_{-0.09}$, with the rest belonging to a subpopulation with at least one rapidly-spinning BH $\chi \sim 0.7$ (App. B.3, Fig. 14). **We now confidently find this high-spin subpopulation with GWTC-5.0** confirming similar indications from previous analyses using GWTC-3.0 and GWTC-4.0 (Hussain et al. 2026; Adamcewicz et al. 2025; Guttman et al. 2026; Banagiri et al. 2025b; Wolfe et al. 2026), and consistent with our further findings on BHs with rapid spins in Sec. 8. The TGMM analysis, in particular, also raises the possibility that the secondary BH in this subpopulation might also have rapid spins which, if confirmed, has implications for their formation mechanism (see App. B.3).

We obtain a complementary view of the spins by considering the effective inspiral and precessing spin parameters, $\chi_{\rm eff}$ (Racine 2008; Ajith et al. 2011) and $\chi_{\rm p}$ (Schmidt et al. 2011, 2012, 2015; Gerosa et al. 2021), respectively. These are compressed descriptions of the spin degrees of freedom that respectively encode mass-weighted projections of the component spins along and perpendicular to the orbital angular momentum. Figure 4 shows their distributions using the Bivariate Skewed $\chi_{\rm eff}/\chi_{\rm p}$ and the $(\chi_{\rm eff}, \chi_{\rm p})$-PixelPop models. The two analyses disagree about the skewness of the distribution (App. B.6): while Bivariate Skewed $\chi_{\rm eff}/\chi_{\rm p}$ finds a right-skewed $\chi_{\rm eff}$ distribution (Fig. 19), PixelPop infers a $\chi_{\rm eff}$ distribution with significantly lower skewness. A certain degree of model dependence of the skewness was already highlighted in GWTC-4.0 (see Fig. 21 of Abac et al. 2025a).

However, both models agree that BBH mergers are more likely to have positive (albeit small) rather than negative $\chi_{\rm eff}$ values, which could provide robust limits on preferentially-aligned channels such as isolated binaries evolution or AGN disks (Gerosa et al. 2018; Rodriguez et al. 2016; Banagiri et al. 2025a). We quantify this with the degree of asymmetry about zero, $\delta\chi = p(\chi_{\rm eff} > 0) - p(\chi_{\rm eff} < 0)$, finding that $\delta\chi = 0.22^{+0.13}_{-0.13}$ ($0.28^{+0.11}_{-0.12}$) with Bivariate Skewed $\chi_{\rm eff}/\chi_{\rm p}$ (PixelPop) model (Fig. 4 inset). Calculating the union of the 90% credible intervals on $\delta\chi$ inferred by Bivariate Skewed $\chi_{\rm eff}/\chi_{\rm p}$ and PixelPop, **we estimate that at least 9–40% of mergers must originate from preferentially aligned channels to explain the observed asymmetry.**

Moreover, consistent with previous catalogs (Abbott et al. 2021b, 2023b; Abac et al. 2025a), **we find that** $39^{+7}_{-7}\%$ ($36^{+6}_{-6}\%$) **of binaries have negative** $\chi_{\rm eff}$ **according to the Bivariate Skewed** $\chi_{\rm eff}/\chi_{\rm p}$ **(PixelPop) model; indicating systems with at least one BH spin misaligned at more than** 90° **with the orbital angular momentum**. If one assumes that all such binaries come from dynamical formation channels such as dense stellar clusters this suggests that a majority of BBH mergers originate from such channels. However, it may be possible for anti-aligned binaries to develop if the stellar progenitors of BHs experience large supernova kicks (Baibhav & Kalogera 2024). Alternatively, Kıroğlu et al. (2025) posits that the entire $\chi_{\rm eff}$ distribution might be explained by mergers in dynamical environments where a preference for mild alignment might arise from stellar collisions with compact object binaries.

Finally, we find that the $\chi_{\rm p}$ distribution peaks at a small but non-zero value of χ_p indicating that a non-negligible fraction of the BBH population have in-plane spins and experience precession.

4.4.4. *Redshift Distribution*

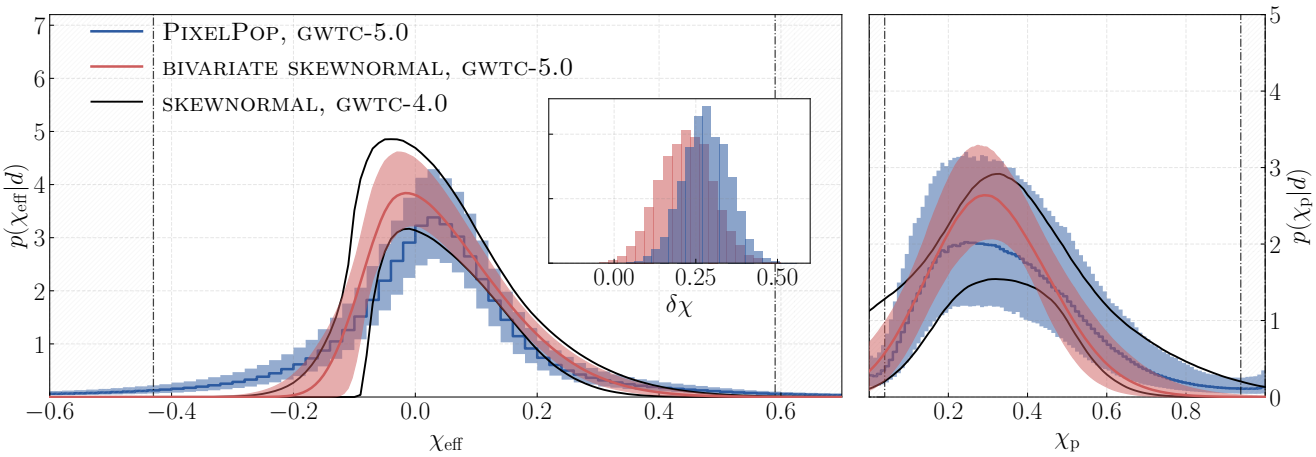

Figure 4. Posterior distribution of effective spins in the BBH population: $\chi_{\rm eff}$ (left) and $\chi_{\rm p}$ (right). The inset shows that the asymmetry about zero, $\delta\chi = p(\chi_{\rm eff} > 0) - p(\chi_{\rm eff} < 0)$ is found to be positive, indicating a preference for aligned binaries

To infer the redshift distribution, we use z-PixelPop as our weakly-parameterized redshift model, and the Default BBH model as our strongly-parameterized one. We assume a ΛCDM cosmology based on inferred cosmological parameter values from Planck15 (Ade et al. 2016). Figure 5 shows the comoving source-frame redshift distribution inferred by the two analyses, along with the GWTC-4.0 bounds for comparison. We estimate the BBH merger rate at $z = 0.2$ to be $30.4^{+6.5}_{-5.4}\,(32.8^{+10.7}_{-7.6})\,\mathrm{Gpc^{-3}\,yr^{-1}}$ using the Default BBH (PixelPop) model for the redshift distribution.[2]. These rates are consistent with the corresponding BBH rates inferred in Abac et al. (2025a) and represents a 20% reduction in statistical uncertainty over GWTC-4.0 when comparing the Default BBH models..

With the updated GWTC-5.0 catalog, we find $\kappa_z = 2.5^{+0.7}_{-0.7}$ for the Default BBH redshift power-law index, which is slightly flatter but statistically consistent with the estimate using GWTC-4.0 (Abac et al. 2025a), as well as being consistent with the redshift evolution of star-formation rate (SFR) (Madau & Dickinson 2014); see Fig. 5. We do not find strong evidence for additional structure in the redshift distribution beyond a power law; a parametric model based on the Madau–Dickinson SFR model has a log Bayes factor of $\log_{10}\mathcal{B} = -0.15$ compared to Default BBH. See App. B.5 for more details.

It is unclear if the structures in the z-PixelPop inference at $z \leq 0.5$ represent real features or statistical fluctuations. Such features have been noted with past data by non-Bayesian analyses that infer the maximum-likelihood population model (Payne & Thrane 2023; Guttman et al. 2026) and with some weakly-parameterized models (Edelman et al. 2023). With present data, these structures are not confidently required in the PixelPop analysis, and the inference of the model remains statistically consistent with a simple power law.

[2] The rates quoted here and in Tab. 2 rest on slightly different assumptions as the lower-limit on black hole mass is different which can lead to a different subset of events contributing to the analysis. Second, all of the binaries in that section are fit with a common redshift distribution, while here we focus only on those that are clearly BBH mergers.

5. PROPERTIES OF THE ∼10 $\mathrm{M_\odot}$ PEAK

The global maximum of the BBH primary-mass distribution at ∼10 $\mathrm{M_\odot}$ has been extensively studied since it was first identified in GWTC-2.0 (Tiwari & Fairhurst 2021; Edelman et al. 2022; Abbott et al. 2023b; Abac et al. 2026d). The existence of this peak and some of its properties are consistent with expectations from isolated binary evolution (Dominik et al. 2015; Belczynski et al. 2020; Giacobbo & Mapelli 2018; Wiktorowicz et al. 2019; Neijssel et al. 2019), including the stable mass transfer channel (e.g., van Son et al. 2022b,a). Those models typically predict that BHs in the ∼10 $\mathrm{M_\odot}$ peak should have low spins preferentially aligned with the orbital angular momentum. Additionally, in the stable mass transfer channel, the combination of mass-ratio reversal, envelope stripping, and the mass-transfer stability cut can cause the mass-ratio distribution to peak away from unity, around $q \sim 0.6$–0.8 (e.g., Neijssel et al. 2019; Olejak & Belczynski 2021; van Son et al. 2022c; Olejak et al. 2021; Broekgaarden et al. 2022; Dorozsmai & Toonen 2024).

In GWTC-5.0, the peak around 10 $\mathrm{M_\odot}$ is discernible in both the primary and secondary masses, whether the data are analyzed with strongly- or weakly-parameterized models (see Fig. 1 and Fig. 2). The overdensity appearing in both components is consistent with the fact that very uneven mass pairings are disfavored by the data (see also Fig. 9). Nevertheless, Godfrey et al. (2023) found signs in GWTC-3.0 that systems with primaries $m_1 \sim 10\,\mathrm{M_\odot}$ are more likely to have a lighter companion, an observation that persisted in GWTC-4.0 (Abac et al. 2026d), where we found a preference for mass ratio $q \sim 0.8$ for systems with primaries $m_1 \sim 10\,\mathrm{M_\odot}$.

With GWTC-5.0, we are not able to confidently confirm a preference for asymmetric masses for systems in

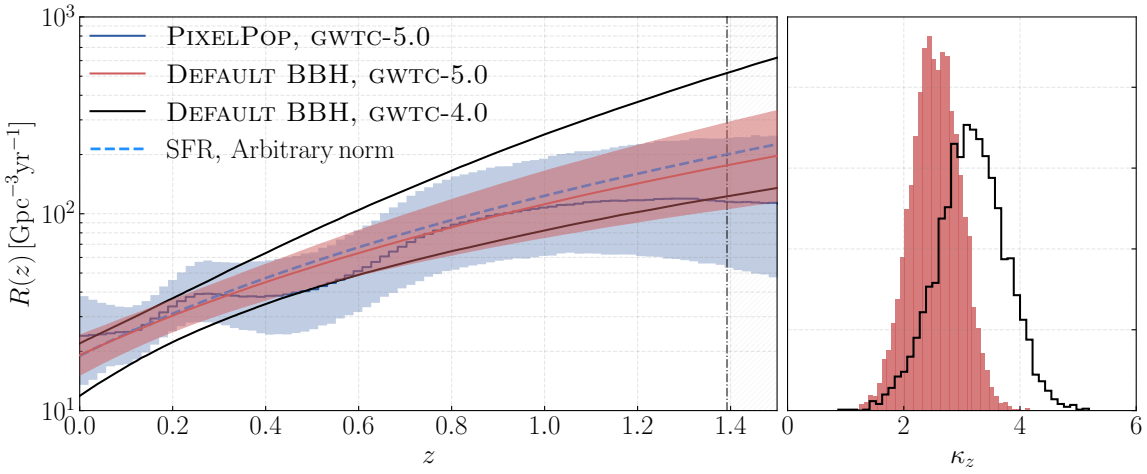

Figure 5. The BBH redshift distribution (left), and the inferred value of the redshift spectral index κ_z assuming $p(z) \propto (1+z)^{\kappa_z}$ (right). The dashed blue lines in the left panel show the redshift evolution of the SFR (arbitrary normalisation)

the $\sim 10\,M_\odot$ peak. While the new dataset could allow for an overabundance of $q \approx 0.8$ systems in the peak, such a feature is not strictly required by the data. The degree of support for the $q \sim 0.8$ peak at $\sim 10\,M_\odot$ depends on modeling choices, as evidenced by our comparison to the dedicated Isolated Peak mode (Godfrey et al. 2023) to the more flexible PixelPop and Binned Gaussian Process models (Fig. 6). The Isolated Peak analysis models the $\sim 10\,M_\odot$ peak and the underlying continuum with distinct mass-ratio and spin distributions. We compare its inferences for the peak (continuum) to those of the weakly-parametrized models within (outside) the $[8, 15]\,M_\odot$ primary-mass range.

The Isolated Peak model finds some preference for mergers in the $\sim 10\,M_\odot$ peak having unequal masses, measuring $q = 0.80^{+0.17}_{-0.31}$ based on posterior-predictive from the Gaussian peak component (red distribution in the top-left panel of Fig. 6). However, unlike in GWTC-4.0, this preference does not markedly distinguish the peak from the rest of the population: posterior-predictive draws from the continuum component give $q = 0.73^{+0.24}_{-0.51}$ (blue distribution in the top-left panel of Fig. 6), a broader range than for the peak but with a similar degree of support for $q = 0.8$ versus $q = 1$. Even though systems in the peak favor $q = 0.8$ on average, the posterior-predictive bands in the top-left panel of Fig. 6 show that both the peak and the continuum can accommodate similar merger-rate densities for $q = 1$ as $q = 0.8$ within 90% credibility. In fact, the merger-rate density at $q = 0.8$ is found to be $1.6^{+6.6}_{-1.1}$ times the value at $q = 1$ for the peak and $1.5^{+3.7}_{-1.0}$ for the continuum, which are both consistent with unity. In other words, based on the upper and lower bounds of these 90%-credible ranges, Isolated Peak does not find that the $\sim 10\,M_\odot$ peak significantly favors $q = 0.8$ over $q = 1$, although that cannot be ruled out either: the $q = 0.8$ versus $q = 1$ merger-rate density ratio could be as high as $\sim 8:1$ and as low as $\sim 1:2$.

The potential preference for $q = 0.8$ in the $\sim 10\,M_\odot$ peak becomes even more ambiguous when we consider other models. As seen in the top-middle panel of Fig. 6, PixelPop does not find a marked preference for unequal masses for binaries in this peak (red). On the contrary, the (m_1, q)-PixelPop analysis suggests that systems in the $[8, 15]\,M_\odot$ range are more likely on average to have equal rather than unequal masses. This is also evident in the right panel of Fig. 1 from the (m_1, m_2)-PixelPop run, where the excess at $\sim 10\,M_\odot$ is consistent with the diagonal line $m_1 = m_2$. PixelPop finds the merger-rate density at $q = 0.8$ to be $1.1^{+5.6}_{-0.9}$ times the rate at $q = 1$ for the peak and $0.7^{+1.4}_{-0.5}$ for the continuum. This means that, while PixelPop allows the $\sim 10\,M_\odot$ peak to favor $q = 0.8$ over $q = 1$ by as much as $\sim 7:1$, the ratio could be as low as $\sim 1:5$, so a preference for uneven masses in the peak is not required.

The other flexible model, Binned Gaussian Process, finds a similar result (top-right panel of Fig. 6). The merger-rate density at $q = 0.8$ is found to be $1.3^{+2.7}_{-0.6}$ times the value at $q = 1$ for the peak (red) and $1.0^{+0.6}_{-0.3}$ for the continuum (blue). At 90% credibility, thus, the preference for $q = 0.8$ over $q = 1$ could be as high as $\sim 4:1$ and as low as $\sim 1:1.4$ for systems in the peak. Unlike PixelPop, Binned Gaussian Process applies a flexible model in the three-dimensional space of $(m_1, q, \chi_{\rm eff})$ but fixes the distribution in redshift and other spin degrees of freedom.

All in all, there is inconclusive evidence for distinctly unequal masses in the $\sim 10\,M_\odot$ peak: all three models considered here allow for such an asymmetry to exist preferentially in the peak more so than in the rest of the population, but none of the models strictly require it. In this respect, the data remain consistent with the $\sim 10\,M_\odot$ peak originating in a specific formation channel that yields uneven masses, such as stable mass transfer, but the mass-ratio distribution alone is not currently sufficient to confidently ascertain this. Nevertheless, all models favor $q > 0.5$ for the peak.

If systems in the $\sim 10\,M_\odot$ peak do originate in a specific formation channel, they may also have distinct spin properties. The Isolated Peak model, which explicitly assigns an inde-

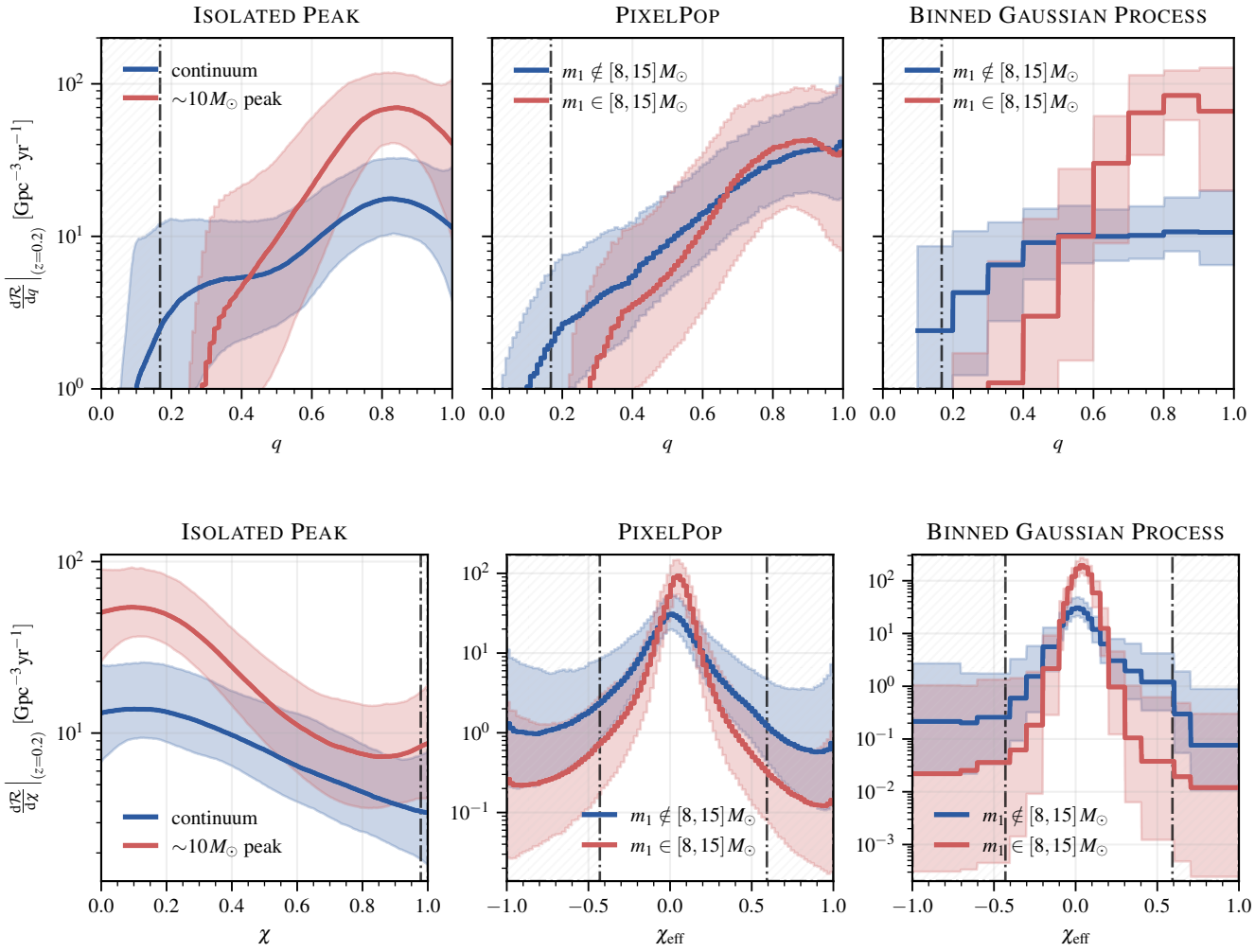

Figure 6. Mass-ratio (top row) and spin (bottom row) distributions for the $\sim 10\,M_\odot$ peak (red) versus the rest of the population (blue), inferred with Isolated Peak (left), PixelPop (middle), and Binned Gaussian Process (right). PixelPop results come from a (m_1, q) run in the top row, and an $(m_1, \chi_{\rm eff})$ run in the bottom row. Isolated Peak natively models the spin magnitude χ (bottom left panel), while PixelPop and Binned Gaussian Process model the effective inspiral spin $\chi_{\rm eff}$ (bottom middle and right panels). All models favor $q > 0.5$ for the peak. The Binned Gaussian Process merger-rate-densities at $z = 0.2$ are calculated assuming a powerlaw index of 2.7 (see Tab. 1).

pendent spin-magnitude distribution to the peak, finds that **systems in the peak have a broad distribution of spin magnitudes that is consistent with the rest of the population, although with slightly more support for low magnitudes** (bottom-left panel of Fig. 6). Concretely, the 90%-credible upper limit on the spin magnitude is $\chi_{90\%} = 0.78^{+0.07}_{-0.07}$ for the continuum (blue) while only $\chi_{90\%} = 0.68^{+0.12}_{-0.12}$ within the peak (red). We performed an additional check in the $(m_1, \chi_{\rm eff})$-PixelPop run (bottom-middle panel in Fig. 6), which similarly finds that systems in the $[8, 15]\,M_\odot$ range are more tightly constrained to have low effective inspiral spins than the rest of the population; the median of the PPD implies $\chi_{\rm eff} = 0.01^{+0.43}_{-0.52}$ for systems outside that range but $\chi_{\rm eff} = 0.05^{+0.15}_{-0.19}$ within it. The $(m_1, q, \chi_{\rm eff})$ Binned Gaussian Process analysis (bottom-right panel of Fig. 6) shows a qualitatively comparable effective-inspiral-spin structure, with a broader $\chi_{\rm eff}$ distribution for systems in the $[8, 15]\,M_\odot$ range than for the rest of the population; the median PPD curves give $\chi_{\rm eff} = 0.02^{+0.34}_{-0.22}$ outside the $[8, 15]\,M_\odot$ range (blue) while $\chi_{\rm eff} = 0.04^{+0.10}_{-0.10}$ within it (red). Both PixelPop and Binned Gaussian Process find a slightly more pronounced preference for positive $\chi_{\rm eff}$ for the peak.

Finally, the $(m_1, \chi_{\rm eff})$-PixelPop run suggests that **systems in the $[8, 15]\,M_\odot$ range may display a correlation between effective inspiral spin and primary mass** that is not present in the rest of the population. The Spearman correlation coefficient (Spearman 1904) between $\log m_1$ and $\chi_{\rm eff}$ is found to be $\rho = 0.13^{+0.20}_{-0.20}$ for systems in that range while $\rho = -0.01^{+0.26}_{-0.23}$ for the rest of the population ($|\chi_{\rm eff}| \lesssim 0.25$ in both cases). While not yet statistically conclusive, this correlation could be hinting at signatures of binary processes such

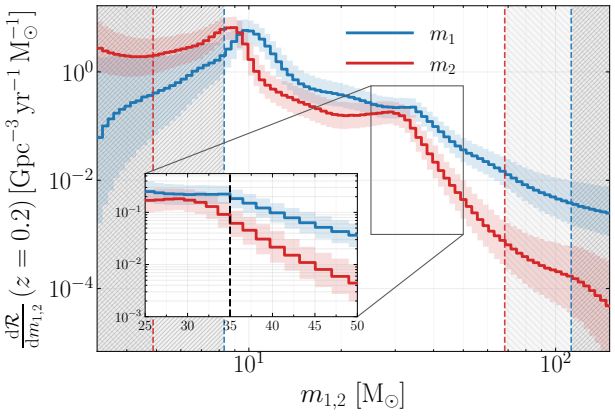

Figure 7. Marginal primary (m_1) and secondary (m_2) mass distributions reconstructed using (m_1, m_2)-PixelPop model. The inset shows the merger-rate density in the mass range 25–50 $\mathrm{M_\odot}$.

as accretion-induced spin-up of the first born BH (King & Kolb 1999).

6. PROPERTIES OF THE ~35 $\mathrm{M_\odot}$ FEATURE

In previous catalogs, we identified a potential local maxima in the BBH merger-rate density near $m_1 \sim 35\,\mathrm{M_\odot}$ (Abbott et al. 2021b, 2023b; Abac et al. 2025a). While earlier work (e.g., Abbott et al. 2023b) identified a peak there with high significance, the analysis with GWTC-4.0 painted a more complex picture of the shape of the mass distribution, finding that the feature can either be a peak or a turnover marking the onset of a decline in merger-rate density (Abac et al. 2025a; Corelli et al. 2026). Such an ambiguity has also been noted in analyses that use more complex models for the mass-ratio distribution of binaries (e.g., Farah et al. 2024; Banagiri et al. 2025b). Here, we revisit the properties of the BHs that make up the $m_1 \sim 35\,\mathrm{M_\odot}$ feature with GWTC-5.0 using the weakly-parameterized models, PixelPop and Binned Gaussian Process.

Figure 7 shows the marginal primary- and secondary-mass distributions inferred using the bivariate (m_1, m_2)-PixelPop analysis. For a comparison of the PixelPop and Binned Gaussian Process m_1–m_2 distributions, see Fig. 24. The corresponding two-dimensional (m_1, m_2) merger-rate density does not reveal additional structure beyond that seen in the one-dimensional m_1 and m_2 marginals, so we focus on the marginal distributions. In the mass range [25–40] $\mathrm{M_\odot}$, the reconstructed m_1 and m_2 distributions are largest at $m_1 = 29.0^{+5.3}_{-3.4}\,\mathrm{M_\odot}$ and $m_2 = 27.8^{+3.7}_{-2.2}\,\mathrm{M_\odot}$, respectively. To quantify the shape of the two distributions, we compare the merger-rate density at several points in that range. For the primary mass, the marginal merger-rate density at $m_1 = 30\,\mathrm{M_\odot}$ is a factor of $0.8^{+0.7}_{-0.4}$ times the merger-rate density at $m_1 = 25\,\mathrm{M_\odot}$, while it is $2.2^{+1.6}_{-1.0}$ times larger than the merger-rate density at $m_1 = 40\,\mathrm{M_\odot}$. For the secondary mass, the marginal merger-rate density at $m_2 = 30\,\mathrm{M_\odot}$ is a factor of $1.0^{+1.1}_{-0.5}$ times the merger-rate density at $m_2 = 25\,\mathrm{M_\odot}$, but $7.9^{+9.4}_{-4.4}$ times larger than the merger-rate density at $m_2 = 40\,\mathrm{M_\odot}$. In other words, for both the primary- and secondary-mass distributions, we find that the merger-rate density at $25\,\mathrm{M_\odot}$ is consistent with the value at $30\,\mathrm{M_\odot}$, whereas the value at $40\,\mathrm{M_\odot}$ is clearly lower than at $30\,\mathrm{M_\odot}$. This shows that, within current levels of observational uncertainty, **the feature in the mass spectrum marks a change in slope in both the primary- and secondary-mass distributions, with the secondary turning over much more rapidly than the primary**.

Using both PixelPop and Binned Gaussian Process, we now turn to other properties of the BBH mergers comprising the ~35 $\mathrm{M_\odot}$ feature. We start with their mass ratios in the top left of Fig. 8. We find that the marginal mass-ratio distribution in this mass range peaks at $q = 1$ in both reconstructions. Using (m_1, q)-PixelPop, we find that the merger-rate density at $q = 1$ is $1.9^{+4.8}_{-1.4}$ times larger than at $q = 0.7$. This means that, while PixelPop allows for a merger-rate density at $q = 1$ that is a factor of ≈ 4.7 higher than at $q = 0.7$, it could also be lower by a factor of ≈ 0.5; so a preference for equal masses, while favored, is not yet strongly required by the data. This level of preference for equal-mass mergers is consistent with findings from both GWTC-3.0 and GWTC-4.0 for the ~35 $\mathrm{M_\odot}$ population (Li et al. 2022, 2024; Kishore Roy et al. 2025a; Abac et al. 2025a; Banagiri et al. 2025b).

The redshift evolution of the merger rate (top right of Fig. 8) of the ~35 $\mathrm{M_\odot}$ population—inferred with both (m_1, z)-PixelPop and Binned Gaussian Process—is broadly consistent with SFR. We observe mild deviations beyond $z \sim 1.2$. However, the inference at such high redshifts can be particularly sensitive to modeling and prior choice as it lies in a data-poor part of parameter space. We find no evidence that the primary-mass distribution of this population evolves with redshift.

The (m_1, χ_{eff})-PixelPop analysis finds that the χ_{eff} distribution for the ~35 $\mathrm{M_\odot}$ population is similar to that of the full population, with both distributions symmetric around zero. This corresponds to roughly 50% of systems having negative, albeit small, effective inspiral spin. This result is consistent with some previous studies using GWTC-3.0 and GWTC-4.0 (Ray et al. 2025; Abac et al. 2025a). However, other studies report a preference for ~30 $\mathrm{M_\odot}$ BHs to have a χ_{eff} distribution peaking at positive values (Sadiq et al. 2025a; Kishore Roy et al. 2025b). As shown in Figs. 8 and 24, we find that although Binned Gaussian Process finds a smaller fraction of mergers at negative χ_{eff}, its results are statistically consistent with PixelPop within 90% credibility. We also find no evidence for a correlation between m_1 and χ_{eff} in the primary-mass range [25–40] $\mathrm{M_\odot}$.

The ~35 $\mathrm{M_\odot}$ feature was originally discussed in the context of pair-instability physics. This is because pulsational pair-instability supernovae (PPISNe) are expected to compress a broad range of carbon-oxygen core masses into a narrow range of remnant masses, thereby producing a pile up in the BH mass spectrum that could have potentially explained this feature (Belczynski et al. 2016; Woosley 2017a; Spera & Mapelli 2017; Talbot & Thrane 2018; Stevenson et al. 2019; Marchant et al. 2019a; Karathanasis et al. 2023; Winch et al.

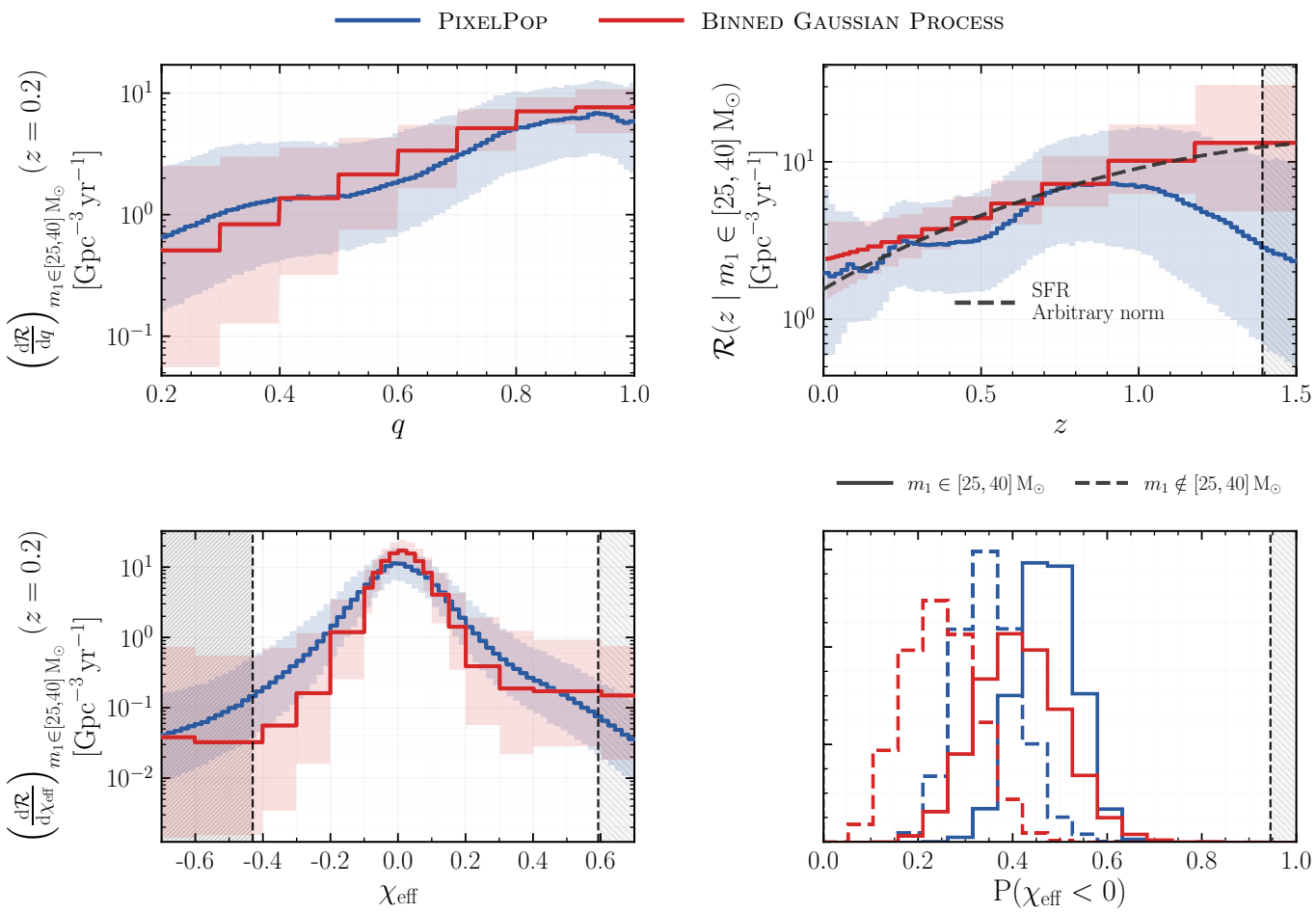

Figure 8. BBH merger rate for $m_1 \in [25, 40]\,M_\odot$, inferred using different variants of the PixelPop model: (m_1, q) (top left), (m_1, z) (top right), and (m_1, χ_{eff}) (bottom left panel). The bottom right panel shows the inferred fraction of mergers with negative χ_{eff}. These are overplotted with different variants of the Binned Gaussian Process model as a consistency check: (m_1, q, χ_{eff}) (top left), (m_1, m_2, z) (top right), and (m_1, m_2, χ_{eff}) (bottom panels). The agreement between PixelPop and the Binned Gaussian Process demonstrates the robustness of our results in this mass range. In this mass range, the mass-ratio distribution likely peaks at $q = 1$, indicating a preference for equal-mass mergers in the $\sim 35\,M_\odot$ population. The redshift distribution is broadly consistent with the star-formation rate and remains robust up to $z \sim 1.2$, beyond which modeling uncertainties dominate. The effective inspiral spin distribution for the $\sim 35\,M_\odot$ population is broadly consistent with that of the full population, with both exhibiting significant support at negative χ_{eff}. But the $\sim 35\,M_\odot$ population has a stronger preference for a symmetric χ_{eff} distribution about zero, as seen by the histograms of the fraction of binaries with $\chi_{eff} < 0$ (bottom right).. The Binned Gaussian Process merger-rate-densities at $z = 0.2$ are calculates assuming a powerlaw index of 2.7 (see Tab. 1).

2025). However, subsequent studies have argued that producing a feature at such low masses through PPISNe requires pushing the $^{12}C(\alpha,\gamma)^{16}O$ reaction rate above its laboratory-measured value, together with additional assumptions about mixing, winds, envelope stripping, and rotation. Therefore, the observed break near $\sim 30\,M_\odot$ is unlikely to be a direct signature of PPISNe alone (Farag et al. 2022; Hendriks et al. 2023; Costa et al. 2021; Vink et al. 2021; Croon & Sakstein 2025; Golomb et al. 2024; Kishore Roy et al. 2025b; Antonini et al. 2025).

This motivates the question of what astrophysical channel could instead explain the feature and its properties. Several possibilities have been proposed: chemically homogeneous evolution can form massive, nearly equal-mass binaries (de Mink & Mandel 2016; Mandel & de Mink 2016; Marchant et al. 2016); stable mass transfer with quasi-homogeneous evolution can generate structure near the same mass scale (Briel et al. 2023), as is also the case for Population III binaries (Kinugawa et al. 2014, 2021), dynamical formation in dense stellar environments, and hierarchical mergers (Rodriguez et al. 2018; Antonini et al. 2023; Ray et al. 2025). However it remains unclear if any of these formation mechanisms can explain *all* of the properties of the BHs at these masses explored above (Kishore Roy et al. 2025b; Banagiri et al. 2025b). The precise astrophysical origin of the $\sim 35\,M_\odot$ feature therefore remains open.

7. HIGH-MASS FEATURES

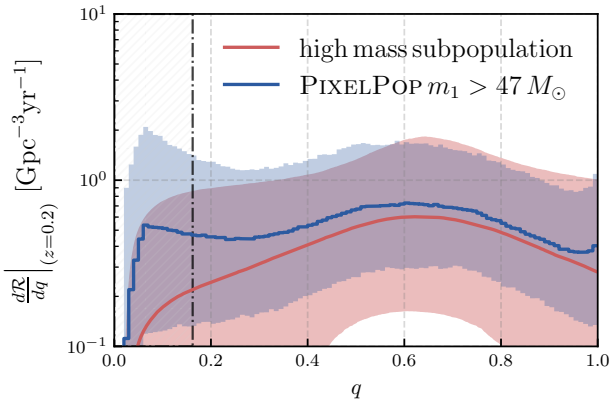

Figure 9. The mass-ratio distribution of the high-mass subpopulation with $m_1 \geq 46.6^{+11.6}_{-6.7}\,\mathrm{M}_\odot$ using the THREE-SUBPOPULATION model (in red, see App. I) and the mass-ratio distribution of the high-mass mergers with $m_1 > 47\,\mathrm{M}_\odot$ using (m_1, q)-PixelPop (blue). The spread in the inferred merger rate by PixelPop at $q < 0.2$ is driven by its agnostic priors.

We now investigate mergers at higher masses, $m \gtrsim 40\,\mathrm{M}_\odot$. In this region, the BBH mass spectrum drops rapidly, consistent with a power law (Sec. 4.4.1); previous studies have reported a potential rise of the mass distribution at $m_1 \sim$ 60–70 $\mathrm{M}_\odot$ (Magaña Hernandez & Palmese 2025; Abac et al. 2025a; Pierra & Papadopoulos 2026), but we do not find a significant overdensity around this mass scale in GWTC-5.0 using PixelPop (Fig. 1). Here we study mergers with $m_1 \gtrsim 40\,\mathrm{M}_\odot$ in search for signatures in the mass and mass-ratio distributions that differ from those at lower masses, potentially indicating that the high-mass BHs represent a distinct subpopulation.

As discussed in Sec. 6, the secondary-mass distribution exhibits a more pronounced decline at higher masses compared to the primary (Fig. 7). We quantify the difference using the slopes, i.e., logarithmic probability density versus logarithmic mass, of the marginal m_1 and m_2 distributions, averaged over two different mass intervals using (m_1, m_2)-PixelPop. In the range 40–60 $\mathrm{M}_\odot$, the slope of the m_2 distribution is constrained to be $-7.0^{+2.4}_{-2.7}$, significantly steeper at >99.9% credibility than in the lower-mass interval 13–25 $\mathrm{M}_\odot$ where the m_2 slope is $-1.1^{+1.1}_{-1.1}$. The m_1 distribution also exhibits a steeper decline at higher masses, consistent with a broken power-law structure with a steeper spectral index above $\sim$35 $\mathrm{M}_\odot$ (Sec. 4.4.1). However, the m_1 slope in the 40–60 $\mathrm{M}_\odot$ range is constrained to be $-3.8^{+1.3}_{-1.4}$ and is still shallower than the corresponding m_2 slope with 97.7% credibility.

Using a model that explicitly allows for a sharp gap, Tong et al. (2025b) reported one in the m_2 distribution beginning at $\sim$45 $\mathrm{M}_\odot$ with GWTC-4.0 data (see also Mould et al. 2026). However, other strongly-parameterized models that allow for a more flexible gap shape do not clearly find the sharp onset of a gap (Ray & Kalogera 2026). In GWTC-5.0, **while PixelPop does not resolve a sharp gap in m_2 (Fig. 1), we consistently find a clear suppression of systems with high m_2.** More conservatively, the cumulative distribution of m_2 also indicates only a small fraction of mergers above $\sim$40 $\mathrm{M}_\odot$ (Fig. 23 in App. H).

The relative scarcity of high-mass secondaries is consistent with the inferred pairing distribution (Fig. 9) of BBH mergers at high masses. We find that **binaries with $m_1 \gtrsim 40\,\mathrm{M}_\odot$ can exhibit low mass ratios**, consistent with the properties of a high-mass subpopulation reported in, e.g., Banagiri et al. (2025b); Ray et al. (2026). This tendency for unequal masses can also be qualitatively observed in several high-mass binaries discovered in O4b such as GW241127_061008, GW241102_144729, GW241230_084504, GW250109_074552 etc (Abac et al. 2026b). Using THREE SUBPOPULATION, which treats these high-mass mergers as a subpopulation with separate spin and mass-ratio properties (Banagiri et al. 2025b and App. I), we constrain the onset of this subpopulation to $m_1 = 46.6^{+11.6}_{-6.7}\,\mathrm{M}_\odot$. We find a similar transition in χ_{eff}, Sec. 8.1.

In this model, the mass-ratio distribution for this high-mass subpopulation is described by a Gaussian and we infer its mean to be at $q = 0.6^{+0.3}_{-0.5}$ (Fig. 9). Results for mergers with $m_1 > 47\,\mathrm{M}_\odot$ from (m_1, q)-PixelPop are overplotted for comparison; they similarly indicate that high-mass mergers preferentially follow a mass-ratio distribution peaked away from unity, supporting the tendency toward unequal-mass systems in this regime. Together with the mass-ratio distributions at lower m_1, this indicates that BBH pairing properties evolve with primary mass (cf. top row of Fig. 6 for mass ratios at $m_1 \sim 10\,\mathrm{M}_\odot$ and Fig. 8 for mass ratios at $m_1 \sim 35\,\mathrm{M}_\odot$). This could be a signature of underlying differences in the physics of BBH formation.

One of the predictions of stellar evolution theory is a gap in BH masses arising from very massive stars that undergo pair-instability supernovae (PISNe) and PPISNe (Fowler & Hoyle 1964; Barkat et al. 1967; Rakavy & Shaviv 1967; Heger et al. 2003; Woosley et al. 2007; Woosley 2017b; Spera & Mapelli 2017; Marchant et al. 2019b; Farmer et al. 2019). Although the precise locations of the lower and upper edges of this pair-instability mass gap depend sensitively on uncertain physical assumptions (Marchant et al. 2019b; Farmer et al. 2019; Costa et al. 2021; Renzo & Smith 2024), the presence of such a feature is a robust prediction of most stellar evolution models.

The primary-mass distribution in GWTC-5.0, however, shows no clear evidence for such a PISN gap: although it steepens at high mass, it extends smoothly beyond 100 $\mathrm{M}_\odot$. This suggests that, if there is a pair-instability gap, it should be polluted by some other formation pathways, e.g., hierarchical mergers from dense stellar clusters. The physics of several of these alternative formation channels, which are generally expected to be rare to begin with, can make it less likely that they contribute simultaneously to both components of a binary. Binaries with only one component from such a channel will generally be dominant. For example, the rate of mergers involving one second-generation (2G) BH—formed from the merger of first-generation (1G) BHs rather than from stellar collapse—in dense stellar clusters could be

more than an order of magnitude higher than that for mergers where both components are 2G BHs (Rodriguez et al. 2019). Motivated by this, previous studies have tested whether the m_2 distribution may provide a cleaner view of a putative PISN gap (Tong et al. 2025b; Ray & Kalogera 2025; Mould et al. 2026).

The increased support for low q at higher masses in Fig. 9 tentatively supports the picture of increasing contamination from non-standard formation pathways. In particular, this trend is consistent with 2G+1G hierarchical mergers populating a putative pair-instability gap in the primary. While under the simplest assumption for dynamically assembled 2G+1G mergers one would expect a characteristic mass ratio near $q \sim 0.5$ (Rodriguez et al. 2019; Kimball et al. 2020, 2021; Borchers et al. 2025), our inferred $p(q)$ for $m_1 \gtrsim 47\,\mathrm{M}_\odot$ with GWTC-5.0 (Fig. 9) is comparatively broad and, within uncertainties, compatible with a nearly flat distribution. It is possible that the lack of a sharper peak in $p(q)$ is merely an observational limitation from the paucity of high-mass mergers. However theoretical expectations for $p(q)$ in dense clusters also depend sensitively on the BH natal spin and pairing prescriptions (Torniamenti et al. 2024; Arca Sedda et al. 2026), and the limited number of available simulations may not yet provide an exhaustive sampling of the relevant parameter space for such systems (Wang et al. 2016; Kremer et al. 2020a; Rodriguez et al. 2019; Hong et al. 2020; Rantala et al. 2025). Thus, given both the current observational uncertainties and the model dependence of these predictions, the mass-ratio distribution alone does not provide conclusive evidence for or against 1G+2G mergers in dense star clusters, nor uniquely identifies the dominant formation channel of high-mass BHs.

In the next section, we turn to the spin distribution of BHs to identify signatures of alternate formation channels such as hierarchical mergers.

8. SIGNATURES OF HIERARCHICAL MERGER SUBPOPULATIONS

As discussed in Sec. 4.4.3, the observed GW population includes BHs with a broad distribution of spin magnitudes and tilts, with evidence for multiple subpopulations, including systems with at least one rapidly-spinning BH. While isolated binary evolution can account for some of these features, dynamical assembly in dense environments, such as AGN disks and star clusters, provides a natural pathway to the observed BBH diversity via hierarchical mergers, in which merger remnants participate in subsequent mergers (e.g., Gerosa & Fishbach 2021). Such channels can naturally produce larger BH masses, high spin magnitudes and large tilt angles, even if the 1G progenitors rotated slowly. The LVK recently reported the detection of two BBH mergers with rapid primary spins and unequal mass ratios (Abac et al. 2025c)—potential signatures of 1G+2G mergers.

If BHs above the PISN mass gap are predominantly hierarchical, BH spin properties may change across the PISN mass scale. Second-generation BHs are expected to have spin magnitudes clustering around $\chi \sim 0.7$ (Pretorius 2005; Buonanno et al. 2008; Hofmann et al. 2016; Berti & Volonteri 2008). If such remnants are retained in dense environments and subsequently merge with 1G BHs with low, isotropic spins, the $\chi_{\rm eff}$ distribution would be approximately symmetric around zero with a half-width of ∼0.47 (Antonini et al. 2025; Rodriguez et al. 2019; Baibhav et al. 2020; Fishbach et al. 2022). In contrast, alternative channels generally do not make robust predictions for $\chi_{\rm eff}$, as the resulting spins depend more sensitively on uncertain assumptions about the progenitors. The characteristic $\chi_{\rm eff}$ morphology expected from hierarchical mergers thus provides a falsifiable fingerprint of this scenario, which can be tested by searching for mass-dependent structure in the $\chi_{\rm eff}$ distribution.

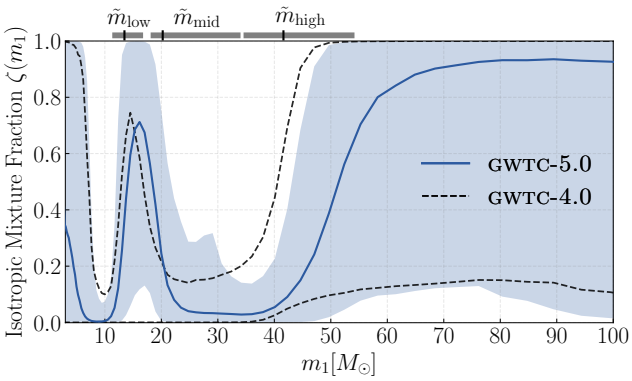

Figure 10. Mass-dependent mixture fraction $\zeta(m_1)$ between the Gaussian and uniform $\chi_{\rm eff}$ components as a function of primary BH mass obtained with the $\chi_{\rm eff}$ MIXTURE model. Here ζ denotes the fraction of systems in the uniform component. The solid line shows the posterior median inferred from GWTC-5.0 and the shaded band the corresponding 90% credible interval. The dashed lines indicate the 90% credible bounds from GWTC-4.0. The bars and markers at the top are the credible intervals of the transition masses ($\tilde{m}_{\rm low}$, $\tilde{m}_{\rm mid}$, $\tilde{m}_{\rm high}$) inferred with the $\chi_{\rm eff}$ THREE TRANSITIONS model.

8.1. *Results*

We look for transitions in the $\chi_{\rm eff}$ distribution at different masses using GWTC-5.0 data. Support for such transitions has been reported using by analyses previous datasets (Hoy et al. 2022; Antonini et al. 2025; Antonini et al. 2025; Antonini et al. 2025; Tong et al. 2025b,a; Plunkett et al. 2026; Banagiri et al. 2025b; Ray & Kalogera 2025; Farah et al. 2026; Vijaykumar et al. 2026). Meanwhile, some analyses also found evidence that the spin-magnitude distribution correlates with BH primary mass (Pierra et al. 2024; Berti et al. 2026).

We adopt the $\chi_{\rm eff}$ MIXTURE model and infer $\zeta(m_1)$, the mass-dependent fraction of systems assigned to a uniformly-distributed $\chi_{\rm eff}$ subpopulation over a narrower Gaussian component (App. G.1). Figure 10 shows the GWTC-5.0 result, which displays nontrivial peak: a pronounced low-mass feature at 10-–20 $\mathrm{M}_\odot$, where the median $\zeta(m_1)$ rises to ∼70%, followed by a dip at intermediate masses, and a second in-

crease above $\sim 40\,M_\odot$. **The data therefore support the presence of multiple mass scales at which a broader, approximately uniform $\chi_{\rm eff}$ component becomes relevant**. For the uniform $\chi_{\rm eff}$ component we find a mean $\mu = 0.04^{+0.09}_{-0.09}$ with corresponding half-width $\sigma = 0.37^{+0.13}_{-0.11}$. The narrow truncated Gaussian component has a location and a width parameter given by $\mu = 0.03^{+0.01}_{-0.01}$ and $\log_{10}\sigma = -1.24^{+0.09}_{-0.09}$, respectively. The mixture fraction $\zeta(m_1)$ remains largely unconstrained below $\sim 10\,M_\odot$.

To further localize these features in mass, we use the $\chi_{\rm eff}$ Three Transitions model. In contrast to the $\chi_{\rm eff}$ Mixture model, which allows for a smooth variation of the mixing fraction across the entire mass range, the $\chi_{\rm eff}$ Three Transitions model parametrizes the population using discrete transitions between spin regimes at transition masses $\tilde{m}_{\rm low}$, $\tilde{m}_{\rm mid}$, and $\tilde{m}_{\rm high}$ (App. G.2). We find support for a multi-transition description, with all three transition masses well constrained by the data (Fig. 22 in App. G.2). We infer transitions at $\tilde{m}_{\rm low} = 13.47^{+3.3}_{-2.16}\,M_\odot$, $\tilde{m}_{\rm mid} = 20.24^{+13.78}_{-2.14}\,M_\odot$, and $\tilde{m}_{\rm high} = 41.62^{+12.58}_{-7.06}\,M_\odot$, qualitatively consistent with $\chi_{\rm eff}$ Mixture (top axis in Fig. 10). The $\chi_{\rm eff}$ Three Transitions model does not assume, a priori, that the low-mass and high-mass uniform $\chi_{\rm eff}$ components have the same $\chi_{\rm eff}$ distribution. It finds the mean and the half-width of the Uniform component between $\tilde{m}_{\rm low}$ and $\tilde{m}_{\rm mid}$ to be $0.07^{+0.24}_{-0.15}$ and $0.51^{+0.19}_{-0.22}$, respectively. Similarly, the mean and the half-width of the Uniform component over masses of $\tilde{m}_{\rm high}$ is $0.07^{+0.24}_{-0.13}$ and $0.47^{+0.16}_{-0.23}$, respectively. These are both consistent with the expected signatures for 1G + 2G mergers. These results also broadly agree with the Truncated Gaussian Mixture Model finding from Sec. 4.4.3 that the BBH population has a dominant low-spin component and a subdominant component with at least one rapidly-spinning BH and median magnitude of $\chi \sim 0.7$ (App. B.3).

The $\chi_{\rm eff}$ Mixture model infers that the volumetric merger rate associated with the uniform and approximately-symmetric $\chi_{\rm eff}$ subpopulation is $R^{\zeta}_{\rm U} = 0.6^{+0.99}_{-0.4}\,{\rm Gpc^{-3}\,yr^{-1}}$ at $z = 0.2$. This is consistent with the $\chi_{\rm eff}$ Three Transitions model, which yields $R_{\rm U,high\,mass} = 0.38^{+0.36}_{-0.28}\,{\rm Gpc^{-3}\,yr^{-1}}$ for $m_1 > \tilde{m}_{\rm high}$ and $R_{\rm U,low\,mass} = 1.22^{+1.46}_{-0.85}\,{\rm Gpc^{-3}\,yr^{-1}}$ for $\tilde{m}_{\rm low} < m_1 < \tilde{m}_{\rm mid}$, corresponding to a total rate $R_{\rm U} = 1.63^{+1.48}_{-0.96}\,{\rm Gpc^{-3}\,yr^{-1}}$. The uniform component thus corresponds to ~1–10% of the overall BBH merger rate.

8.2. *Astrophysical implications*

8.2.1. *The high-mass sector*

The transition in spin properties above $\tilde{m}_{\rm high} \approx 40\,M_\odot$ suggests a change in the channels contributing to the observed mergers. The inferred width and mean of the uniform $\chi_{\rm eff}$ component is consistent with expectations from the standard 1G+2G merger scenario at high masses (Antonini et al. 2025; Baibhav et al. 2020; Gerosa & Berti 2017; Rodriguez et al. 2019; Fishbach et al. 2017), but many factors could lead to confusion from other channels. Furthermore, the observational uncertainty on the mixture fraction is high and we cannot rule out low occupancy of the uniform component at high masses (Fig. 10), and neither can we rule out additional formation channels.

Mergers in AGN disks (Vaccaro et al. 2024; Yang et al. 2019; Gerosa & Berti 2017; McKernan et al. 2020, 2018; Mandel & O'Shaughnessy 2010; Belczynski et al. 2020; de Mink et al. 2009; Song et al. 2016; Yoon & Langer 2005), chemically homogeneous evolution in tidally-locked massive binaries (de Mink & Mandel 2016; Marchant et al. 2016), and primordial BHs (Bardeen et al. 1972; De Luca et al. 2021, 2025; Blinnikov et al. 2016) have all been suggested as mechanisms to produce either high-mass or high-spin systems or both. Uncertainties in stellar evolution (e.g., Spruit 1999, 2002; Heger et al. 2005, 2000; Qin et al. 2018; Cantiello et al. 2014; Denissenkov & Pinsonneault 2007; Zahn et al. 2007; Fuller & Ma 2019) may also enable the formation of rapidly rotating 1G BHs with masses above $\sim 40\,M_\odot$ (Shibata & Fujibayashi 2026; Uchida et al. 2019; Croon et al. 2026; Gottlieb et al. 2025; Spera et al. 2019; Di Carlo et al. 2019; Kremer et al. 2020b; Ghodla & Eldridge 2024; Arca sedda et al. 2024a; Kıroğlu et al. 2025)

The inferred transition mass $\tilde{m}_{\rm high}$ lies suggestively close to common estimates for the lower edge of the PISN mass gap. However, the mapping between progenitor and final BH properties depends sensitively on multiple layers of uncertain stellar physics that can shift the effective onset of the gap (Costa et al. 2021; Ugolini et al. 2025; Vink et al. 2021; Renzo & Smith 2024; Mapelli et al. 2020; Fernández et al. 2018; Luo et al. 2025), leading to 1G BHs with masses above $40\,M_\odot$. This makes a direct association between the observed transition and the underlying physics difficult.

8.2.2. *The low-mass sector*

We observe a pronounced increase in the mixing fraction $\zeta(m_1)$ for $m_1 \sim 10$–$20\,M_\odot$, indicating that the uniform $\chi_{\rm eff}$ component becomes more prominent in this interval. Hierarchical mergers formed in dense stellar environments are predicted to span a broad mass range, making their presence at low primary masses possible (e.g., Tiwari & Fairhurst 2021; Mapelli et al. 2022; Santoliquido et al. 2020; Arca sedda et al. 2024b; Ye et al. 2026). However, the apparent enhancement of hierarchical-like signatures in the ~ 10–$20\,M_\odot$ interval, followed by a suppression at intermediate masses (~ 20–$40\,M_\odot$), is difficult to explain. One possible explanation lies in the structure of the 1G BH mass function, which depends sensitively on supernova physics and stellar evolution (e.g., Spera et al. 2022; Mapelli 2021). Several models predict a depletion or partial gap in the first-generation BH mass spectrum between $\sim 11\,M_\odot$ and $16\,M_\odot$ from binary stripped stars (Woosley et al. 2020; Patton & Sukhbold 2020; Ertl et al. 2020; Schneider et al. 2023; Maltsev et al. 2025; Galaudage & Lamberts 2025; Willcox et al. 2025), which could enhance the relative visibility of hierarchical mergers in this mass range. At the same time, the location and depth of such a feature remain model dependent and impacted by uncertainties in stellar evolution and cluster dynamics (e.g., Schneider et al. 2023; Chieffi & Limongi 2020; Adamcewicz

et al. 2024; Tiwari 2025; Gennari et al. 2025), complicating the interpretation.

9. BROAD POPULATION CORRELATIONS

Here we present an overview of the broad correlations between pairs of parameters in the BBH populations (Abbott et al. 2023b; Abac et al. 2025a). We discuss evidence for correlations between the distributions of mass ratio and effective inspiral spin (Sec. 9.1), and between effective inspiral spin and redshift (Sec. 9.2). Model variations and inconclusive results are shown in Apps. C and D. These results further suggest contributions to the BBH population from multiple formation pathways.

9.1. *Mass ratio and spin correlations*

Correlations between $\chi_{\rm eff}$ and q have been reported since GWTC-2.0 (Callister et al. 2021; Abbott et al. 2023b; Adamcewicz & Thrane 2022; Adamcewicz et al. 2023; Abac et al. 2025a). While GWTC-4.0 data found a correlation between q and $\chi_{\rm eff}$, we could not determine whether the $\chi_{\rm eff}$ shifts in mean, broadens, or both, with q. **In GWTC-5.0 we find decreased evidence that the mean of $\chi_{\rm eff}$ evolves with q and increased evidence that its width does, compared to GWTC-4.0.** Figure 11 shows the joint distribution of $\chi_{\rm eff}$ and q for the Linear Correlation and Spline Correlation models. The top panel shows the evolution of the width of the $\chi_{\rm eff}$ distribution with q, quantified by the standard deviation $\sigma_{\chi_{\rm eff}|q}$.

The Linear Correlation model relates both the mean and width of the $\chi_{\rm eff}$ distribution through two independent linear functions, directly parametrizing the gradient of the mean $\delta\mu_{\chi_{\rm eff}|q}$ and the gradient of the natural log of the width $\delta\ln\sigma_{\chi_{\rm eff}|q}$. This model finds that the peak of the $\chi_{\rm eff}$ distribution does not shift with q: we measure $\delta\mu_{\chi_{\rm eff}|q} = -0.03^{+0.15}_{-0.15}$, consistent with no evolution of the mean. Conversely, the model supports a more pronounced evolution of the width of the distribution with q, with more unequal-mass binaries exhibiting a wider distribution of $\chi_{\rm eff}$ values. Specifically, we obtain $\delta\ln\sigma_{\chi_{\rm eff}|q} = -2.20^{+0.69}_{-0.59}$ which rules out no evolution of the width with q at >99% credibility and implies that more unequal-mass binaries have a larger spread in $\chi_{\rm eff}$. This trend persists when we leave out the recently-discovered unequal-mass, highly-spinning systems GW241011 and GW241110, meaning that these two events do not entirely drive the correlation (see App. C).

The Spline Correlation model relates the mean and width of the $\chi_{\rm eff}$ distribution to q through two independent cubic splines, allowing for a more flexible correlation. For this model, we calculate average slopes for $\delta\mu_{\chi_{\rm eff}|q}$ and $\delta\ln\sigma_{\chi_{\rm eff}|q}$ in the range $q > 1/3$, since for smaller mass ratios the width is informed by the spline knot at $q = 0$ where we have no observations. Therefore, our calculation of $\delta\ln\sigma_{\chi_{\rm eff}|q}$ captures the Spline Correlation result's overall evolution of $\sigma_{\chi_{\rm eff}|q}$, avoiding the impact of modeling choices on local gradients. We find $\delta\mu_{\chi_{\rm eff}|q} = -0.05^{+0.23}_{-0.19}$ and $\delta\ln\sigma_{\chi_{\rm eff}|q} = -1.91^{+0.80}_{-0.73}$. This result agrees with the Linear Correlation model, showing an evolution of the width of $\chi_{\rm eff}$ with q without evolution of the mean, although uncertainties are larger due to the increased model flexibility.

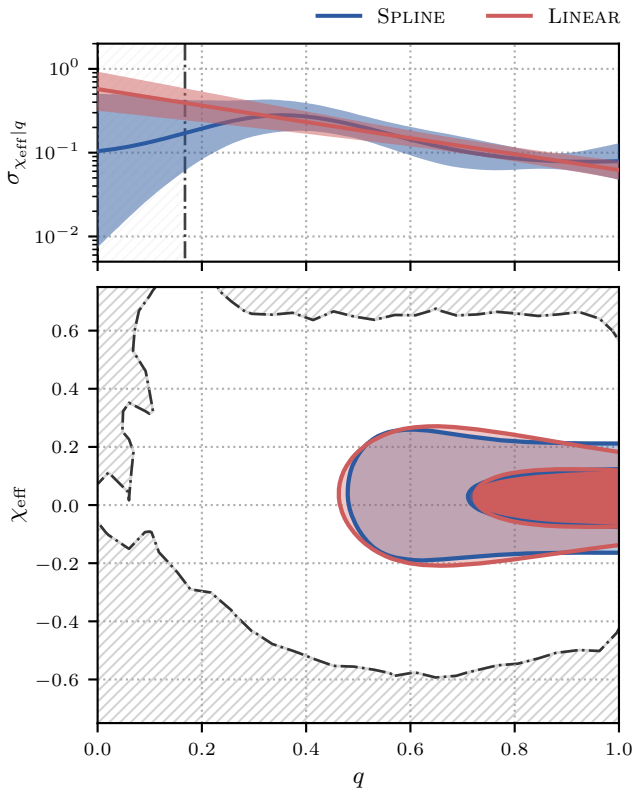

Figure 11. Top: the inferred standard deviation of the $\chi_{\rm eff}$ distribution as a function of mass ratio, for the Linear Correlation (red) and Spline Correlation (blue) models. The shaded bands show the 90% credible interval, indicating that the standard deviation tends to decrease with increasing q. Bottom: the posterior predictive distribution of the joint ($\chi_{\rm eff}$–q) distribution, for the Linear Correlation and Spline Correlation models, where the outlines contain 90% and 50% of the posterior volume. The hatching in both panels shows the areas where there are < 1% of parameter estimation samples for GWTC-5.0 observations.

We additionally test the presence of a correlation in $(q, \chi_{\rm eff})$ using a Copula Correlation model, which relates the two marginal distributions using a Frank copula via a correlation coefficient η (Adamcewicz & Thrane 2022). We find $\eta_{\chi_{\rm eff},q} < 0$ at 63% credibility, compared to 90% credibility with GWTC-4.0. However, unlike the Linear Correlation and Spline Correlation models, the Copula Correlation model cannot account for a broadening of the $\chi_{\rm eff}$ distribution with mass ratio. The decrease in $\eta_{\chi_{\rm eff},q}$ compared to GWTC-4.0 is consistent with the diminishing evidence for a direct anticorrelation between the mean of $\chi_{\rm eff}$ and q.

The wider range of $\chi_{\rm eff}$ observed at small q could be explained by a single q-dependent channel, or a mix of channels that add up to broaden $\chi_{\rm eff}$ at small q. A significant fraction of dynamically assembled BHs at lower mass ratios may widen $\chi_{\rm eff}$ (Mould et al. 2022). Hierarchical mergers of

1G+2G BHs are expected to have $q \approx 0.5$ and $\chi_1 \approx 0.7$, resulting in a broadening of $\chi_{\rm eff}$ with decreasing q. The presence of low-mass-ratio, highly-spinning binaries qualitatively agrees with the hierarchical-merger-like signatures presented in Secs. 4.4.3, 7 and 8. With a strong model, Vijaykumar et al. (2026) reported evidence for a hierarchical subpopulation of mergers in GWTC-4.0 giving rise to a similar broadening. Other mechanisms could also explain the observed trend: isolated binaries undergoing tidal spin-up, stable mass transfer, and mass ratio reversal may all result in low-q, high-spin binaries (Broekgaarden et al. 2022; Zevin & Bavera 2022; Olejak et al. 2024). However, the reduced evidence for a shift in the mean suggests that the $\chi_{\rm eff}$ distribution at unequal mass ratios is more isotropic than previously reported. This agrees with previous works that found that the aligned-spin components do not exhibit a correlation with mass ratio (Tiwari 2022, 2025; Vijaykumar et al. 2026). Such an isotropic distribution of $\chi_{\rm eff}$ is difficult to produce with most isolated formation channels although this can depend on the complex interplay between spins, natal kicks and other factors (e.g., Baibhav & Kalogera 2024).

9.2. *Redshift and spin correlations*

Evidence of a broadening of $\chi_{\rm eff}$ with increasing redshift has been observed since GWTC-3.0 (Biscoveanu et al. 2022a; Abac et al. 2025a). Figure 12 shows the joint ($\chi_{\rm eff}$–z) distribution and the width of the $\chi_{\rm eff}$ distribution as a function of redshift ($\sigma_{\chi_{\rm eff}|z}$) for the Linear Correlation and Spline Correlation models. With the Linear Correlation model we find $\delta\mu_{\chi_{\rm eff}|z} = -0.03^{+0.08}_{-0.08}$ and $\delta\ln\sigma_{\chi_{\rm eff}|z} = 0.48^{+0.31}_{-0.42}$, which indicates a preference for broadening of the width of the distribution with z at 93% credibility. The joint distribution from the Spline Correlation model qualitatively supports broadening, even if the evolution of $\sigma_{\rm eff|z}$ indicates some non-linear structure in the evolution of the width. With the Spline Correlation model we find $\delta\mu_{\chi_{\rm eff}|z} = -0.06^{+0.11}_{-0.13}$ and $\delta\ln\sigma_{\chi_{\rm eff}|z} = 0.22^{+0.47}_{-0.54}$, where we evaluate the gradients over the range where we have >1% of parameter estimation samples. This is consistent with no evolution of $\chi_{\rm eff}$ across the broad range of redshifts where we have observations.

In summary, **we find model-dependent evidence for $\chi_{\rm eff}$ broadening with redshift** with the Linear Correlation and Spline Correlation models. Evidence for this broadening is supported by additional models, which we include in App. D. The results in this section are caveated by the fact that correlations in $(\chi_{\rm eff}, z)$ are degenerate with correlations between mass and redshift, or mass and $\chi_{\rm eff}$ (Biscoveanu et al. 2022a). We discussed evidence for correlations between primary mass and $\chi_{\rm eff}$ in Sec. 8.

A broadening in $\chi_{\rm eff}$ with redshift could be a signature of multiple formation channels. For example, Farah et al. (2026) find that hierarchical mergers can produce such a broadening, due to the steeper evolution of the hierarchical BBH merger rate with redshift. Meanwhile, tidal spin up in isolated binaries can produce more *positive* $\chi_{\rm eff}$ at larger redshift due to interplay between metallicity and orbital separation, with low-metallicity environments at high redshift resulting in tighter binaries that are both tidally spun up and short-lived (Bavera et al. 2022). However, this mechanism cannot easily explain a roughly symmetric broadening under common supernova kicks (Baibhav & Kalogera 2024).

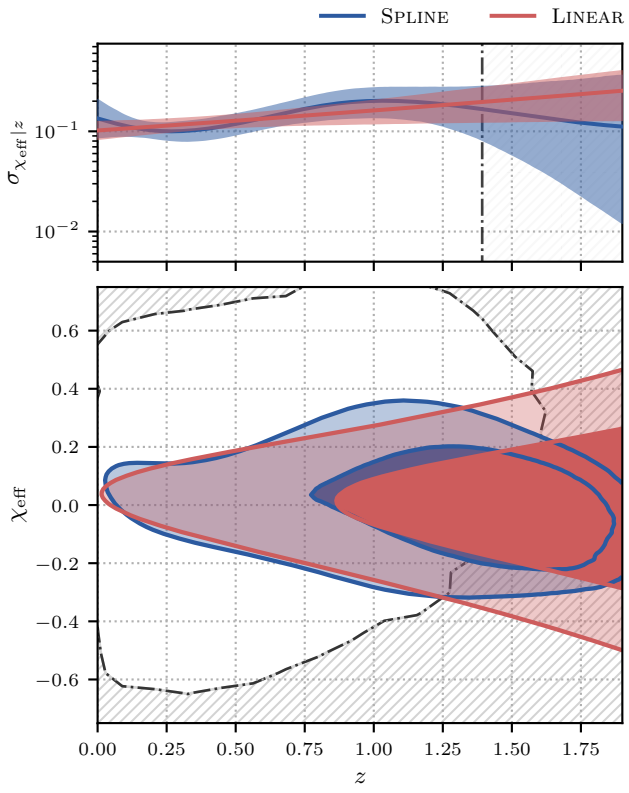

Figure 12. Top: The inferred standard deviation of the $\chi_{\rm eff}$ distribution as a function of redshift, for the Linear Correlation (red) and Spline Correlation (blue) models. The shaded bands show the 90% credible interval. Bottom: the posterior predictive distribution of the joint ($\chi_{\rm eff}$–z) distribution, for the Linear Correlation and Spline Correlation models. The outlines contain 90% and 50% of the volume. The hatched area in both plots indicates the region where there are < 1% parameter estimation samples for GWTC-5.0 observations.

10. CONCLUSION

We have presented analyses of the compact objects in the GWTC-5.0 catalog. The 267 candidate events in the dataset have further enhanced our understanding of the astrophysical properties of stellar-mass BHs. Among the most exciting findings is the growing evidence that multiple subpopulations of BHs, each with distinct properties, are producing the observed sources. Based on the number of public alerts sent about significant BBH candidates, we expect the forthcoming GWTC-6.0 catalog to yield another $\gtrsim 68$ sources (LIGO Scientific Collaboration et al. 2024), further improving our understanding of the number, rates and properties of these populations.

11. DATA AVAILABILITY

The analysis results and figure generation scripts used for this paper are released as (LIGO Scientific Collaboration et al. 2026), while the data products for estimating sensitivity can be found in (LIGO–Virgo–KAGRA Collaboration 2026a,b).

ACKNOWLEDGEMENTS

This material is based upon work supported by NSF's LIGO Laboratory, which is a major facility fully funded by the National Science Foundation. The authors also gratefully acknowledge the support of the Science and Technology Facilities Council (STFC) of the United Kingdom, the Max-Planck-Society (MPS), and the State of Niedersachsen/Germany for support of the construction of Advanced LIGO and construction and operation of the GEO 600 detector. Additional support for Advanced LIGO was provided by the Australian Research Council. The authors gratefully acknowledge the Italian Istituto Nazionale di Fisica Nucleare (INFN), the French Centre National de la Recherche Scientifique (CNRS) and the Netherlands Organization for Scientific Research (NWO) for the construction and operation of the Virgo detector and the creation and support of the EGO consortium. The authors also gratefully acknowledge research support from these agencies as well as by the Council of Scientific and Industrial Research of India, the Department of Science and Technology, India, the Science & Engineering Research Board (SERB), India, the Ministry of Human Resource Development, India, the Spanish Agencia Estatal de Investigación (AEI), the Spanish Ministerio de Ciencia, Innovación y Universidades, the European Union NextGenerationEU/PRTR (PRTR-C17.I1), the ICSC - CentroNazionale di Ricerca in High Performance Computing, Big Data and Quantum Computing, funded by the European Union NextGenerationEU, the Comunitat Autonòma de les Illes Balears through the Conselleria d'Educació i Universitats, the Conselleria d'Innovació, Universitats, Ciència i Societat Digital de la Generalitat Valenciana and the CERCA Programme Generalitat de Catalunya, Spain, the Polish National Agency for Academic Exchange, the National Science Centre of Poland and the European Union - European Regional Development Fund; the Foundation for Polish Science (FNP), the Polish Ministry of Science and Higher Education, the Swiss National Science Foundation (SNSF), the Russian Science Foundation, the European Commission, the European Social Funds (ESF), the European Regional Development Funds (ERDF), the Royal Society, the Scottish Funding Council, the Scottish Universities Physics Alliance, the Hungarian Scientific Research Fund (OTKA), the French Lyon Institute of Origins (LIO), the Belgian Fonds de la Recherche Scientifique (FRS-FNRS), Actions de Recherche Concertées (ARC) and Fonds Wetenschappelijk Onderzoek - Vlaanderen (FWO), Belgium, the Paris Île-de-France Region, the National Research, Development and Innovation Office of Hungary (NKFIH), the National Research Foundation of Korea, the Natural Sciences and Engineering Research Council of Canada (NSERC), the Canadian Foundation for Innovation (CFI), the Brazilian Ministry of Science, Technology, and Innovations, the International Center for Theoretical Physics South American Institute for Fundamental Research (ICTP-SAIFR), the Research Grants Council of Hong Kong, the National Natural Science Foundation of China (NSFC), the Israel Science Foundation (ISF), the US-Israel Binational Science Fund (BSF), the Leverhulme Trust, the Research Corporation, the National Science and Technology Council (NSTC), Taiwan, the United States Department of Energy, and the Kavli Foundation. The authors gratefully acknowledge the support of the NSF, STFC, INFN and CNRS for provision of computational resources.

This work was supported by MEXT, the JSPS Leading-edge Research Infrastructure Program, JSPS Grant-in-Aid for Specially Promoted Research 26000005, JSPS Grant-in-Aid for Scientific Research on Innovative Areas 2402: 24103006, 24103005, and 2905: JP17H06358, JP17H06361 and JP17H06364, JSPS Core-to-Core Program A. Advanced Research Networks, JSPS Grants-in-Aid for Scientific Research (S) 17H06133 and 20H05639, JSPS Grant-in-Aid for Transformative Research Areas (A) 20A203: JP20H05854, the joint research program of the Institute for Cosmic Ray Research, University of Tokyo, the National Research Foundation (NRF), the Computing Infrastructure Project of the Global Science experimental Data hub Center (GSDC) at KISTI, the Korea Astronomy and Space Science Institute (KASI), the Ministry of Science and ICT (MSIT) in Korea, Academia Sinica (AS), the AS Grid Center (ASGC) and the National Science and Technology Council (NSTC) in Taiwan under grants including the Science Vanguard Research Program, the Advanced Technology Center (ATC) of NAOJ, the Mechanical Engineering Center of KEK and Vietnam National Foundation for Science and Technology Development (NAFOSTED) 103.01-2025.147.

Additional acknowledgements for support of individual authors may be found in the following document: `https://dcc.ligo.org/LIGO-M2300033/public`. For the purpose of open access, the authors have applied a Creative Commons Attribution (CC BY) license to any Author Accepted Manuscript version arising. We request that citations to this article use 'A. G. Abac *et al.* (LIGO-Virgo-KAGRA Collaboration), ...' or similar phrasing, depending on journal convention.

REFERENCES

Aasi, J., Abbott, B. P., Abbott, R., et al. 2015, Classical and Quantum Gravity, 32, 074001, doi: 10.1088/0264-9381/32/7/074001

Abac, A. G., Abouelfettouh, I., Acernese, F., et al. 2026a, To be published in this issue. https://dcc.ligo.org/LIGO-P2500701/public

—. 2026b, To be published in this issue. https://dcc.ligo.org/LIGO-P2600152/public
—. 2026c, To be published in this issue. https://dcc.ligo.org/LIGO-P2600166/public
—. 2026d, To be published in this issue. https://dcc.ligo.org/LIGO-P2600045/public
Abac, A. G., Abbott, R., Abouelfettouh, I., et al. 2024, ApJL, 970, L34, doi: 10.3847/2041-8213/ad5beb
Abac, A. G., Abouelfettouh, I., Acernese, F., et al. 2025a, arXiv e-prints, arXiv:2508.18083, doi: 10.48550/arXiv.2508.18083
—. 2025b, PhRvL, 135, 111403, doi: 10.1103/kw5g-d732
—. 2025c, ApJL, 993, L21, doi: 10.3847/2041-8213/ae0d54
—. 2025d, ApJL, 993, L25, doi: 10.3847/2041-8213/ae0c9c
—. 2025e, arXiv e-prints, arXiv:2508.18082, doi: 10.48550/arXiv.2508.18082
—. 2026, arXiv e-prints, arXiv:2605.11703. https://arxiv.org/abs/2605.11703
Abbott, B. P., Abbott, R., Abbott, T. D., et al. 2016, PhRvL, 116, 241102, doi: 10.1103/PhysRevLett.116.241102
—. 2019, Physical Review X, 9, 031040, doi: 10.1103/PhysRevX.9.031040
—. 2020a, Classical and Quantum Gravity, 37, 045006, doi: 10.1088/1361-6382/ab5f7c
Abbott, R., Abbott, T. D., Abraham, S., et al. 2020b, ApJL, 896, L44, doi: 10.3847/2041-8213/ab960f
—. 2021a, Physical Review X, 11, 021053, doi: 10.1103/PhysRevX.11.021053
—. 2021b, ApJL, 913, L7, doi: 10.3847/2041-8213/abe949
—. 2021c, ApJL, 915, L5, doi: 10.3847/2041-8213/ac082e
Abbott, R., Abbott, T. D., Acernese, F., et al. 2022, A&A, 659, A84, doi: 10.1051/0004-6361/202141452
—. 2023a, Physical Review X, 13, 041039, doi: 10.1103/PhysRevX.13.041039
—. 2023b, Physical Review X, 13, 011048, doi: 10.1103/PhysRevX.13.011048
Acernese, F., Agathos, M., Agatsuma, K., et al. 2015, Classical and Quantum Gravity, 32, 024001, doi: 10.1088/0264-9381/32/2/024001
Adamcewicz, C., Guttman, N., Lasky, P. D., & Thrane, E. 2025, The Astrophysical Journal, 994, 261, doi: 10.3847/1538-4357/ae1370
Adamcewicz, C., Lasky, P. D., & Thrane, E. 2023, The Astrophysical Journal, 958, 13, doi: 10.3847/1538-4357/acf763
Adamcewicz, C., Lasky, P. D., Thrane, E., & Mandel, I. 2024, ApJ, 975, 253, doi: 10.3847/1538-4357/ad7ea8
Adamcewicz, C., & Thrane, E. 2022, Monthly Notices of the Royal Astronomical Society, 517, 3928, doi: 10.1093/mnras/stac2961
Adams, T., Buskulic, D., Germain, V., et al. 2016, Classical and Quantum Gravity, 33, 175012, doi: 10.1088/0264-9381/33/17/175012
Ade, P. A. R., Aghanim, N., Arnaud, M., et al. 2016, A&A, 594, A13, doi: 10.1051/0004-6361/201525830
Ai, S., Gao, H., Yuan, Y., Zhang, B., & Lan, L. 2023, Mon. Not. Roy. Astron. Soc., 526, 6260, doi: 10.1093/mnras/stad3177
Ajith, P., Hannam, M., Husa, S., et al. 2011, PhRvL, 106, 241101, doi: 10.1103/PhysRevLett.106.241101
Akutsu, T., Ando, M., Arai, K., et al. 2021, Progress of Theoretical and Experimental Physics, 2021, 05A101, doi: 10.1093/ptep/ptaa125
Alléné, C., Aubin, F., Bentara, I., et al. 2025, Classical and Quantum Gravity, 42, 105009, doi: 10.1088/1361-6382/add234
Alvarez-Lopez, S., Heinzel, J., Mould, M., & Vitale, S. 2025. https://arxiv.org/abs/2506.20731
Andres, N., Assiduo, M., Aubin, F., et al. 2022, Classical and Quantum Gravity, 39, 055002, doi: 10.1088/1361-6382/ac482a
Antonini, F., Callister, T., Dosopoulou, F., Romero-Shaw, I. M., & Chattopadhyay, D. 2025, PhRvD, 112, 063040, doi: 10.1103/nxnr-pdyx
Antonini, F., Gieles, M., Dosopoulou, F., & Chattopadhyay, D. 2023, MNRAS, 522, 466, doi: 10.1093/mnras/stad972
Antonini, F., Romero-Shaw, I., Callister, T., et al. 2025. https://arxiv.org/abs/2509.04637
Antonini, F., Romero-Shaw, I. M., & Callister, T. 2025, PhRvL, 134, 011401, doi: 10.1103/PhysRevLett.134.011401
Apostolatos, T. A., Cutler, C., Sussman, G. J., & Thorne, K. S. 1994, PhRvD, 49, 6274, doi: 10.1103/PhysRevD.49.6274
Arca sedda, M., Kamlah, A. W. H., Spurzem, R., et al. 2024a, MNRAS, 528, 5140, doi: 10.1093/mnras/stad3951
—. 2024b, MNRAS, 528, 5140, doi: 10.1093/mnras/stad3951
Arca Sedda, M., Paiella, L., Ugolini, C., et al. 2026. https://arxiv.org/abs/2603.20430
Ashton, G., Hübner, M., Lasky, P. D., et al. 2019, ApJS, 241, 27, doi: 10.3847/1538-4365/ab06fc
Aubin, F., Brighenti, F., Chierici, R., et al. 2021, Classical and Quantum Gravity, 38, 095004, doi: 10.1088/1361-6382/abe913
Azzalini, A., & Valle, A. D. 1996, Biometrika, 83, 715, doi: 10.1093/biomet/83.4.715
Baibhav, V., Gerosa, D., Berti, E., et al. 2020, PhRvD, 102, 043002, doi: 10.1103/PhysRevD.102.043002
Baibhav, V., & Kalogera, V. 2024. https://arxiv.org/abs/2412.03461
Bailyn, C. D., Jain, R. K., Coppi, P., & Orosz, J. A. 1998, ApJ, 499, 367, doi: 10.1086/305614
Banagiri, S., Callister, T. A., Adamcewicz, C., Doctor, Z., & Kalogera, V. 2025a, Astrophys. J., 990, 147, doi: 10.3847/1538-4357/adf4c6
Banagiri, S., Thrane, E., & Lasky, P. D. 2025b. https://arxiv.org/abs/2509.15646
Bardeen, J. M., Press, W. H., & Teukolsky, S. A. 1972, ApJ, 178, 347, doi: 10.1086/151796

Barkat, Z., Rakavy, G., & Sack, N. 1967, PhRvL, 18, 379, doi: 10.1103/PhysRevLett.18.379
Barr, E. D., et al. 2024, Science, 383, 275, doi: 10.1126/science.adg3005
Bavera, S. S., Fishbach, M., Zevin, M., Zapartas, E., & Fragos, T. 2022, A&A, 665, A59, doi: 10.1051/0004-6361/202243724
Belczynski, K., Heger, A., Gladysz, W., et al. 2016, A&A, 594, A97, doi: 10.1051/0004-6361/201628980
Belczynski, K., Klencki, J., Fields, C. E., et al. 2020, A&A, 636, A104, doi: 10.1051/0004-6361/201936528
Berti, E., Crescimbeni, F., Franciolini, G., et al. 2026, PhRvD, 113, 043048, doi: 10.1103/3mb7-vnft
Berti, E., & Volonteri, M. 2008, ApJ, 684, 822, doi: 10.1086/590379
Biscoveanu, S., Callister, T. A., Haster, C.-J., et al. 2022a, Astrophys. J. Lett., 932, L19, doi: 10.3847/2041-8213/ac71a8
Biscoveanu, S., Landry, P., & Vitale, S. 2022b, Mon. Not. Roy. Astron. Soc., 518, 5298, doi: 10.1093/mnras/stac3052
Blinnikov, S., Dolgov, A., Porayko, N. K., & Postnov, K. 2016, JCAP, 2016, 036, doi: 10.1088/1475-7516/2016/11/036
Bonino, A., Gamba, R., Schmidt, P., et al. 2023, PhRvD, 107, 064024, doi: 10.1103/PhysRevD.107.064024
Borchers, A., Ye, C. S., & Fishbach, M. 2025, ApJ, 987, 146, doi: 10.3847/1538-4357/addec6
Briel, M. M., Stevance, H. F., & Eldridge, J. J. 2023, MNRAS, 520, 5724, doi: 10.1093/mnras/stad399
Broekgaarden, F. S., Stevenson, S., & Thrane, E. 2022, ApJ, 938, 45, doi: 10.3847/1538-4357/ac8879
Buonanno, A., Kidder, L. E., & Lehner, L. 2008, PhRvD, 77, 026004, doi: 10.1103/PhysRevD.77.026004
Callister, T. A., & Farr, W. M. 2024, Physical Review X, 14, 021005, doi: 10.1103/PhysRevX.14.021005
Callister, T. A., Haster, C.-J., Ng, K. K. Y., Vitale, S., & Farr, W. M. 2021, ApJL, 922, L5, doi: 10.3847/2041-8213/ac2ccc
Campanelli, M., Lousto, C. O., & Zlochower, Y. 2006, PhRvD, 74, 041501, doi: 10.1103/PhysRevD.74.041501
Cannon, K., Caudill, S., Chan, C., et al. 2021, SoftwareX, 14, 100680, doi: 10.1016/j.softx.2021.100680
Cantiello, M., Mankovich, C., Bildsten, L., Christensen-Dalsgaard, J., & Paxton, B. 2014, ApJ, 788, 93, doi: 10.1088/0004-637X/788/1/93
Cheng, A. Q., Zevin, M., & Vitale, S. 2023, Astrophys. J., 955, 127, doi: 10.3847/1538-4357/aced98
Chieffi, A., & Limongi, M. 2020, ApJ, 890, 43, doi: 10.3847/1538-4357/ab6739
Colleoni, M., Ramis Vidal, F. A., García-Quirós, C., Akçay, S., & Bera, S. 2025, PhRvD, 111, 104019, doi: 10.1103/PhysRevD.111.104019
Corelli, A., Gerosa, D., Mould, M., & Fabbri, C. M. 2026, arXiv e-prints, arXiv:2603.00239, doi: 10.48550/arXiv.2603.00239
Costa, G., Bressan, A., Mapelli, M., et al. 2021, MNRAS, 501, 4514, doi: 10.1093/mnras/staa3916
Cotturone, J., Zevin, M., & Biscoveanu, S. 2026, ApJ, 998, 272, doi: 10.3847/1538-4357/ae3829
Croon, D., Gerosa, D., & Sakstein, J. 2026, MNRAS, 546, stag073, doi: 10.1093/mnras/stag073
Croon, D., & Sakstein, J. 2025, Physical Review D, 112, 063053, doi: 10.1103/53lj-hm4d
Dal Canton, T., Nitz, A. H., Gadre, B., et al. 2021, ApJ, 923, 254, doi: 10.3847/1538-4357/ac2f9a
De Luca, V., Desjacques, V., Franciolini, G., Pani, P., & Riotto, A. 2021, PhRvL, 126, 051101, doi: 10.1103/PhysRevLett.126.051101
De Luca, V., Franciolini, G., & Riotto, A. 2025, arXiv e-prints, arXiv:2508.09965, doi: 10.48550/arXiv.2508.09965
de Mink, S. E., Cantiello, M., Langer, N., et al. 2009, A&A, 497, 243, doi: 10.1051/0004-6361/200811439
de Mink, S. E., & Mandel, I. 2016, MNRAS, 460, 3545, doi: 10.1093/mnras/stw1219
Denissenkov, P. A., & Pinsonneault, M. 2007, ApJ, 655, 1157, doi: 10.1086/510345
Di Carlo, U. N., Giacobbo, N., Mapelli, M., et al. 2019, MNRAS, 487, 2947, doi: 10.1093/mnras/stz1453
Dietrich, T., Coughlin, M. W., Pang, P. T. H., et al. 2020, Science, 370, 1450, doi: 10.1126/science.abb4317
Dittmann, A. J., et al. 2024, Astrophys. J., 974, 295, doi: 10.3847/1538-4357/ad5f1e
Dominik, M., Berti, E., O'Shaughnessy, R., et al. 2015, Astrophys. J., 806, 263, doi: 10.1088/0004-637X/806/2/263
Dorozsmai, A., & Toonen, S. 2024, MNRAS, 530, 3706, doi: 10.1093/mnras/stae152
Edelman, B., Doctor, Z., Godfrey, J., & Farr, B. 2022, Astrophys. J., 924, 101, doi: 10.3847/1538-4357/ac3667
Edelman, B., Farr, B., & Doctor, Z. 2023, The Astrophysical Journal, 946, 16, doi: 10.3847/1538-4357/acb5ed
Ertl, T., Woosley, S. E., Sukhbold, T., & Janka, H.-T. 2020, ApJ, 890, 51, doi: 10.3847/1538-4357/ab6458
Essick, R., & Farr, W. 2022, arXiv e-prints, arXiv:2204.00461, doi: 10.48550/arXiv.2204.00461
Essick, R., Coughlin, M. W., Zevin, M., et al. 2025, PhRvD, 112, 102001, doi: 10.1103/44x3-hv3y
Ewing, B., Huxford, R., Singh, D., et al. 2024, PhRvD, 109, 042008, doi: 10.1103/PhysRevD.109.042008
Farag, E., Renzo, M., Farmer, R., Chidester, M. T., & Timmes, F. X. 2022, The Astrophysical Journal, 937, 112, doi: 10.3847/1538-4357/ac8b83
Farah, A. M., Fishbach, M., Essick, R., Holz, D. E., & Galaudage, S. 2022, Astrophys. J., 931, 108, doi: 10.3847/1538-4357/ac5f03
Farah, A. M., Fishbach, M., & Holz, D. E. 2024, Astrophys. J., 962, 69, doi: 10.3847/1538-4357/ad0558

Farah, A. M., Vijaykumar, A., & Fishbach, M. 2026. https://arxiv.org/abs/2601.03456
Farah, A. M., Vijaykumar, A., & Fishbach, M. 2026, ApJL, 1001, L40, doi: 10.3847/2041-8213/ae4e19
Farmer, R., Renzo, M., de Mink, S. E., Marchant, P., & Justham, S. 2019, ApJ, 887, 53, doi: 10.3847/1538-4357/ab518b
Farr, W. M. 2019, Research Notes of the American Astronomical Society, 3, 66, doi: 10.3847/2515-5172/ab1d5f
Farr, W. M., Gair, J. R., Mandel, I., & Cutler, C. 2015, PhRvD, 91, 023005, doi: 10.1103/PhysRevD.91.023005
Farr, W. M., Sravan, N., Cantrell, A., et al. 2011, ApJ, 741, 103, doi: 10.1088/0004-637X/741/2/103
Fei, Q., & Yang, Y. 2024, Communications in Theoretical Physics, 76, 075402, doi: 10.1088/1572-9494/ad4bbb
Fernández, R., Quataert, E., Kashiyama, K., & Coughlin, E. R. 2018, MNRAS, 476, 2366, doi: 10.1093/mnras/sty306
Fishbach, M., Essick, R., & Holz, D. E. 2020, Astrophys. J. Lett., 899, L8, doi: 10.3847/2041-8213/aba7b6
Fishbach, M., Holz, D. E., & Farr, B. 2017, ApJL, 840, L24, doi: 10.3847/2041-8213/aa7045
Fishbach, M., Holz, D. E., & Farr, W. M. 2018, ApJL, 863, L41, doi: 10.3847/2041-8213/aad800
Fishbach, M., Kimball, C., & Kalogera, V. 2022, ApJL, 935, L26, doi: 10.3847/2041-8213/ac86c4
Fowler, W. A., & Hoyle, F. 1964, ApJS, 9, 201, doi: 10.1086/190103
Fragione, G., Loeb, A., Kocsis, B., & Rasio, F. A. 2022, ApJ, 933, 170, doi: 10.3847/1538-4357/ac75d0
Fuller, J., & Ma, L. 2019, ApJL, 881, L1, doi: 10.3847/2041-8213/ab339b
Galaudage, S., & Lamberts, A. 2025, A&A, 694, A186, doi: 10.1051/0004-6361/202451654
Gamba, R., Breschi, M., Carullo, G., et al. 2023, Nature Astronomy, 7, 11, doi: 10.1038/s41550-022-01813-w
Gamboa, A., Buonanno, A., Enficiaud, R., et al. 2025, PhRvD, 112, 044038, doi: 10.1103/jxrc-z298
Gayathri, V., Healy, J., Lange, J., et al. 2022, Nature Astronomy, 6, 344, doi: 10.1038/s41550-021-01568-w
Gennari, V., Mastrogiovanni, S., Tamanini, N., Marsat, S., & Pierra, G. 2025, PhRvD, 111, 123046, doi: 10.1103/ftw9-7xd5
Gerosa, D., & Berti, E. 2017, PhRvD, 95, 124046, doi: 10.1103/PhysRevD.95.124046
Gerosa, D., Berti, E., O'Shaughnessy, R., et al. 2018, PhRvD, 98, 084036, doi: 10.1103/PhysRevD.98.084036
Gerosa, D., & Fishbach, M. 2021, Nature Astronomy, 5, 749, doi: 10.1038/s41550-021-01398-w
Gerosa, D., Mould, M., Gangardt, D., et al. 2021, Phys. Rev. D, 103, 064067, doi: 10.1103/PhysRevD.103.064067
Ghodla, S., & Eldridge, J. J. 2024, MNRAS, 534, 1868, doi: 10.1093/mnras/stae2198
Giacobbo, N., & Mapelli, M. 2018, Mon. Not. Roy. Astron. Soc., 480, 2011, doi: 10.1093/mnras/sty1999
Godfrey, J., Edelman, B., & Farr, B. 2023. https://arxiv.org/abs/2304.01288
Golomb, J., Isi, M., & Farr, W. M. 2024, The Astrophysical Journal, 976, 121, doi: 10.3847/1538-4357/ad8572
Gottlieb, O., Metzger, B. D., Issa, D., et al. 2025, ApJL, 993, L54, doi: 10.3847/2041-8213/ae0d81
Gupte, N., Ramos-Buades, A., Buonanno, A., et al. 2025, PhRvD, 112, 104045, doi: 10.1103/vpyp-nvfp
Gupte, N., Coleman Miller, M., Udall, R., et al. 2026, arXiv e-prints, arXiv:2603.29019, doi: 10.48550/arXiv.2603.29019
Guttman, N., Payne, E., Lasky, P. D., & Thrane, E. 2026, The Astrophysical Journal, 996, 144, doi: 10.3847/1538-4357/ae17af
Hanna, C., Caudill, S., Messick, C., et al. 2020, PhRvD, 101, 022003, doi: 10.1103/PhysRevD.101.022003
Heger, A., Fryer, C. L., Woosley, S. E., Langer, N., & Hartmann, D. H. 2003, ApJ, 591, 288, doi: 10.1086/375341
Heger, A., Langer, N., & Woosley, S. E. 2000, ApJ, 528, 368, doi: 10.1086/308158
Heger, A., Woosley, S. E., & Spruit, H. C. 2005, ApJ, 626, 350, doi: 10.1086/429868
Heinzel, J., Biscoveanu, S., & Vitale, S. 2024, Phys. Rev. D, 109, 103006, doi: 10.1103/PhysRevD.109.103006
Heinzel, J., Mould, M., Álvarez-López, S., & Vitale, S. 2025a, Phys. Rev. D, 111, 063043, doi: 10.1103/PhysRevD.111.063043
Heinzel, J., Mould, M., & Vitale, S. 2025b, Phys. Rev. D, 111, L061305, doi: 10.1103/PhysRevD.111.L061305
Heinzel, J., & Vitale, S. 2025, arXiv e-prints, arXiv:2509.07221, doi: 10.48550/arXiv.2509.07221
Hendriks, D. D., van Son, L. A. C., Renzo, M., Izzard, R. G., & Farmer, R. 2023, Monthly Notices of the Royal Astronomical Society, 526, 4130, doi: 10.1093/mnras/stad2857
Hofmann, F., Barausse, E., & Rezzolla, L. 2016, ApJL, 825, L19, doi: 10.3847/2041-8205/825/2/L19
Hong, J., Askar, A., Giersz, M., Hypki, A., & Yoon, S.-J. 2020, MNRAS, 498, 4287, doi: 10.1093/mnras/staa2677
Hoy, C., Fairhurst, S., Hannam, M., & Tiwari, V. 2022, ApJ, 928, 75, doi: 10.3847/1538-4357/ac54a3
Hussain, A., Isi, M., & Zimmerman, A. 2025. https://arxiv.org/abs/2510.20010
Hussain, A., Isi, M., & Zimmerman, A. 2026, The Astrophysical Journal, 996, 71, doi: 10.3847/1538-4357/ae1574
Huth, S., Pang, P. T. H., Tews, I., et al. 2022, Nature, 606, 276, doi: 10.1038/s41586-022-04750-w
Iglesias, H. L., Lange, J., Bartos, I., et al. 2024, ApJ, 972, 65, doi: 10.3847/1538-4357/ad5ff6
Jan, A., Tsao, B.-J., O'Shaughnessy, R., Shoemaker, D., & Laguna, P. 2026, Phys. Rev. D, 113, 024018, doi: 10.1103/zjmc-117s

Joshi, P., Tsukada, L., Hanna, C., et al. 2025a, arXiv e-prints, arXiv:2506.06497, doi: 10.48550/arXiv.2506.06497
Joshi, P., Niu, W., Hanna, C., et al. 2025b, arXiv e-prints, arXiv:2505.23959, doi: 10.48550/arXiv.2505.23959
Karathanasis, C., Mukherjee, S., & Mastrogiovanni, S. 2023, Monthly Notices of the Royal Astronomical Society, 523, 4539, doi: 10.1093/mnras/stad1373
Kimball, C., Talbot, C., Berry, C. P. L., et al. 2020, ApJ, 900, 177, doi: 10.3847/1538-4357/aba518
—. 2021, The Astrophysical Journal, 915, L35, doi: 10.3847/2041-8213/ac0aef
King, A. R., & Kolb, U. 1999, MNRAS, 305, 654, doi: 10.1046/j.1365-8711.1999.02482.x
Kinugawa, T., Inayoshi, K., Hotokezaka, K., Nakauchi, D., & Nakamura, T. 2014, MNRAS, 442, 2963, doi: 10.1093/mnras/stu1022
Kinugawa, T., Nakamura, T., & Nakano, H. 2021, MNRAS, 504, L28, doi: 10.1093/mnrasl/slab032
Kıroğlu, F., Lombardi, J. C., Kremer, K., Vanderzyden, H. D., & Rasio, F. A. 2025, Astrophys. J. Lett., 983, L9, doi: 10.3847/2041-8213/adc263
Kıroğlu, F., Kremer, K., & Rasio, F. A. 2025, ApJL, 994, L37, doi: 10.3847/2041-8213/ae1eeb
Kishore Roy, S., van Son, L. A. C., & Farr, W. M. 2025a, Classical and Quantum Gravity, 42, 225008, doi: 10.1088/1361-6382/ae1921
—. 2025b, Classical and Quantum Gravity, 42, 225008, doi: 10.1088/1361-6382/ae1921
Klimenko, S., Mohanty, S., Rakhmanov, M., & Mitselmakher, G. 2005, PhRvD, 72, 122002, doi: 10.1103/PhysRevD.72.122002
Klimenko, S., Yakushin, I., Mercer, A., & Mitselmakher, G. 2008, Classical and Quantum Gravity, 25, 114029, doi: 10.1088/0264-9381/25/11/114029
Klimenko, S., Vedovato, G., Drago, M., et al. 2016, PhRvD, 93, 042004, doi: 10.1103/PhysRevD.93.042004
Koehn, H., et al. 2025, Phys. Rev. X, 15, 021014, doi: 10.1103/PhysRevX.15.021014
Koloniari, A. E., Koursoumpa, E. C., Nousi, P., et al. 2025, Machine Learning: Science and Technology, 6, 015054, doi: 10.1088/2632-2153/adb5ed
Kreidberg, L., Bailyn, C. D., Farr, W. M., & Kalogera, V. 2012, ApJ, 757, 36, doi: 10.1088/0004-637X/757/1/36
Kremer, K., Ye, C. S., Rui, N. Z., et al. 2020a, ApJS, 247, 48, doi: 10.3847/1538-4365/ab7919
Kremer, K., Spera, M., Becker, D., et al. 2020b, ApJ, 903, 45, doi: 10.3847/1538-4357/abb945
Kumar, P., & Dent, T. 2024, PhRvD, 110, 043036, doi: 10.1103/PhysRevD.110.043036
Lalleman, M., Turbang, K., Callister, T., & van Remortel, N. 2025, A&A, 698, A85, doi: 10.1051/0004-6361/202553941
Landry, P., Essick, R., & Chatziioannou, K. 2020, PhRvD, 101, 123007, doi: 10.1103/PhysRevD.101.123007
Landry, P., & Read, J. S. 2021, ApJL, 921, L25, doi: 10.3847/2041-8213/ac2f3e
Legred, I., Chatziioannou, K., Essick, R., Han, S., & Landry, P. 2021, PhRvD, 104, 063003, doi: 10.1103/PhysRevD.104.063003
Lenon, A. K., Nitz, A. H., & Brown, D. A. 2020, MNRAS, 497, 1966, doi: 10.1093/mnras/staa2120
Li, Y.-J., Tang, S.-P., Gao, S.-J., Wu, D.-C., & Wang, Y.-Z. 2024, ApJ, 977, 67, doi: 10.3847/1538-4357/ad83b5
Li, Y.-J., Wang, Y.-Z., Tang, S.-P., et al. 2022, The Astrophysical Journal, 933, L14, doi: 10.3847/2041-8213/ac78dd
LIGO–Virgo–KAGRA Collaboration. 2026a, GWTC-5.0: O4a+O4b Search Sensitivity Estimates, Zenodo, doi: 10.5281/zenodo.19500064
—. 2026b, GWTC-5.0: Cumulative Search Sensitivity Estimates, Zenodo, doi: 10.5281/zenodo.19500052
LIGO Scientific Collaboration, Virgo Collaboration, & KAGRA Collaboration. 2024, GraceDB: Gravitational-Wave Candidate Event Database — Public Alerts, O4, https://gracedb.ligo.org/superevents/public/O4/
—. 2026, GWTC-5.0: Population Properties of Merging Compact Binaries, https://doi.org/10.5281/zenodo.20292639, Zenodo, doi: 10.5281/zenodo.20292639
Loredo, T. J., & Lamb, D. Q. 2002, Physical Review D, 65, 063002, doi: 10.1103/PhysRevD.65.063002
Luo, R., Zhu, C., Lü, G., et al. 2025, A&A, 704, A46, doi: 10.1051/0004-6361/202555081
Madau, P., & Dickinson, M. 2014, Ann. Rev. Astron. Astrophys., 52, 415, doi: 10.1146/annurev-astro-081811-125615
Magaña Hernandez, I., & Palmese, A. 2024, arXiv e-prints, arXiv:2407.02460, doi: 10.48550/arXiv.2407.02460
Magaña Hernandez, I., & Palmese, A. 2025, Phys. Rev. D, 111, 083031, doi: 10.1103/PhysRevD.111.083031
Mali, U., & Essick, R. 2025, Astrophys. J., 980, 85, doi: 10.3847/1538-4357/ad9de7
Mali, U., & Essick, R. 2026, PhRvD, 113, 083013, doi: 10.1103/w6gp-lgfk
Maltsev, K., Schneider, F. R. N., Mandel, I., et al. 2025, A&A, 700, A20, doi: 10.1051/0004-6361/202554931
Mandel, I., & de Mink, S. E. 2016, MNRAS, 458, 2634, doi: 10.1093/mnras/stw379
Mandel, I., Farr, W. M., & Gair, J. R. 2019, MNRAS, 486, 1086, doi: 10.1093/mnras/stz896
Mandel, I., & O'Shaughnessy, R. 2010, Classical and Quantum Gravity, 27, 114007, doi: 10.1088/0264-9381/27/11/114007
Mapelli, M. 2021, in Handbook of Gravitational Wave Astronomy, ed. C. Bambi, S. Katsanevas, & K. D. Kokkotas, 16, doi: 10.1007/978-981-15-4702-7_16-1

Mapelli, M., Bouffanais, Y., Santoliquido, F., Arca Sedda, M., & Artale, M. C. 2022, MNRAS, 511, 5797, doi: 10.1093/mnras/stac422

Mapelli, M., Spera, M., Montanari, E., et al. 2020, ApJ, 888, 76, doi: 10.3847/1538-4357/ab584d

Marchant, P., Langer, N., Podsiadlowski, P., Tauris, T. M., & Moriya, T. J. 2016, A&A, 588, A50, doi: 10.1051/0004-6361/201628133

Marchant, P., Renzo, M., Farmer, R., et al. 2019a, The Astrophysical Journal, 882, 36, doi: 10.3847/1538-4357/ab3426

—. 2019b, ApJ, 882, 36, doi: 10.3847/1538-4357/ab3426

Margalit, B., & Metzger, B. D. 2017, ApJL, 850, L19, doi: 10.3847/2041-8213/aa991c

McKernan, B., Ford, K. E. S., O'Shaugnessy, R., & Wysocki, D. 2020, MNRAS, 494, 1203, doi: 10.1093/mnras/staa740

McKernan, B., Ford, K. E. S., Bellovary, J., et al. 2018, ApJ, 866, 66, doi: 10.3847/1538-4357/aadae5

McMillin, P., Wagner, K. J., Ficarra, G., Lousto, C. O., & O'Shaughnessy, R. 2025, arXiv e-prints, arXiv:2507.22862, doi: 10.48550/arXiv.2507.22862

Mehta, A. K., Olsen, S., Wadekar, D., et al. 2025a, Phys. Rev. D, 111, 024049, doi: 10.1103/PhysRevD.111.024049

Mehta, A. K., Wadekar, D., Anantpurkar, I., et al. 2025b, Phys. Rev. D, 112, 124023, doi: 10.1103/mc85-361v

Messick, C., Blackburn, K., Brady, P., et al. 2017, PhRvD, 95, 042001, doi: 10.1103/PhysRevD.95.042001

Miller, S., Callister, T. A., & Farr, W. M. 2020, ApJ, 895, 128, doi: 10.3847/1538-4357/ab80c0

Miller, S. J., Winney, S., Chatziioannou, K., & Meyers, P. M. 2026. https://arxiv.org/abs/2604.06090

Mishra, T., Bhaumik, S., Gayathri, V., et al. 2025, PhRvD, 111, 023054, doi: 10.1103/PhysRevD.111.023054

Morras, G., Pratten, G., & Schmidt, P. 2025. https://arxiv.org/abs/2503.15393

Mould, M., Gerosa, D., & Taylor, S. R. 2022, Phys. Rev. D, 106, 103013, doi: 10.1103/PhysRevD.106.103013

Mould, M., Heinzel, J., Alvarez-Lopez, S., et al. 2026. https://arxiv.org/abs/2602.11282

Nathanail, A., Most, E. R., & Rezzolla, L. 2021, ApJL, 908, L28, doi: 10.3847/2041-8213/abdfc6

Neijssel, C. J., Vigna-Gómez, A., Stevenson, S., et al. 2019, MNRAS, 490, 3740, doi: 10.1093/mnras/stz2840

Nitz, A. H., Capano, C., Nielsen, A. B., et al. 2019, ApJ, 872, 195, doi: 10.3847/1538-4357/ab0108

Nitz, A. H., Capano, C. D., Kumar, S., et al. 2021, ApJ, 922, 76, doi: 10.3847/1538-4357/ac1c03

Nitz, A. H., Dal Canton, T., Davis, D., & Reyes, S. 2018, PhRvD, 98, 024050, doi: 10.1103/PhysRevD.98.024050

Nitz, A. H., Dent, T., Dal Canton, T., Fairhurst, S., & Brown, D. A. 2017, ApJ, 849, 118, doi: 10.3847/1538-4357/aa8f50

Nitz, A. H., Kumar, S., Wang, Y.-F., et al. 2023, ApJ, 946, 59, doi: 10.3847/1538-4357/aca591

Nitz, A. H., Dent, T., Davies, G. S., et al. 2020, ApJ, 891, 123, doi: 10.3847/1538-4357/ab733f

Niu, W., et al. 2025. https://arxiv.org/abs/2509.09741

Olejak, A., & Belczynski, K. 2021, ApJL, 921, L2, doi: 10.3847/2041-8213/ac2f48

Olejak, A., Belczynski, K., & Ivanova, N. 2021, A&A, 651, A100, doi: 10.1051/0004-6361/202140520

Olejak, A., Klencki, J., Xu, X.-T., et al. 2024, A&A, 689, A305, doi: 10.1051/0004-6361/202450480

Olsen, S., Venumadhav, T., Mushkin, J., et al. 2022, PhRvD, 106, 043009, doi: 10.1103/PhysRevD.106.043009

O'Shea, E., & Kumar, P. 2023, PhRvD, 108, 104018, doi: 10.1103/PhysRevD.108.104018

Patton, R. A., & Sukhbold, T. 2020, MNRAS, 499, 2803, doi: 10.1093/mnras/staa3029

Payne, E., & Thrane, E. 2023, Physical Review Research, 5, 023013, doi: 10.1103/PhysRevResearch.5.023013

Phukon, K. S., Schmidt, P., Morras, G., & Pratten, G. 2025, arXiv e-prints, arXiv:2512.10803, doi: 10.48550/arXiv.2512.10803

Pierra, G., Mastrogiovanni, S., & Perriès, S. 2024, arXiv e-prints, arXiv:2406.01679, doi: 10.48550/arXiv.2406.01679

Pierra, G., & Papadopoulos, A. 2026, arXiv e-prints, arXiv:2601.03257, doi: 10.48550/arXiv.2601.03257

Planas, M. d. L., Husa, S., Ramos-Buades, A., & Valencia, J. 2025, Astrophys. J., 995, 47, doi: 10.3847/1538-4357/ae1d7d

Planas, M. d. L., Ramos-Buades, A., García-Quirós, C., et al. 2025, PhRvD, 112, 123004, doi: 10.1103/cv75-y8dr

Plunkett, C., Callister, T., Zevin, M., & Vitale, S. 2026. https://arxiv.org/abs/2601.07908

Pompili, L., Buonanno, A., Estellés, H., et al. 2023, PhRvD, 108, 124035, doi: 10.1103/PhysRevD.108.124035

Pratten, G., García-Quirós, C., Colleoni, M., et al. 2021, PhRvD, 103, 104056, doi: 10.1103/PhysRevD.103.104056

Pretorius, F. 2005, PhRvL, 95, 121101, doi: 10.1103/PhysRevLett.95.121101

Qin, Y., Fragos, T., Meynet, G., et al. 2018, A&A, 616, A28, doi: 10.1051/0004-6361/201832839

Racine, É. 2008, PhRvD, 78, 044021, doi: 10.1103/PhysRevD.78.044021

Rakavy, G., & Shaviv, G. 1967, ApJ, 148, 803, doi: 10.1086/149204

Ramos-Buades, A., Buonanno, A., Estellés, H., et al. 2023a, PhRvD, 108, 124037, doi: 10.1103/PhysRevD.108.124037

Ramos-Buades, A., Buonanno, A., & Gair, J. 2023b, PhRvD, 108, 124063, doi: 10.1103/PhysRevD.108.124063

Rantala, A., Lahén, N., Naab, T., Escobar, G. J., & Iorio, G. 2025, MNRAS, 543, 2130, doi: 10.1093/mnras/staf1519

Ray, A., Hernandez, I. M., Breivik, K., & Creighton, J. 2025, The Astrophysical Journal, 991, 17, doi: 10.3847/1538-4357/adf22a
Ray, A., & Kalogera, V. 2025. https://arxiv.org/abs/2510.18867
Ray, A., & Kalogera, V. 2026, ApJL, 998, L20, doi: 10.3847/2041-8213/ae374d
Ray, A., Magaña Hernandez, I., Mohite, S., Creighton, J., & Kapadia, S. 2023, Astrophys. J., 957, 37, doi: 10.3847/1538-4357/acf452
Ray, A., Mukherjee, S., Zevin, M., & Kalogera, V. 2026, arXiv e-prints, arXiv:2603.17987, doi: 10.48550/arXiv.2603.17987
Ray, A., Niu, W., Sakon, S., et al. 2023, arXiv e-prints, arXiv:2306.07190, doi: 10.48550/arXiv.2306.07190
Renzo, M., & Smith, N. 2024, arXiv e-prints, arXiv:2407.16113, doi: 10.48550/arXiv.2407.16113
Rezzolla, L., Most, E. R., & Weih, L. R. 2018, ApJL, 852, L25, doi: 10.3847/2041-8213/aaa401
Rodriguez, C. L., Amaro-Seoane, P., Chatterjee, S., & Rasio, F. A. 2018, PhRvL, 120, 151101, doi: 10.1103/PhysRevLett.120.151101
Rodriguez, C. L., Zevin, M., Amaro-Seoane, P., et al. 2019, PhRvD, 100, 043027, doi: 10.1103/PhysRevD.100.043027
Rodriguez, C. L., Zevin, M., Pankow, C., Kalogera, V., & Rasio, F. A. 2016, ApJL, 832, L2, doi: 10.3847/2041-8205/832/1/L2
Romero-Shaw, I., Lasky, P. D., & Thrane, E. 2022a, ApJ, 940, 171, doi: 10.3847/1538-4357/ac9798
Romero-Shaw, I., Lasky, P. D., Thrane, E., & Calderón Bustillo, J. 2020a, ApJL, 903, L5, doi: 10.3847/2041-8213/abbe26
Romero-Shaw, I. M., Lasky, P. D., & Thrane, E. 2019, MNRAS, 490, 5210, doi: 10.1093/mnras/stz2996
Romero-Shaw, I. M., Thrane, E., & Lasky, P. D. 2022b, PASA, 39, e025, doi: 10.1017/pasa.2022.24
Romero-Shaw, I. M., Talbot, C., Biscoveanu, S., et al. 2020b, MNRAS, 499, 3295, doi: 10.1093/mnras/staa2850
Ruiz, M., Shapiro, S. L., & Tsokaros, A. 2018, PhRvD, 97, 021501, doi: 10.1103/PhysRevD.97.021501
Rutherford, N., Mendes, M., Svensson, I., et al. 2024, ApJL, 971, L19, doi: 10.3847/2041-8213/ad5f02
Sachdev, S., Caudill, S., Fong, H., et al. 2019, arXiv e-prints, arXiv:1901.08580, doi: 10.48550/arXiv.1901.08580
Sadiq, J., Dent, T., & Lorenzo-Medina, A. 2025a, Physical Review D, 112, 123054, doi: 10.1103/117r-lsw2
—. 2025b, PhRvD, 112, 083028, doi: 10.1103/j9fq-nkl3
Sakon, S., Tsukada, L., Fong, H., et al. 2024, PhRvD, 109, 044066, doi: 10.1103/PhysRevD.109.044066
Santoliquido, F., Mapelli, M., Bouffanais, Y., et al. 2020, ApJ, 898, 152, doi: 10.3847/1538-4357/ab9b78
Schmidt, P., Hannam, M., & Husa, S. 2012, PhRvD, 86, 104063, doi: 10.1103/PhysRevD.86.104063
Schmidt, P., Hannam, M., Husa, S., & Ajith, P. 2011, PhRvD, 84, 024046, doi: 10.1103/PhysRevD.84.024046
Schmidt, P., Ohme, F., & Hannam, M. 2015, PhRvD, 91, 024043, doi: 10.1103/PhysRevD.91.024043
Schneider, F. R. N., Podsiadlowski, P., & Laplace, E. 2023, ApJL, 950, L9, doi: 10.3847/2041-8213/acd77a
Shibata, M., & Fujibayashi, S. 2026, ApJ, 996, 57, doi: 10.3847/1538-4357/ae22d4
Song, H. F., Meynet, G., Maeder, A., Ekström, S., & Eggenberger, P. 2016, A&A, 585, A120, doi: 10.1051/0004-6361/201526074
Spearman, C. 1904, The American Journal of Psychology, 15, 72, doi: 10.2307/1412159
Spera, M., & Mapelli, M. 2017, MNRAS, 470, 4739, doi: 10.1093/mnras/stx1576
Spera, M., Mapelli, M., Giacobbo, N., et al. 2019, MNRAS, 485, 889, doi: 10.1093/mnras/stz359
Spera, M., Trani, A. A., & Mencagli, M. 2022, Galaxies, 10, 76, doi: 10.3390/galaxies10040076
Spruit, H. C. 1999, A&A, 349, 189, doi: 10.48550/arXiv.astro-ph/9907138
—. 2002, A&A, 381, 923, doi: 10.1051/0004-6361:20011465
Sridhar, O., Ray, A., & Kalogera, V. 2025. https://arxiv.org/abs/2511.22093
Stevenson, S., Sampson, M., Powell, J., et al. 2019, ApJ, 882, 121, doi: 10.3847/1538-4357/ab3981
Talbot, C., & Golomb, J. 2023, MNRAS, 526, 3495, doi: 10.1093/mnras/stad2968
Talbot, C., & Thrane, E. 2018, ApJ, 856, 173, doi: 10.3847/1538-4357/aab34c
Thrane, E., & Talbot, C. 2019, PASA, 36, e010, doi: 10.1017/pasa.2019.2
Tiwari, A., Bhat, S. A., Shaikh, M. A., & Kapadia, S. J. 2025, Astrophys. J., 995, 48, doi: 10.3847/1538-4357/ae1d74
Tiwari, V. 2018, Classical and Quantum Gravity, 35, 145009, doi: 10.1088/1361-6382/aac89d
Tiwari, V. 2022, Astrophys. J., 928, 155, doi: 10.3847/1538-4357/ac589a
Tiwari, V. 2024, Monthly Notices of the Royal Astronomical Society, 527, 298, doi: 10.1093/mnras/stad3155
—. 2025, ApJ, 995, 177, doi: 10.3847/1538-4357/ae2260
Tiwari, V. 2025. https://arxiv.org/abs/2510.25579
Tiwari, V., & Fairhurst, S. 2021, The Astrophysical Journal, 913, L19, doi: 10.3847/2041-8213/abfbe7
Tiwari, V., & Fairhurst, S. 2021, Astrophys. J. Lett., 913, L19, doi: 10.3847/2041-8213/abfbe7
Tong, H., Callister, T. A., Fishbach, M., et al. 2025a. https://arxiv.org/abs/2511.05316
Tong, H., et al. 2025b. https://arxiv.org/abs/2509.04151
Torniamenti, S., Mapelli, M., Périgois, C., et al. 2024, A&A, 688, A148, doi: 10.1051/0004-6361/202449272
Tsukada, L., Joshi, P., Adhicary, S., et al. 2023, PhRvD, 108, 043004, doi: 10.1103/PhysRevD.108.043004

Uchida, H., Shibata, M., Takahashi, K., & Yoshida, T. 2019, ApJ, 870, 98, doi: 10.3847/1538-4357/aaf39e

Ugolini, C., Limongi, M., Schneider, R., et al. 2025, A&A, 695, A122, doi: 10.1051/0004-6361/202451483

Usman, S. A., Nitz, A. H., Harry, I. W., et al. 2016, Classical and Quantum Gravity, 33, 215004, doi: 10.1088/0264-9381/33/21/215004

Vaccaro, M. P., Mapelli, M., Périgois, C., et al. 2024, A&A, 685, A51, doi: 10.1051/0004-6361/202348509

van den Heuvel, E. P. J., & Tauris, T. M. 2020, Science, 368, eaba3282, doi: 10.1126/science.aba3282

van Son, L. A. C., de Mink, S. E., Chruslinska, M., et al. 2022a, doi: 10.3847/1538-4357/acbf51

van Son, L. A. C., de Mink, S. E., Renzo, M., et al. 2022b, Astrophys. J., 940, 184, doi: 10.3847/1538-4357/ac9b0a

van Son, L. A. C., de Mink, S. E., Callister, T., et al. 2022c, Astrophys. J., 931, 17, doi: 10.3847/1538-4357/ac64a3

Varma, V., Field, S. E., Scheel, M. A., et al. 2019, Physical Review Research, 1, 033015, doi: 10.1103/PhysRevResearch.1.033015

Venumadhav, T., Zackay, B., Roulet, J., Dai, L., & Zaldarriaga, M. 2019, PhRvD, 100, 023011, doi: 10.1103/PhysRevD.100.023011

—. 2020, PhRvD, 101, 083030, doi: 10.1103/PhysRevD.101.083030

Vijaykumar, A., Farah, A. M., & Fishbach, M. 2026, ApJL, 999, L30, doi: 10.3847/2041-8213/ae4878

Vijaykumar, A., Farah, A. M., & Fishbach, M. 2026. https://arxiv.org/abs/2601.03457

Vink, J. S., Higgins, E. R., Sander, A. A. C., & Sabhahit, G. N. 2021, MNRAS, 504, 146, doi: 10.1093/mnras/stab842

Vitale, S., Biscoveanu, S., & Talbot, C. 2022, Astron. Astrophys., 668, L2, doi: 10.1051/0004-6361/202245084

Vitale, S., Gerosa, D., Farr, W. M., & Taylor, S. R. 2022, in Handbook of Gravitational Wave Astronomy, ed. C. Bambi, S. Katsanevas, & K. D. Kokkotas, 45, doi: 10.1007/978-981-15-4702-7_45-1

Vitale, S., Lynch, R., Sturani, R., & Graff, P. 2017, Classical and Quantum Gravity, 34, 03LT01, doi: 10.1088/1361-6382/aa552e

Wadekar, D., Roulet, J., Venumadhav, T., et al. 2023. https://arxiv.org/abs/2312.06631

Wang, L., Spurzem, R., Aarseth, S., et al. 2016, MNRAS, 458, 1450, doi: 10.1093/mnras/stw274

Wang, S., Zhao, X., Feng, F., et al. 2024, Nature Astronomy, 8, 1583, doi: 10.1038/s41550-024-02359-9

Wiktorowicz, G., Wyrzykowski, Ł., Chruslinska, M., et al. 2019, doi: 10.3847/1538-4357/ab45e6

Willcox, R., Schneider, F. R. N., Laplace, E., et al. 2025, arXiv e-prints, arXiv:2510.07573, doi: 10.48550/arXiv.2510.07573

Winch, E. R. J., Sabhahit, G. N., Vink, J. S., & Higgins, E. R. 2025, MNRAS, 540, 90, doi: 10.1093/mnras/staf676

Wolfe, N. E., Vitale, S., & Zevin, M. 2026, arXiv e-prints, arXiv:2605.05300, doi: 10.48550/arXiv.2605.05300

Woosley, S. E. 2017a, The Astrophysical Journal, 836, 244, doi: 10.3847/1538-4357/836/2/244

—. 2017b, ApJ, 836, 244, doi: 10.3847/1538-4357/836/2/244

Woosley, S. E., Blinnikov, S., & Heger, A. 2007, Nature, 450, 390, doi: 10.1038/nature06333

Woosley, S. E., Sukhbold, T., & Janka, H.-T. 2020, ApJ, 896, 56, doi: 10.3847/1538-4357/ab8cc1

Wu, S., Cao, Z., & Zhu, Z.-H. 2020, MNRAS, 495, 466, doi: 10.1093/mnras/staa1176

Xu, Y., Valencia, J., Estellés Estrella, H., et al. 2025, arXiv e-prints, arXiv:2512.19513, doi: 10.48550/arXiv.2512.19513

Yang, Y., Bartos, I., Gayathri, V., et al. 2019, PhRvL, 123, 181101, doi: 10.1103/PhysRevLett.123.181101

Ye, C. S., Fishbach, M., Kremer, K., & Reina-Campos, M. 2026, ApJ, 997, 267, doi: 10.3847/1538-4357/ae317f

Yoon, S.-C., & Langer, N. 2005, A&A, 443, 643, doi: 10.1051/0004-6361:20054030

Zackay, B., Venumadhav, T., Dai, L., Roulet, J., & Zaldarriaga, M. 2019, PhRvD, 100, 023007, doi: 10.1103/PhysRevD.100.023007

Zahn, J.-P., Brun, A. S., & Mathis, S. 2007, A&A, 474, 145, doi: 10.1051/0004-6361:20077653

Zevin, M., & Bavera, S. S. 2022, ApJ, 933, 86, doi: 10.3847/1538-4357/ac6f5d

APPENDIX

A. DATASET AND METHODS

A.1. *Waveform model choices*

For newly identified CBC candidates in O4b, we use posterior samples generated with the Bilby package (Ashton et al. 2019; Romero-Shaw et al. 2020b).

For BBH candidates from O1 - third observing run (O3), all analyses in this paper made the same waveform choices as detailed in Abac et al. (2025e). For events in fourth observing run (O4), our analyses broadly made two different choices of waveforms. All analyses used posterior samples generated with NRSur7dq4 (Varma et al. 2019) when available. When samples with NRSur7dq4 were not available, e.g. when the signal duration is too long to be analyzed with it, PixelPop, FullPop, Linear Correlation and the Spline Correlation models used posterior draws generated with the IMRPhenomXPHM_SpinTaylor waveform (Pratten et al. 2021; Colleoni et al. 2025). The Default BBH model, the Three Subpopulation model, Binned Gaussian Process, Isolated Peak, Truncated Gaussian Mixture Model, $\chi_{\rm eff}$ Three Transitions, Bivariate Skewed $\chi_{\rm eff}/\chi_{\rm p}$, $\chi_{\rm eff}$ Mixture, and the copula analyses used Mixed samples – a mixture of posterior draws from the IMRPhenomXPHM_SpinTaylor and SEOBNRv5PHM waveforms analyses (Ramos-Buades et al. 2023a; Pompili et al. 2023) – for O4a and samples from IMRPhenomXPHM_SpinTaylor for O4b [3].

Our full-spectrum models also made different waveform choices for NS-containing events. For the BNSs mergers, GW170817 and GW190425, both FullPop and PixelPop used IMRPhenomPv2_NRTidal. For GW200105 and GW200115 PixelPop used Mixed samples while FullPop used IMRPhenomNSBH. Finally for GW230529_181500, PixelPop used draws from IMRPhenomNSBH while FullPop used Mixed samples.

We note that we do not expect our population inferences to be sensitive to the choices between these waveforms.

A.2. *Estimation of the detector network sensitivity*

We numerically estimate the sensitivity of the detector network (i.e., measure $\xi(\Lambda)$) during O3, O4a and O4b by re-weighting a large set of simulated signals (injections) added to real data and searched by the same pipelines used to produce the actual catalog (Abac et al. 2025a; Essick et al. 2025). This yields a list of $\sim 1.21 \times 10^6$ ($\sim 1.11 \times 10^6$) injections above the detection threshold of FAR< 1 per year (< 0.25 per year). For O1 and second observing run (O2) only, a different procedure is used, which thresholds on SNR instead of FAR (Abbott et al. 2023b), yielding $\sim 3.70 \times 10^5$ injections above SNR$= 10$.

B. OVERVIEW MODELS

B.1. PixelPop

The PixelPop analysis employs a high-resolution binned model that is able to infer joint population distribution of multiple CBC parameters and their correlations with minimal assumptions (Heinzel et al. 2024). To accomplish this, the joint space of CBC parameters is finely binned and the comoving merger rate density in each bin is inferred as an independent parameter using hierarchical Bayesian inference. To enforce a notion of smoothness, the rate within each bin β is coupled to its nearest neighbors using a log-normal intrinsic conditional autoregressive prior (ICAR),

$$p\left(\ln \mathcal{R}_\beta \,\middle|\, \{\ln \mathcal{R}_{b\neq\beta}\}, \sigma\right) \propto \exp\left[-\sum_b \frac{(\ln \mathcal{R}_\beta - \ln \mathcal{R}_b)^2}{2\sigma^2}\right]. \tag{B1}$$

where b is an index over the nearest neighbors of bin β and the global parameter σ defines the smoothness of the ICAR. In practice, the joint prior density over all bins can be computed simultaneously as the matrix equation shown in Heinzel et al. (2024). Here, we take the intrinsic CAR limit to improve computational efficiency without making sacrifices on the inference fidelity. See the discussion in App. B of Alvarez-Lopez et al. (2025).

In this paper, we generally use variants of PixelPop that model the joint population distributions of one or two CBC parameters, with 100 bins per dimension. Therefore, our one- and two-dimensional PixelPop models have 10^2 and 10^4 rate parameters in total, respectively. Table 3 shows the different variants used in this papers along with the relevant sections. For CBC parameters that are not binned, we fall back on the strongly-parameterized models described in Tab. 1. We use a uniform prior on $\ln \sigma \in [-3, 5]$. We direct the reader to Heinzel et al. (2024, 2025b) and Alvarez-Lopez et al. (2025) for more details on PixelPop.

[3] Note, however, that the Default BBH model, Three Subpopulation model, $\chi_{\rm eff}$ Three Transitions and the copula analyses used Mixed samples for a small handful of events from O4b, namely GW241111_111552, GW241110_124123, GW240925_005809 and GW240910_103535

PixelPop variant	Dimensionality	Sections used
(m_1, m_2)-PixelPop	2	Secs. 4.1, 4.2, 4.4.1, 7
$(\chi, \cos\theta)$-PixelPop	2	Sec. 4.4.3
(m_1, q)-PixelPop	2	Secs. 4.4.2, 6, 7
$(m_1, \chi_{\rm eff})$-PixelPop	2	Secs. 5, 6
(m_1, z)-PixelPop	2	Sec. 6
$(\chi_{\rm eff}, \chi_{\rm p})$-PixelPop	2	App. E
$(\chi_{\rm eff}, q)$-PixelPop	2	Sec. 9.1
$(\chi_{\rm eff}, z)$-PixelPop	2	Sec. 9.2
z-PixelPop	1	Sec. 4.4.4

Table 3. Variants of PixelPop used in this paper

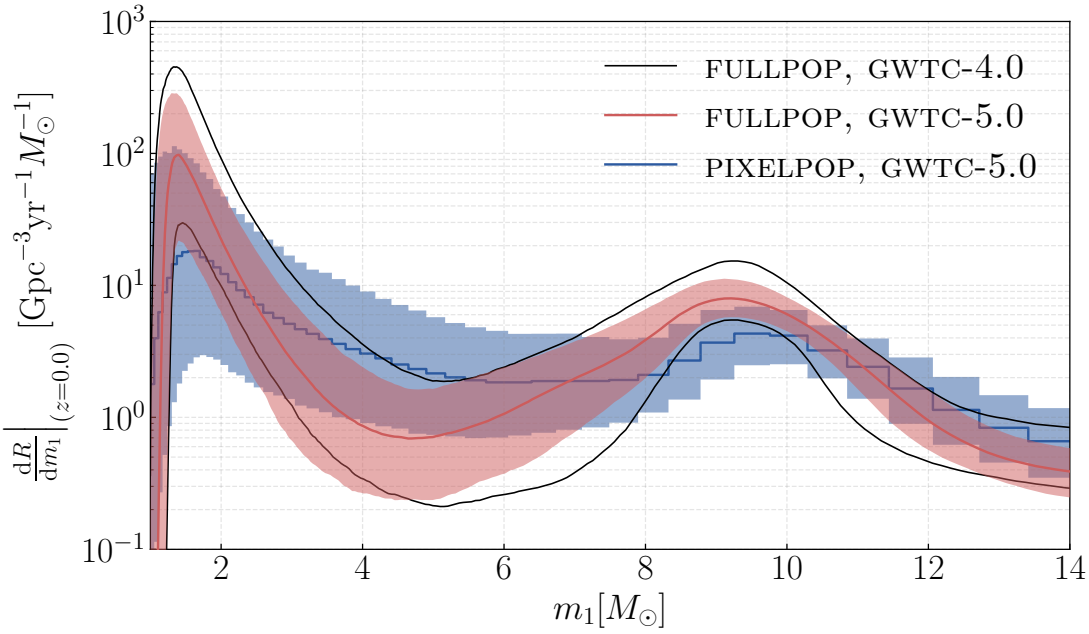

Figure 13. The primary mass distribution below 14 $M_\odot$. The solid lines show the median distribution for each model, with the shaded bands depicting the 90% credible regions. With GWTC-5.0, we find that our models effectively rule out a completely empty lower mass gap. The FullPop model parameterizes the depth of the gap with the hyperparameter A, with $A = 1$ indicating a completely empty gap between $3-5\,M_\odot$. With GWTC-5.0 we find $A \leq 0.88$ at 99% credibility.

B.2. FullPop

The strongly-parameterized FullPop (Abac et al. 2025a; Farah et al. 2022; Mali & Essick 2025), models the complete CBC distribution. The model parameterizes both the primary and secondary masses as drawn from a common underlying population, $\pi_m(m \mid \Lambda)$, with a pairing function, $f(m_1, m_2)$,

$$\pi(m_1, m_2 \mid \Lambda) \propto \pi_m(m_1 \mid \Lambda)\pi_m(m_2 \mid \Lambda) f(m_1, m_2)\,\Theta(m_2 < m_1), \tag{B2}$$

where Θ is the Heaviside function. The mass model, $\pi_m(m \mid \Lambda)$, is parameterized as

$$\begin{aligned}\pi_m(m \mid \Lambda) = \quad & [1 + c_1 \mathcal{N}_{[m_{\rm min}, m_{\rm max}]}(m \mid \mu_1, \sigma_1) + c_2 \mathcal{N}_{[m_{\rm min}, m_{\rm max}]}(m \mid \mu_2, \sigma_2)] n_1(m \mid m_{\rm NSmax}, m_{\rm BHmin}, \eta_{\rm NSmax}, \eta_{\rm BHmin}, A) \\ & \times n_2(m \mid m_{\rm UMGmin}, m_{\rm UMGmax}, \eta_{\rm UMGmin}, \eta_{\rm UMGmax}, A_2) h(m \mid m_{\rm NSmin}, \eta_{\rm NSmin}) l(m \mid m_{\rm BHmax}, \eta_{\rm BHmax}) \\ & \times \begin{cases} m^{\alpha_1} & \text{if } m < m_{\rm NSmax} \\ m^{\alpha_{\rm dip}} m_{\rm NSmax}^{\alpha_1 - \alpha_{\rm dip}} & \text{if } m_{\rm NSmax} \leq m < m_{\rm BHmin} \\ m^{\alpha_2} m_{\rm NSmax}^{\alpha_1 - \alpha_{\rm dip}} m_{\rm BHmin}^{\alpha_{\rm dip} - \alpha_2} & \text{if } m \geq m_{\rm BHmin}. \end{cases} \end{aligned} \tag{B3}$$

This $\pi_m(m \mid \Lambda)$ represents a universal mass function to describe the primary- and secondary-mass distributions. Note that the marginal mass distribution is different from the universal mass distribution due to the pairing formalism. $\mathcal{N}_{[a,b]}(\mu, \sigma)$ represents a truncated normal distribution over $[a, b]$ with location and width parameters μ and σ. The high-pass, low-pass and notch functions are defined as:

$$l(m \mid m_{\rm BHmax}, \eta_{\rm BHmax}) = \left[1 + \left(\frac{m}{m_{\rm BHmax}}\right)^{\eta_{\rm BHmax}}\right]^{-1}, \tag{B4}$$

$$h(m \mid m_{\rm NSmin}, \eta_{\rm NSmin}) = 1 - l(m \mid m_{\rm NSmin}, \eta_{\rm NSmin}), \tag{B5}$$

$$n_1(m \mid m_{\rm NSmax}, m_{\rm BHmin}, \eta_{\rm NSmax}, \eta_{\rm BHmin}, A) = 1 - A l(m \mid m_{\rm NSmax}, \eta_{\rm NSmax}) h(m \mid m_{\rm BHmin}, \eta_{\rm BHmin}), \tag{B6}$$

$$n_2(m \mid m_{\rm UMGmin}, m_{\rm UMGmax}, \eta_{\rm UMGmin}, \eta_{\rm UMGmax}, A_2) = 1 - A_2 l(m \mid m_{\rm UMGmin}, \eta_{\rm UMGmin}) h(m \mid m_{\rm UMGmax}, \eta_{\rm UMGmax}). \tag{B7}$$

The pairing function

$$f(m_1, m_2 \mid \beta_{\rm BH}, \beta_{\rm NS}) = \begin{cases} \left(\frac{m_2}{m_1}\right)^{\beta_1} & \text{if } m_2 < 5\,{\rm M}_\odot \\ \left(\frac{m_2}{m_1}\right)^{\beta_2} & \text{if } m_2 > 5\,{\rm M}_\odot \end{cases} \tag{B8}$$

controls how much merging binaries favor/disfavor equal masses. We allow for alternative pairing for binaries with low-mass secondaries (NSBHs or BBH with the secondary component in the lower-mass gap, e.g., GW190814, Abbott et al. 2020b). We show the priors and describe the parameters of the FullPop model in Tab. 4. The primary-mass distribution below $15\,{\rm M}_\odot$ is shown in Fig. 13.

B.3. Truncated Gaussian Mixture Model

In the Truncated Gaussian Mixture Model analysis, we write the joint component spin magnitude as a sum of two truncated bivariate Gaussian mixtures (Hussain et al. 2026).

$$p(\boldsymbol{\chi}) = \eta_a \mathcal{N}(\boldsymbol{\chi} \mid \boldsymbol{\mu}^a, \boldsymbol{\Sigma}^a) + \eta_b \mathcal{N}(\boldsymbol{\chi} \mid \boldsymbol{\mu}^b, \boldsymbol{\Sigma}^b), \tag{B9}$$

where $\boldsymbol{\chi} = (\chi_1, \chi_2)$, and $\boldsymbol{\mu}$ and $\boldsymbol{\Sigma}$ are the mean vectors and the covariance matrices of the two-dimensional distribution. The indices a and b refer to the dominant and the subdominant modes respectively. The fraction of mergers in each mode is parameterized by η_a and η_b, with $\eta_a + \eta_b = 1$.

Unlike the component spin models highlighted in Sec. 4.4.3, this model fits the two components independently allowing us to separately infer the spins of each components and any possible correlations. Moreover by using more than one mode, the model is able to find substructure in this joint distribution that is not clearly distinguishable in IID models.

B.4. Default BBH *Model*

This section presents details the default strongly-parameterized models used in this paper (see Tab. 1). These are fully consistent with the fiducial models used by the LVK in our analysis of GWTC-4.0 data in Abac et al. (2025a).

Broken Power Law + 2 Peaks: The fiducial BBH mass model is a mixture between a broken power law and two left-truncated Gaussian peaks, with low-mass tapering applied to the full distribution. The broken power law is given by

$$p_{\rm BP}(m_1 \mid \alpha_1, \alpha_2, m_{\rm break}, m_{1,\rm low}, m_{\rm high}) = \frac{1}{N} \begin{cases} \left(\frac{m_1}{m_{\rm break}}\right)^{-\alpha_1} & m_{1,\rm low} \leq m_1 < m_{\rm break} \\ \left(\frac{m_1}{m_{\rm break}}\right)^{-\alpha_2} & m_{\rm break} \leq m_1 < m_{\rm high}, \end{cases} \tag{B10}$$

Table 4. Summary of FullPop model parameters and priors.

Category	Parameter	Unit	Description	Prior
Pairing Function	β_1	–	Power-law index below 5 $M_\odot$	U(−2, 3)
	β_2	–	Power-law index above 5 $M_\odot$	U(−2, 7)
Broken Power-Law	α_1	–	Power-law index below $m_{\rm NS\ max}$	U(−10, 2)
	$\alpha_{\rm dip}$	–	Power-law index between $m_{\rm NS\ max}$ and $m_{\rm BH\ min}$	U(−3, m2)
	α_2	–	Power-law index above $m_{\rm BH\ min}$	U(−3, 2)
	$m_{\rm brk}$	$M_\odot$	Break point between α_1 and α_2	5
Highpass Filter	$m_{\rm NS\ min}$	$M_\odot$	Low-mass roll-off	U(1, 1.4)
	$\eta_{\rm min}$	–	Sharpness at $m_{\rm NS\ min}$	50
Lowpass Filter	$m_{\rm BHmax}$	$M_\odot$	High-mass roll-off	U(60, 200)
	$\eta_{\rm max}$	–	Sharpness at $m_{\rm BHmax}$	U(−4, 12)
Low-Mass Notch	$m_{\rm NS\ max}$	$M_\odot$	Lower notch edge	U(1.4, 5)
	$\eta_1^{\rm low}$	–	Sharpness at $m_{\rm NS\ max}$	50
	$m_{\rm BH\ min}$	$M_\odot$	Upper notch edge	U(5, 9)
	$\eta_1^{\rm high}$	–	Sharpness at $m_{\rm BH\ min}$	50
	A_1	–	Notch depth	0
High-Mass Notch	$m_{\rm UMGmin}$	$M_\odot$	Lower notch edge	U(30, 90)
	$\eta_2^{\rm low}$	–	Sharpness at $m_{\rm UMGmin}$	30
	$m_{\rm UMGmax}$	$M_\odot$	Upper notch edge	U(60, 150)
	$\eta_2^{\rm high}$	–	Sharpness at $m_{\rm UMGmax}$	30
	A_2	–	Depth of high-mass notch	U(0, 1)
Low-Mass Peak	$\mu_2^{\rm peak}$	$M_\odot$	Peak location	U(6, 12)
	$\sigma_2^{\rm peak}$	$M_\odot$	Peak width	U(0, 5)
	c_2	–	Peak height	U(0, 500)
High-Mass Peak	$\mu_1^{\rm peak}$	$M_\odot$	Peak location	U(17, 50)
	$\sigma_1^{\rm peak}$	$M_\odot$	Peak width	U(4, 20)
	c_1	–	Peak height	U(0, 1000)

Note—$U(a, b)$ denotes a uniform distribution in the range $[a, b]$.

where α_1 and α_2 are the power-law indices, the transition between the low-mass and high-mass power law occurs at $m_{\rm break}$, and the normalization constant is

$$N = m_{\rm break}\left[\frac{1-(m_{1,\rm low}/m_{\rm break})^{1-\alpha_1}}{1-\alpha_1} + \frac{\left(m_{1,\rm high}/m_{\rm break}\right)^{1-\alpha_2}-1}{1-\alpha_2}\right]. \tag{B11}$$

The full mixture distribution is

$$\begin{aligned}\pi(m_1) \propto \Big[&\lambda_0 p_{\rm BP}(m_1 \mid \alpha_1, \alpha_2, m_{\rm break}, m_{1,\rm low}, m_{\rm high}) + \lambda_1 \mathcal{N}_{lt}(m_1 \mid \mu_1, \sigma_1, \text{low} = m_{1,\rm low}) \\ &+ (1-\lambda_0-\lambda_1)\mathcal{N}_{lt}(m_1 \mid \mu_2, \sigma_2, \text{low} = m_{1,\rm low})\Big] S(m_1 \mid m_{1,\rm low}, \delta_{m,1}),\end{aligned} \tag{B12}$$

where $\mathcal{N}_{lt}$ is a left-truncated normal distribution. The Planck tapering function S ensures a smooth turn-on of the distribution in the range $(m_{1,\rm low}, m_{1,\rm low} + \delta_{m,1}]$ and is given by

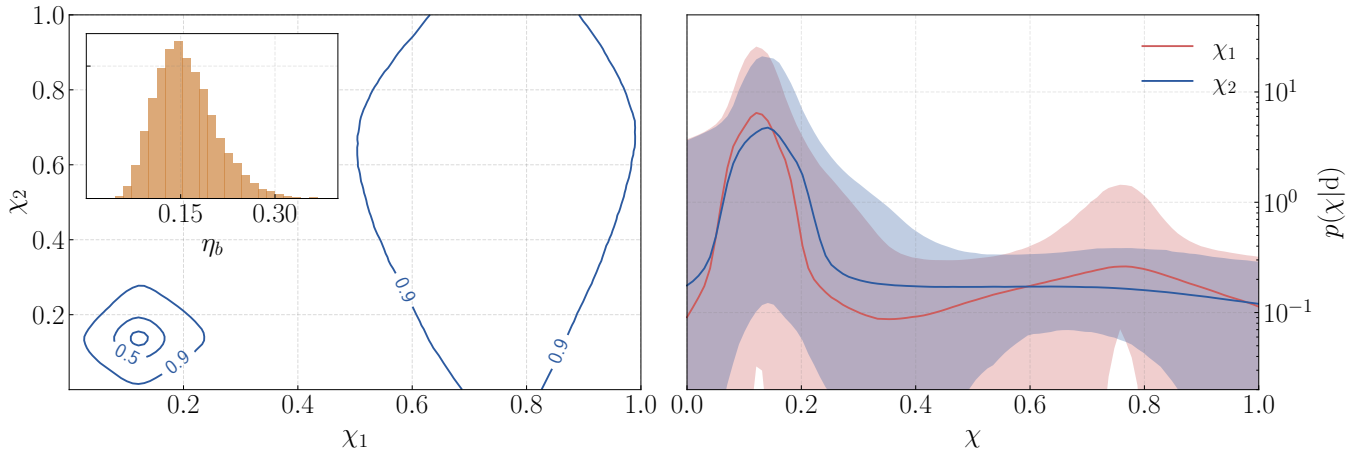

Figure 14. A plot of the 10%, 50% and 90% HDI contours for the median of the joint $\chi_1 - \chi_2$ distribution on the left, as inferred with Truncated Gaussian Mixture Model. We find a dominant mode centered away from zero spins but below spin magnitudes of 0.2 in both components. The subdominant mode is localized at $\chi_1 \sim 0.7$ but with a broad distribution for χ_2. The analysis finds that the fraction of BBH mergers in the subdominant mode, given by η_b, confidently excludes zero as shown in the inset. The marginal distributions of χ_1 and χ_2 are shown on the right. The dominant modes are again well recovered in both components. The subdominant mode is consistent with either a broad χ_2 distribution or a potential peak at $\chi_2 \sim 0.7$.

$$S(m \mid m_{\rm low}, \delta_m) = \begin{cases} 0 & m < m_{\rm low}, \\ [1 + f(m - m_{\rm low}, \delta_m)]^{-1} & m_{\rm low} \leq m < m_{\rm low} + \delta_m, \\ 1 & m_{\rm low} + \delta_m \leq m, \end{cases} \tag{B13}$$

with

$$f(m', \delta_m) = \exp\left(\frac{\delta_m}{m'} + \frac{\delta_m}{m' - \delta_m}\right). \tag{B14}$$

We model the mass ratio as a power law with index β_q and low-mass tapering applied to secondary mass m_2, conditioned on primary mass m_1,

Table 5 shows the parameter descriptions and prior ranges. Figure 15 shows the posterior distributions of the hyperparameters for two different variance cuts.

Default BBH component spin model: We model the spin magnitudes (χ_i) as a truncated Gaussian distribution between 0 and 1, assuming they are identically and independently distributed:

$$\pi(\chi_i \mid \mu_\chi, \sigma_\chi) = \mathcal{N}_{[0,1]}(\chi_1 \mid \mu_\chi, \sigma_\chi)\mathcal{N}_{[0,1]}(\chi_2 \mid \mu_\chi, \sigma_\chi)\,. \tag{B15}$$

We model the distribution of the cosine spin tilt angle ($\cos\theta_i$) as a mixture between a Gaussian distribution truncated on -1 to 1 and an isotropic distribution, assuming they are identically but *not* independently distributed:

$$\pi(\cos\theta_i \mid \mu_t, \sigma_t, \zeta) = \zeta\,\mathcal{N}_{[-1,1]}(\cos\theta_1 \mid \mu_t, \sigma_t)\mathcal{N}_{[-1,1]}(\cos\theta_2 \mid \mu_t, \sigma_t) + \frac{1-\zeta}{4}\,. \tag{B16}$$

We here allow for the location of the Gaussian subpopulation to vary, following Vitale et al. (2022). Priors on the hyperparameters are given in Tab. 6. Posteriors of the model parameters are shown in Fig. 16 with two different variance cuts.

Default BBH redshift model: We model redshift evolution by the comoving merger rate density. In particular, we use the model

$$\pi(z \mid \kappa) \propto \frac{1}{1+z}\frac{\mathrm{d}V_c}{\mathrm{d}z}(1+z)^\kappa \tag{B17}$$

where the prefactor converts from a rate density in comoving volume and source-frame time to detector-frame time and redshift. In other words, the comoving rate density scales as $\mathcal{R} \propto (1+z)^\kappa$. We use a prior on κ as specified in Tab. 7. The posterior inferences of the parameters are shown in Fig. 17.

Table 5. Summary of Broken Power Law + 2 Peaks model parameters and priors.

Parameter	Description	Prior
α_1	Power-law index of 1st primary-mass power law	U(−4, 12)
α_2	Power-law index of 2nd primary-mass power law	U(−4, 12)
$m_{\rm break}$	Power-law break location	U(20, 50)
μ_1	Location of the first peak	U(5, 20)
σ_1	Width of the first peak	U(0, 10)
μ_2	Location of the second peak	U(25, 60)
σ_2	Width of the second peak	U(0, 10)
$m_{1,\rm low}$	Lower edge of taper function	U(3, 10)
$\delta_{\rm m,1}$	Mass range of low mass tapering	U(0, 10)
λ_0, λ_1	Mixing fractions between power law and peaks	Dir(α = (1, 1, 1))
$m_{\rm high}$	Maximum mass for distribution, which is pinned to $m_{\rm high}$ = 300 $M_\odot$ by default	$\delta(m_{\rm high} - 300)$
β_q	Power-law index of mass-ratio power law	U(−2, 7)
$m_{2,\rm low}$	Lower edge of taper function in m_2	U(3, $m_{1,\rm low}$)
$\delta_{\rm m,2}$	Mass range of low-mass tapering in m_2	U(0, 10)

Table 6. Summary of Default BBH model parameters for spin magnitudes (Eq. B15) and tilt angles (Eq. B16).

Parameter	Description	Prior
μ_χ	Location of the χ distribution	U(0, 1)
σ_χ	Width of the χ distribution	U(0.005, 1)
μ_t	Location of the Gaussian component of the $\cos\theta$ distribution	U(−1, 1)
σ_t	Width of the Gaussian component of the $\cos\theta$ distribution	U(0.01, 4)
ζ	Fraction in the Gaussian component of the $\cos\theta$ distribution	U(0, 1)
$t_{\rm min}$	Minimum of the $\cos\theta$ distribution	U(−1, 1)

Table 7. Summary of Default BBH redshift model parameter (top) and priors and Madau-Dickinson model parameters (bottom), and the corresponding priors.

Parameter	Description	Prior
κ_z	Power-law index on comoving merger rate evolution	U(−10, 10)
γ	The low redshift index of the Madau-Dickinson model	U(−10, 10)
$z_{\rm peak}$	The peak redshift parameter of the Madau-Dickinson model	U(0, 2.5)
α	The high redshift index of the Madau-Dickinson model	U(−10, 10)

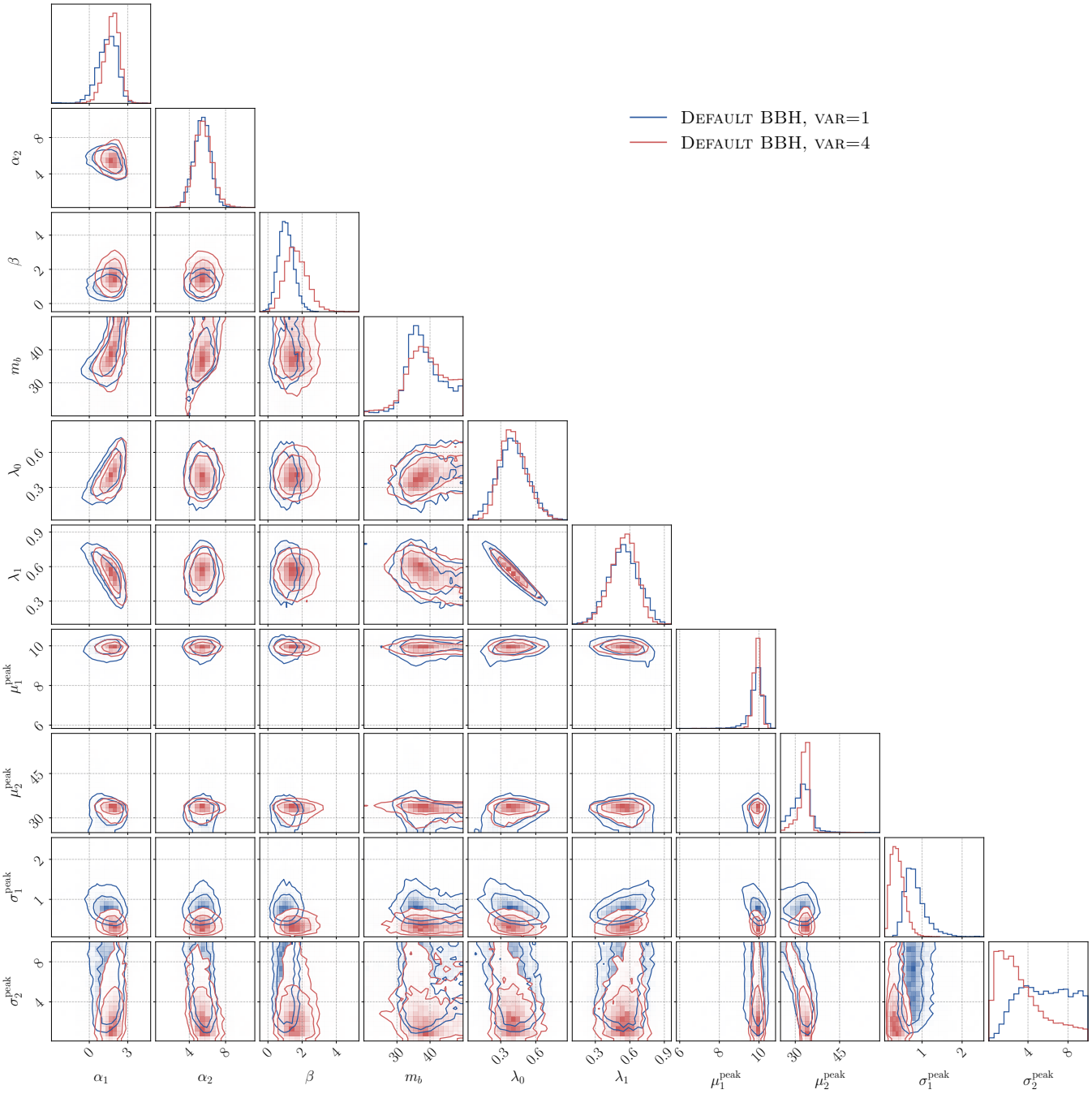

Figure 15. The posterior distribution of the parameters (see Tab. 5 for definition) of the DEFAULT BBH mass model. The two colors corresponds to inferences with two different variance cuts (see Sec. 3). Other than expected differences in the width of the Gaussian peaks, other parameter estimates are consistent between both runs.

B.5. *Madau–Dickinson Model*

We test an alternative redshift model based on the parametric form of the Madau–Dickinson Star Formation Rate.

$$\psi(z \mid \gamma, \alpha, z_p) \propto \frac{(1+z)^{\gamma}}{1 + ((1+z)/(1+z_p))^{\alpha}}. \tag{B18}$$

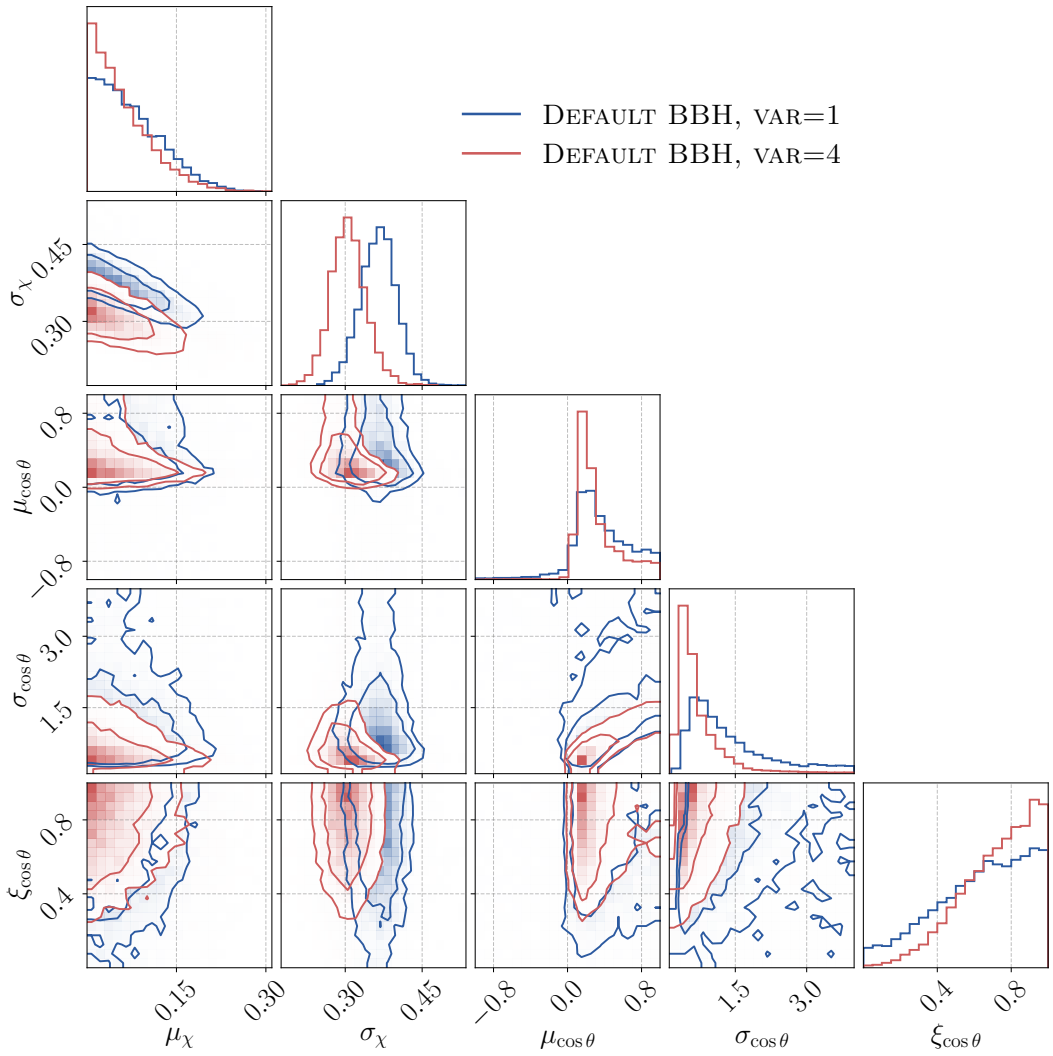

Figure 16. The posterior distribution of the parameters (see Tab. 6 for definition) of the Default BBH spin model. The two colors corresponds to inferences with two different variance cuts (see Sec. 3). Other than expected differences in the width of the Gaussians, other parameter estimates are consistent between both runs.

At $z \ll z_p$, the spectral index of the model is given by

$$\kappa_{\rm eff} = \gamma - \frac{\alpha}{1 + (1 + z_p)^\alpha} \tag{B19}$$

Model priors are shown in Tab. 7 and the inferred redshift distribution in Fig. 18. No major deviations are noticeable between the inferred redshift distribution of the Madau–Dickinson model and the Default BBH redshift model.

B.6. Bivariate Skewed $\chi_{\rm eff}/\chi_{\rm p}$

The Bivariate Skewed $\chi_{\rm eff}/\chi_{\rm p}$ uses a truncated version of the multivariate skewnormal model (Azzalini & Valle 1996). This model combines the bivariate Gaussian (Miller et al. 2020) and the skewnormal models (Banagiri et al. 2025b) used to fit effective spins in previous LVK analyses (Abac et al. 2025a; Abbott et al. 2023b). This model therefore allows both the $\chi_{\rm eff}$ and $\chi_{\rm p}$ distributions to be skewed and be covariant with each other.

The model is formally defined as,

$$p(\chi_{\rm eff}, \chi_{\rm p}) \propto \begin{cases} 2\mathcal{N}(\vec{\chi} \mid \vec{\mu}, \Sigma)\, \Phi(\vec{\chi} - \vec{\mu} \cdot \vec{\alpha}) & \text{if } \chi_{\rm eff} \in [-1, 1] \text{ and } \chi_{\rm p} \in [0, 1], \\ 0 & \text{otherwise} \end{cases}. \tag{B20}$$

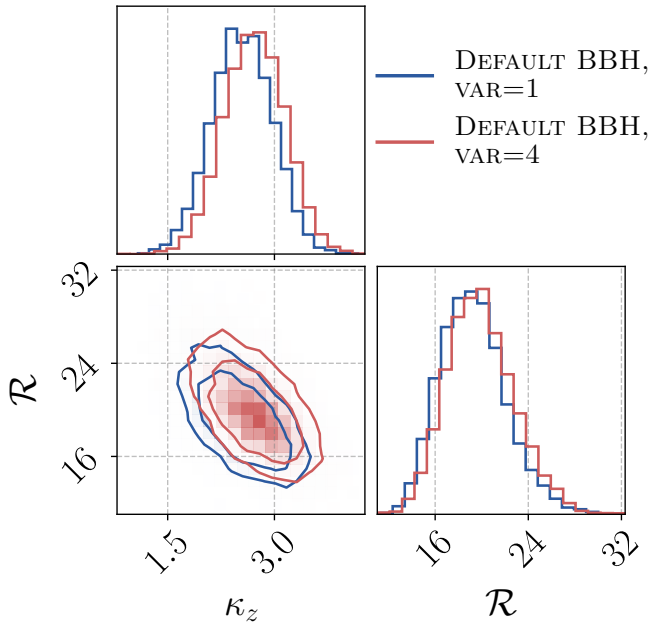

Figure 17. The posterior distribution of the parameters (see Tab. 7 for definition) of the DEFAULT BBH redshift model. The two colors corresponds to inferences performed using two different convergence cuts.

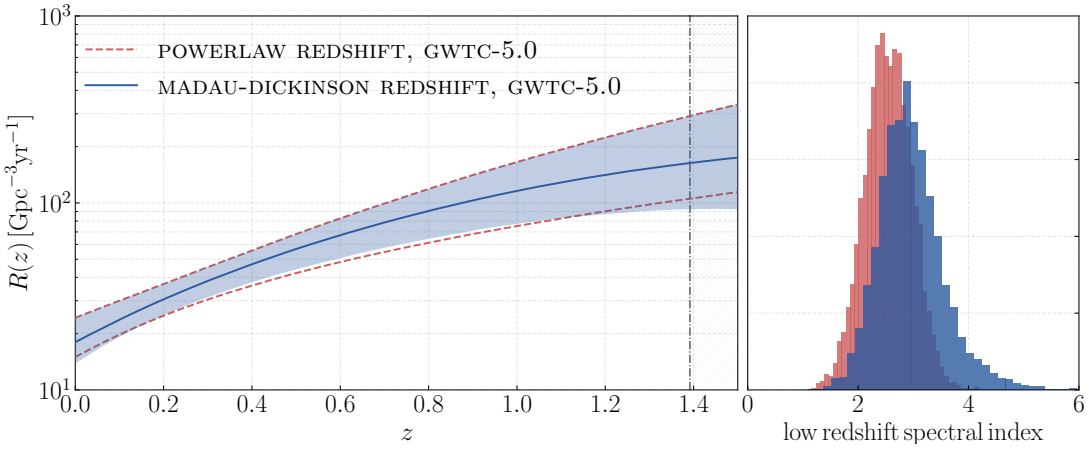

Figure 18. The redshift distribution of the BBH population under the Madau–Dickinson model (Eq. B18) is shown on the left (with the DEFAULT BBH redshift model shown in comparison). In the right, the inferred value of the low redshift spectral index κ_z assuming $p(z) \propto (1+z)^{\kappa_z}$, and for the Madau–Dickinson model (Eq. B19).

Here, $\vec{\chi} = (\chi_{\rm eff}, \chi_{\rm p})$ is the vector of effective spins. The parameters $\vec{\mu} = (\mu_{\rm eff}, \mu_{\rm p})$ represent the mean vector, and Σ, the covariance matrix with normalized covariance ρ:

$$\Sigma = \begin{bmatrix} \sigma_{\rm eff}^2 & \rho\sigma_{\rm eff}\sigma_{\rm p} \\ \rho\sigma_{\rm eff} & \sigma_{\rm p}^2 \end{bmatrix}, \tag{B21}$$

and $\vec{\alpha} = (\alpha_{\rm eff}, \alpha_{\rm p})$ as the skewness matrix. While $\alpha_{\rm eff}$ and $\alpha_{\rm p}$ formally can take any real numbered value, for consistency with Abac et al. (2025a) and Banagiri et al. (2025b), we define $\epsilon_{\rm eff}$ and $\epsilon_{\rm p}$ such that,

$$\alpha_{\rm eff(p)} = \epsilon_{\rm eff(p)} + \tan\frac{\pi\epsilon_{\rm eff(p)}}{2}. \tag{B22}$$

Table 8. Summary of Bivariate Skewed $\chi_{\rm eff}/\chi_{\rm p}$ model parameters

Parameter	Description	Prior
$\mu_{\rm eff}$	Location of the $\chi_{\rm eff}$ distribution	U(−1, 1)
$\sigma_{\rm eff}$	Width of the $\chi_{\rm eff}$ distribution	U(0.05, 1)
μ_p	Location of the $\chi_{\rm p}$ distribution	U(0.05, 1)
σ_p	Width of the $\chi_{\rm p}$ distribution	U(0.07, 1)
ρ	Degree of correlation between $\chi_{\rm eff}$ and $\chi_{\rm p}$	U(−0.75, 0.75)
$\epsilon_{\rm eff}$	$\chi_{\rm eff}$ component of the skew of the distribution	U(−1, 1)
$\epsilon_{\rm p}$	$\chi_{\rm p}$ component of the skew of the distribution	U(−1, 1)

Table 8 shows the parameter priors and Fig. 19 shows the posteriors on the model parameters. We find that the Bivariate Skewed $\chi_{\rm eff}/\chi_{\rm p}$ model and the $(\chi_{\rm eff}, \chi_p)$-PixelPop model disagree on the degree of skewness of the $\chi_{\rm eff}$ distribution. Using the asymmetry about the mode of the distribution as a measure of skewness, we find that the former model infers skewness to be $0.38^{+0.3}_{-0.25}$, while the latter infers a value of $0.02^{+0.26}_{-0.27}$ – consistent with zero.

C. MASS RATIO AND SPIN CORRELATION VARIANTS

We verify the correlation between mass ratio and effective spin (Sec. 9.1) with variations of the Linear Correlation model and the weakly-parametrized PixelPop model. Namely, we test the Linear Correlation $(q,\chi_{\rm eff})$ model with a broken power-law distribution in q instead of a power-law distribution (Linear BPL), and a skewnormal distribution in $\chi_{\rm eff}$ instead of a truncated Gaussian (Linear Skew). The joint $(q,\chi_{\rm eff})$ distribution and the width of $\chi_{\rm eff}$ with q for all model variants are shown in Fig. 20. We find that the variants agree with the default model result: the position of the peak of the $\chi_{\rm eff}$ distribution does not evolve with q, and that the width of the $\chi_{\rm eff}$ distribution gets wider towards more unequal q. In addition, we test the impact of unequal-mass, high-spin, sources, such as GW241011 and GW241110, with a leave-one-out analysis using the default Linear Correlation model, finding that these observations do not impact the result. This confirms that the evolution of the width of $\chi_{\rm eff}$ with q is a robust feature of the data, and is not driven by particular choices of marginal distributions nor by individual events GW241011 and GW241110.

The more flexible PixelPop is also in agreement with the lack of evolution of the mean of $\chi_{\rm eff}$, with $\delta\mu_{\chi_{\rm eff}|q=0.7} = 0.17^{+0.59}_{-0.55}$. PixelPop finds the Spearman correlation statistic is negative at 26% credibility over the entire space (27% credibility over the data-dominated region $[q > 0.5, -0.25 < \chi_{\rm eff} < 0.25]$) indicating little evidence for an anti-correlation (Spearman 1904). PixelPop also identifies broadening, though this is less prominent than the strongly-parametrized models. We find $\delta\ln\sigma_{\chi_{\rm eff}|q=0.7} = -2.05^{+2.49}_{-2.40}$ at $q = 0.7$, which is approximately where the gradients are the largest and uncertainties on the mean and width are smallest. It is not clear whether this evolution is a transition between distinct features along the mass-ratio spectrum with different widths of the $\chi_{\rm eff}$ distribution, or a gradual transition along q as is assumed by the Linear Correlation model.

There may be several explanations for why the evolution of $\sigma_\chi(q)$ disagrees between the Linear Correlation and PixelPop models. The standard deviation has a mathematical limit, approximately equal to the standard deviation of a truncated uniform distribution over $(-1, 1)$. The result for PixelPop reaches this limit at $q < 0.3$, hence we caution against over interpreting σ_χ in this region. We calculate all other results plotted in Fig. 20 consistently with the PixelPop result, hence these also reach this limit at low q. This limit is not fundamental to the population models.Towards more equal mass ratios ($q \gtrsim 0.7$), PixelPop finds a broader distribution of $\chi_{\rm eff}$ than the Linear Correlation and Spline Correlation models. PixelPop a priori disfavours narrow distributions, as highlighted by the model's prior on the width of $\chi_{\rm eff}$ (grey interval in the right panel of Fig. 20). We find that this is due to a combination of PixelPop's ICAR prior preference for smoother distributions, and that measuring the width of a narrow distribution requires strong constraints in the tails. While stronger approaches such as the Linear Correlation and Spline Correlation models extrapolate in the tails using their more rigid functional form, weaker models like PixelPop constrain data-poor regions using a combination of the prior (favoring smoothness) and the information due to non-detection (upper bounds). The inflated uncertainty away from the bulk leads to a bias towards large standard deviations. Compared to the prior, the data at $q \gtrsim 0.6$ are highly informative towards a narrower $\chi_{\rm eff}$ distribution, indicating a true preference for a narrower $\chi_{\rm eff}$ distribution at more equal mass ratios. The disagreement between the Linear Correlation and PixelPop models for $q > 0.7$ could also come from the Linear Correlation model's assumption that the evolution of the width of $\chi_{\rm eff}$ is the same at all q. Instead, it may be that the width of the $\chi_{\rm eff}$ distribution is narrowest at $q < 1$, which is not allowed within the modelling assumptions of the Linear Correlation model which requires monotonic evolution of the width of $\chi_{\rm eff}$.

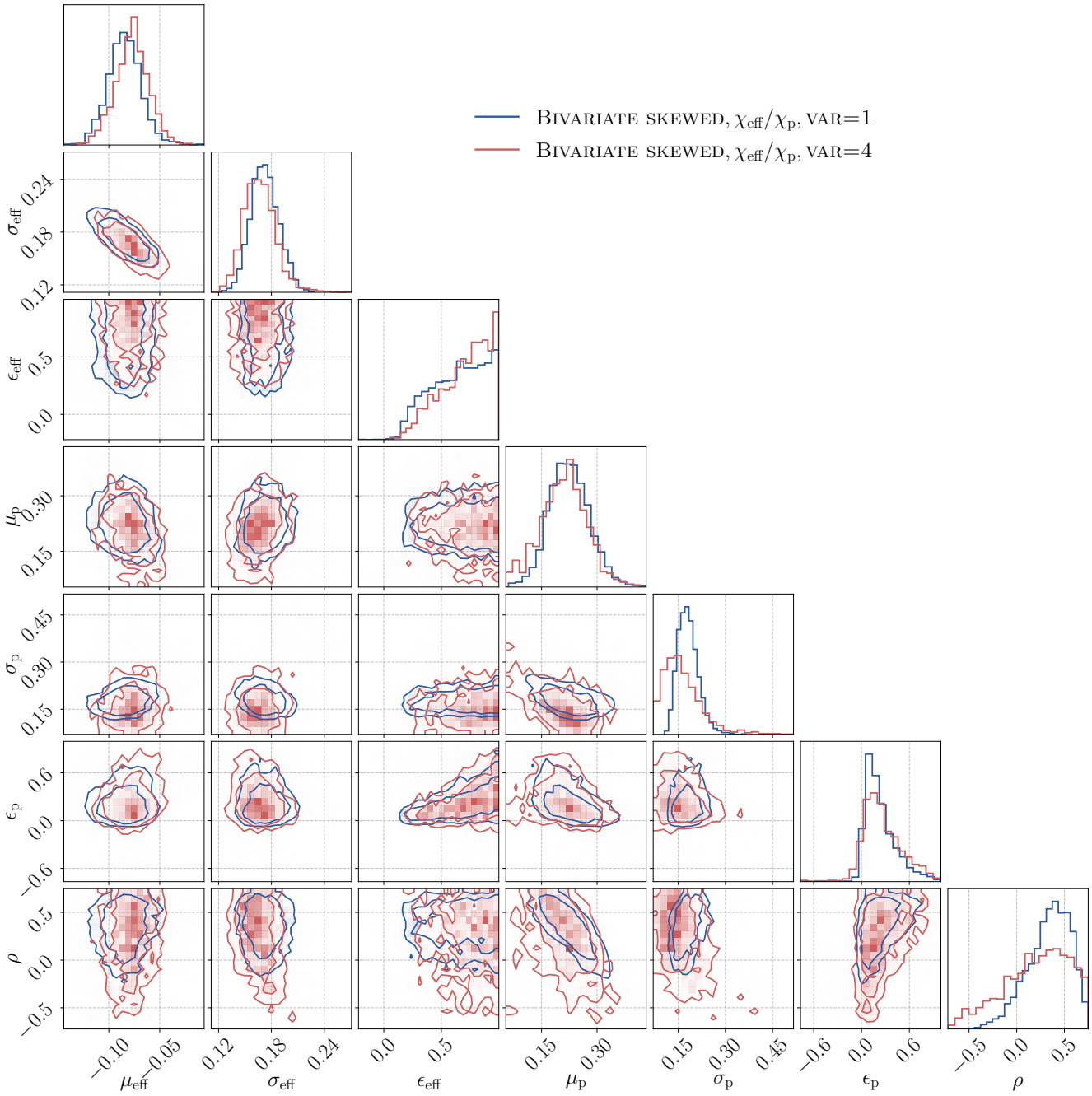

Figure 19. The posterior distribution of the parameters for the Bivariate Skewed $\chi_{\rm eff}/\chi_{\rm p}$ model. The two colors corresponds to inferences with two different variance cuts (see Sec. 3). We find that the run with higher variance cut infers a $\mu_{\rm p}$ value that is slightly lower but still statistically consistent with the default run with a variance cut of 1. We see that Bivariate Skewed $\chi_{\rm eff}/\chi_{\rm p}$ prefers a positive skewness ($\epsilon_{\rm eff} > 0$ at 99.9 credibility) while for $\chi_{\rm p}$, the model prefers small skew. The correlation coefficient between $\chi_{\rm eff}$ and $\chi_{\rm p}$ is consistent with zero.

D. REDSHIFT AND SPIN CORRELATION VARIANTS

Figure D shows the joint $(\chi_{\rm eff}, z)$ distribution and the width of $\chi_{\rm eff}$ with z for two model variants: the $(z,\chi_{\rm eff})$-PixelPop model, and a modified Linear Correlation model with a skewnormal marginal $\chi_{\rm eff}$ distribution (Linear Skew). The peak of the joint $(\chi_{\rm eff}, z)$ distribution differs between both models due to modeling assumptions; the Linear Correlation model assumes a power-law in redshift which is strictly monotonic. The marginal redshift evolution is consistent within uncertainties for both PixelPop and a power-law model as seen in Fig. 5.

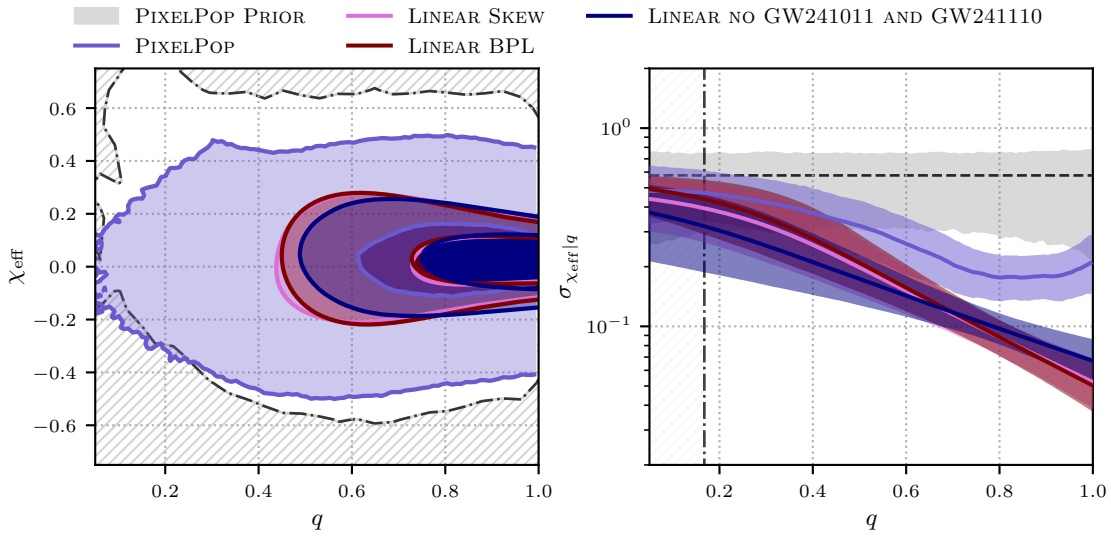

Figure 20. Left: the joint $(q,\chi_{\rm eff})$ PPD for the $(q,\chi_{\rm eff})$-PixelPop model, for the Linear BPL (pink) and Linear Skew (dark red) variants of the default Linear Correlation model, and for the default Linear Correlation model omitting highly-spinning, unequal-mass-ratio events GW241011 and GW241110 (dark blue). Right: the inferred standard deviation of the $\chi_{\rm eff}$ distribution as a function of mass ratio for the same models. The shaded bands show the 90% credible interval, where the grey band shows the 99% credible interval of the $(q,\chi_{\rm eff})$-PixelPop prior on $\sigma_{\chi_{\rm eff}}(q)$. At low q, the standard deviation reaches a maximum value at $\sim 1/\sqrt{3}$, equivalent to the standard deviation of a uniform distribution over $(-1,1)$, shown in the black dashed line. The standard deviation shows a preference for a narrowing $\chi_{\rm eff}$ with increasing q for all Linear Correlation model variants. The $(q,\chi_{\rm eff})$-PixelPop result also shows a preference for narrowing $\chi_{\rm eff}$ with increasing q, though to a lesser degree due to modeling assumptions.

We find that the Linear Skew model prefers a slightly steeper evolution of the width of $\chi_{\rm eff}$ with z than the default Linear Correlation model, though with larger uncertainties, with $\delta\ln\sigma_{\chi_{\rm eff}|z} = 0.53^{+0.51}_{-0.50}$. This is concurrent with an increasing skew of $\chi_{\rm eff}$ with larger redshifts.

PixelPop also indicates some degree of broadening of $\chi_{\rm eff}$ with z. Within $\chi_{\rm eff} \in [-0.5, 0.5]$, $z < 1$—where we have the most information from observations—we find that the Spearman correlation coefficient for the broadening of the distribution for PixelPop is positive at 94.8% credibility. This evidence for broadening can be seen from the increasing $\sigma_{\chi_{\rm eff}}(z)$ until $z \sim 1.25$. Outside this range, this evidence diminishes and the evidence is consistent with no broadening, but this is likely due to the larger uncertainties. PixelPop finds that the mean of the $\chi_{\rm eff}$ distribution is consistent with no correlation for all values of z. Over the restricted domain of $\chi_{\rm eff} \in [-0.5, 0.5]$, $z < 1$, the Spearman correlation coefficient is $-0.03^{+0.16}_{-0.16}$, indicating no correlation of the mean of $\chi_{\rm eff}$ with redshift, while outside this domain PixelPop is largely prior dominated due to a lack of observations.

With a Copula Correlation model, we find evidence for a positive correlation in $(\chi_{\rm eff}, z)$. We measure the Copula Correlation model's correlation parameter $\eta_{\chi_{\rm eff},z} = 3.25^{+1.35}_{-1.53}$, or $\eta_{\chi_{\rm eff},z} > 0$ with 99.8% credibility — up from 98% for GWTC-4.0. The correlation in the Copula Correlation model may be driven by the high-redshift region where we lack sensitivity, and hence the evidence for correlation could come from extrapolation.

Unlike PixelPop, Linear Correlation, and Spline Correlation models, the Copula Correlation model lacks flexibility to fit broadening. If the $\chi_{\rm eff}$ distribution only broadens with redshift and there is no evolution in the mean, it might be expected that the Copula Correlation model finds no evidence for correlation, with $\eta_{\chi_{\rm eff},z}$ consistent with zero. One caveat is that the orbital hang-up effect leads to BBHs with negative $\chi_{\rm eff}$ being quieter than those with positive $\chi_{\rm eff}$, all else held the same (Campanelli et al. 2006). This may cause the median of the PixelPop rate, as shown in Fig. 12, to be wider towards negative $\chi_{\rm eff}$ as the model is less able to rule out contributions from negative $\chi_{\rm eff}$ BBH. Under PixelPop modelling assumptions, this manifests as broadening, and could obscure an underlying correlation. On the other hand, the correlation in the Copula Correlation model may be driven by the high-redshift region where we lack sensitivity, and hence the evidence for correlation could come from extrapolation. To compare to the PixelPop result, over the restricted domain of $\chi_{\rm eff} \in [-0.5, 0.5]$, $z < 1$, the Spearman correlation coefficient for the Copula Correlation model is 0.10, marginalised over the hyperposterior. This is in agreement with no correlation where we are most informed by observations, indicating that the Copula Correlation model is likely extrapolating to high redshifts.

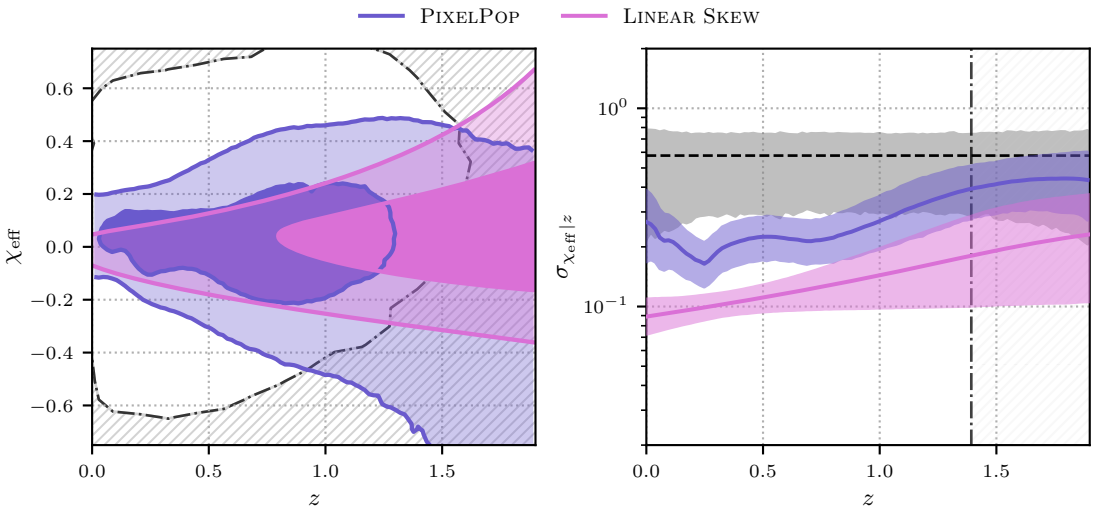

Figure 21. Left: the joint $(\chi_{\rm eff}, z)$ distribution with the PixelPop model (purple) and the Linear Skew model (pink). Right: the inferred standard deviation of the $\chi_{\rm eff}$ distribution as a function of redshift for the Linear Correlation model variant and the $(z,\chi_{\rm eff})$-PixelPop model. The shaded bands show the 90% credible interval, where the grey band shows the 99% credible interval of the $(z,\chi_{\rm eff})$-PixelPop prior on $\sigma_{\chi_{\rm eff}}(z)$. At large redshifts, the standard deviation of the PixelPop model reaches a maximum value at $\sim 1/\sqrt{3}$, equivalent to the standard deviation of a uniform distribution over $(-1, 1)$, shown in the black dashed line. The standard deviation shows a preference for a broadening of $\chi_{\rm eff}$ with increasing z for the Linear Correlation model variant. The $(q,\chi_{\rm eff})$-PixelPop result also shows a preference for broadening of $\chi_{\rm eff}$ with increasing z, though to a lesser degree due to do modeling assumptions.

Table 9. Priors for the Linear Correlation model for the joint $q-\chi_{\rm eff}$ distribution.

Parameter	Description	Prior
$\mu_{\chi_{\rm eff}\|q=0}$	Mean of $\chi_{\rm eff}$ distribution at $q=0$	$\mathrm{U}(-1,1)$
$\mu_{\chi_{\rm eff}\|q=1}$	Mean of $\chi_{\rm eff}$ distribution at $q=1$	$\mathrm{U}(-2,2)$
$\ln\sigma_{\chi_{\rm eff}\|q=0}$	Natural log standard deviation of $\chi_{\rm eff}$ distribution at $q=0$	$\mathrm{U}(-5,0)$
$\ln\sigma_{\chi_{\rm eff}\|q=1}$	Natural log standard deviation of $\chi_{\rm eff}$ distribution at $q=1$	$\mathrm{U}(-12,4)$

E. INCONCLUSIVE CORRELATION RESULTS

Both our GWTC-4.0 analyses (Abac et al. 2025a) and follow-up work (e.g., Gennari et al. 2025; Sadiq et al. 2025b; Lalleman et al. 2025) failed to find model-independent evidence for an evolution of the primary-mass function with redshift. In GWTC-5.0 too we do not find that the primary mass evolves linearly with redshift. We investigate this with a Copula Correlation model, which allows for a correlation between m_1 and z with a variable strength $\eta_{\mathrm{m_1,z}}$. We find this correlation parameter to be $\eta_{\mathrm{m_1,z}} = 0.46^{+1.84}_{-1.95}$, consistent with zero. PixelPop finds no strong evidence for evolution of the primary nor secondary mass distribution with redshift. However, particular features in the primary-mass spectrum may vary with redshift, as discussed in Sec. 6 of the main text.

We also explore the space of $\chi_{\rm eff}$ and $\chi_{\rm p}$ (e.g., Plunkett et al. 2026), but we do not find any evidence of correlations with any of the Copula Correlation, Bivariate Skewed $\chi_{\rm eff}/\chi_{\rm p}$, or PixelPop models.

F. CORRELATION MODELS

All strongly-parametrized correlation model parameters and priors are specified in tables below.

Table 10. Priors for the Linear Correlation model for the joint $z - \chi_{\rm eff}$ distribution. Note that the prior on the width of the peaks in m_1 differs from the Broken Power Law + 2 Peaks model priors to reduce Monte Carlo uncertainties.

Parameter	Description	Prior
σ_1	Width of the first peak in m_1	U(0.25, 10)
σ_2	Width of the second peak in m_1	U(1, 10)
$\mu_{\chi_{\rm eff}\|z=0}$	Mean of $\chi_{\rm eff}$ distribution at $z = 0$	U(−1, 1)
$\mu_{\chi_{\rm eff}\|z=0.5}$	Mean of $\chi_{\rm eff}$ distribution at $z = 0.5$	U(−1, 1)
$\ln \sigma_{\chi_{\rm eff}\|z=0}$	Natural log standard deviation of $\chi_{\rm eff}$ distribution at $z = 0$	U(−5, 0)
$\ln \sigma_{\chi_{\rm eff}\|z=0.5}$	Natural log standard deviation of $\chi_{\rm eff}$ distribution at $z = 0.5$	U(−3, 5)

Table 11. Priors for the Spline Correlation model for the joint $q - \chi_{\rm eff}$ and joint $z - \chi_{\rm eff}$ distributions.

Parameter	Description	Prior
$\mu_{\chi_{\rm eff}}$	Mean of $\chi_{\rm eff}$ distribution at Spline Correlation model knots	U(−1, 1)
$\ln \sigma_{\chi_{\rm eff}}$	Natural log standard deviation of $\chi_{\rm eff}$ distribution at Spline Correlation model knots	U(−5, 0)

Table 12. Priors for the Linear Correlation Skewnormal and Linear Correlation Broken Power Law models for the joint $q - \chi_{\rm eff}$ distribution.

Parameter	Description	Prior
$\mu_{\chi_{\rm eff}\|q=0}$	Mean of $\chi_{\rm eff}$ distribution at $q = 0$	U(−1, 1)
$\mu_{\chi_{\rm eff}\|q=1}$	Mean of $\chi_{\rm eff}$ distribution at $q = 1$	U(−1, 1)
$\log_{10} \sigma_{\chi_{\rm eff}\|q=0}$	$\log_{10}$ standard deviation of $\chi_{\rm eff}$ distribution at $q = 0$	U(−1.5, 0.3)
$\log_{10} \sigma_{\chi_{\rm eff}\|q=1}$	$\log_{10}$ standard deviation of $\chi_{\rm eff}$ distribution at $q = 1$	U(−1.5, 0.3)
$\epsilon_{\chi_{\rm eff}\|q=0}$	Skew of $\chi_{\rm eff}$ distribution at $q = 0$ for the Skewnormal model	U(−1, 1)
$\epsilon_{\chi_{\rm eff}\|q=1}$	Skew of $\chi_{\rm eff}$ distribution at $q = 1$ for the Skewnormal model	U(−1, 1)
β_1	Power law index of the mass ratio distribution when $q < q_b$ for the Broken Power Law model	U(−2, 7)
β_2	Power law index of the mass ratio distribution when $q > q_b$ for the Broken Power Law model	U(−2, 7)
q_b	Mass ratio at which the power-law index changes from β_1 to β_2 for the Broken Power Law model	U(0, 1)

G. MODELS FOR RAPIDLY-SPINNING SUBPOPULATIONS

In Sec. 8, we model the mass dependence of the $\chi_{\rm eff}$ distribution using both weakly- and strongly-parametrized descriptions. Here, we give more details on the models.

G.1. $\chi_{\rm eff}$ Mixture

$\chi_{\rm eff}$ Mixture is a weakly-parametrized model in which the $\chi_{\rm eff}$ distribution at fixed m_1 is described as a mixture of a truncated Gaussian and a uniform component (Antonini et al. 2025; Antonini et al. 2025),

$$\pi(\chi_{\rm eff} \mid m_1, \Lambda) = \zeta(m_1)\,\mathcal{U}(\chi_{\rm eff} \mid \chi_{\rm min}, \chi_{\rm max}) + (1 - \zeta(m_1))\,\mathcal{N}_{\rm trunc}(\chi_{\rm eff} \mid \mu, \sigma). \tag{G23}$$

Table 13. Priors for the LINEAR CORRELATION SKEWNORMAL model for the joint $z-\chi_{\rm eff}$ distribution.

Parameter	Description	Prior
$\mu_{\chi_{\rm eff}\|z=0}$	Mean of $\chi_{\rm eff}$ distribution at $z=0$	$\mathrm{U}(-1,1)$
$\mu_{\chi_{\rm eff}\|z=1.9}$	Mean of $\chi_{\rm eff}$ distribution at $z=1.9$	$\mathrm{U}(-1,1)$
$\log_{10}\sigma_{\chi_{\rm eff}\|z=0}$	$\log_{10}$ standard deviation of $\chi_{\rm eff}$ distribution at $z=0$	$\mathrm{U}(-1.5,0.3)$
$\log_{10}\sigma_{\chi_{\rm eff}\|z=1.9}$	$\log_{10}$ standard deviation of $\chi_{\rm eff}$ distribution at $z=1.9$	$\mathrm{U}(-1.5,0.3)$
$\epsilon_{\chi_{\rm eff}\|z=0}$	Skew of $\chi_{\rm eff}$ distribution at $z=0$ for the SKEWNORMAL model	$\mathrm{U}(-1,1)$
$\epsilon_{\chi_{\rm eff}\|z=1.9}$	Skew of $\chi_{\rm eff}$ distribution at $z=1.9$ for the SKEWNORMAL model	$\mathrm{U}(-1,1)$

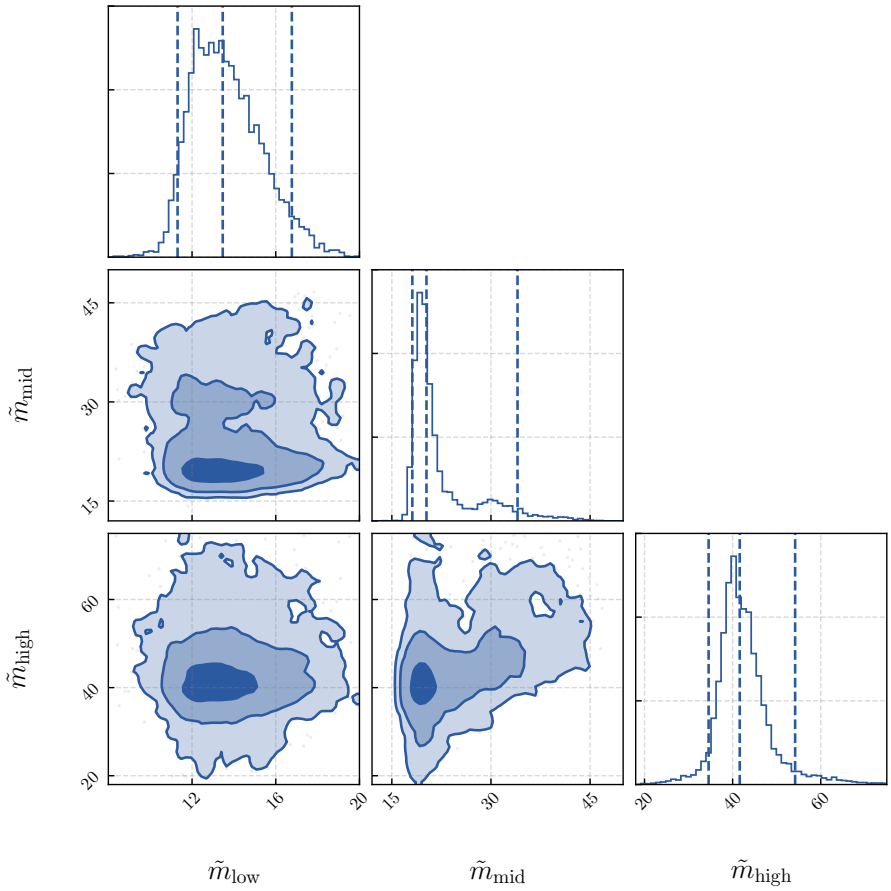

Figure 22. Posterior distributions of the transition masses $\tilde{m}_{\rm low}$, $\tilde{m}_{\rm mid}$, and $\tilde{m}_{\rm high}$ inferred with the three-transition model. One-dimensional marginals are shown on the diagonal, with dashed lines marking the median and 90% credible interval; two-dimensional credible regions are shown off-diagonal.

Here, μ and σ describe the Gaussian component, while $\chi_{\rm min}$ and $\chi_{\rm max}$ define the support of the uniform component. The mass dependence is encoded in the mixture fraction $\zeta(m_1)$, which is modeled non-parametrically as

$$\zeta(m_1) = S(\Psi(\ln m_1)), \tag{G24}$$

Table 14. Summary of $\chi_{\rm eff}$ Mixture model parameters and priors (top) and the Gaussian process hyperparameters (bottom).

Parameter	Description	Prior
μ	Location of the Gaussian component	U(−1, 1)
$\log\sigma$	Scale of the Gaussian component	U(−1.5, 0)
$\chi_{\rm max}$	Upper bound of the uniform component	U(0.1, 1)
$\chi_{\rm min,unscaled}$	Unscaled lower bound of the uniform component	U(0, 1)
a_ζ	Gaussian process amplitude parameter	$\mathcal{HN}(5)$
ℓ_ζ	Gaussian process correlation length parameter	$\mathcal{N}(-0.5, 1)$

Note—The true lower bound, $\chi_{\rm min}$ is obtained by the transformation $\chi_{\rm min} = \chi_{\rm min,unscaled}(1+\chi_{\rm max}) - 1$. $\mathcal{HN}(a)$ denotes a half-normal distribution with scale parameter a.

where $S(x) = (1+e^{-x})^{-1}$ ensures $0 \le \zeta(m_1) \le 1$. The latent function Ψ is drawn from a Gaussian process,

$$\Psi(\ln m_1) \sim \mathcal{GP}(0, k(x, x'; a_\zeta, \ell_\zeta)), \tag{G25}$$

with squared-exponential kernel k. The hyperparameters a_ζ and ℓ_ζ control the amplitude and correlation length of the process, respectively. The Gaussian process is evaluated on a grid uniform in $\ln m_1$, and $\zeta(m_1)$ is obtained via interpolation between grid points. This model allows the relative contribution of the broad spin component to vary smoothly with primary mass. The list of model parameters and their priors are shown in Tab. 14.

G.2. $\chi_{\rm eff}$ Three Transitions

As a more structured alternative, we consider a strongly-parametrized model in which the $\chi_{\rm eff}$ distribution is specified across four primary-mass intervals separated by three transition masses, $\tilde{m}_{\rm low}$, $\tilde{m}_{\rm mid}$, and $\tilde{m}_{\rm high}$ (Tong et al. 2025a). In all mass intervals, the baseline component is a truncated Gaussian ($\mathcal{N}_{\rm trunc}(\chi_{\rm eff} \mid \mu, \sigma)$) with shared hyperparameters μ and σ. In the intervals $\tilde{m}_{\rm low} < m_1 < \tilde{m}_{\rm mid}$ and $m_1 > \tilde{m}_{\rm high}$, this Gaussian component is mixed with a uniform component. The support of the uniform distribution is allowed to differ between the two mass ranges, and the corresponding mixture fractions are described by $\xi_{\text{low-mass}}$ and $\xi_{\text{high-mass}}$. The full model is

$$\pi(\chi_{\rm eff} \mid m_1, \Lambda) = \begin{cases} \mathcal{N}_{\rm trunc}(\chi_{\rm eff} \mid \mu, \sigma), & m_1 < \tilde{m}_{\rm low}, \\ \xi_{\text{low-mass}}\, \mathcal{U}(\chi_{\rm eff} \mid \chi_{\rm min}^{\text{low-mass}}, \chi_{\rm max}^{\text{low-mass}}) + (1-\xi_{\text{low-mass}})\, \mathcal{N}_{\rm trunc}(\chi_{\rm eff} \mid \mu, \sigma), & \tilde{m}_{\rm low} < m_1 < \tilde{m}_{\rm mid}, \\ \mathcal{N}_{\rm trunc}(\chi_{\rm eff} \mid \mu, \sigma), & \tilde{m}_{\rm mid} < m_1 < \tilde{m}_{\rm high}, \\ \xi_{\text{high-mass}}\, \mathcal{U}(\chi_{\rm eff} \mid \chi_{\rm min}^{\text{high-mass}}, \chi_{\rm max}^{\text{high-mass}}) + (1-\xi_{\text{high-mass}})\, \mathcal{N}_{\rm trunc}(\chi_{\rm eff} \mid \mu, \sigma), & m_1 > \tilde{m}_{\rm high}. \end{cases} \tag{G26}$$

This parameterization introduces discrete transition masses and allows the broad spin component to appear in two distinct mass ranges. The priors for the parameters of the $\chi_{\rm eff}$ Three Transitions model are summarized in Tab. 15.

H. CUMULATIVE DISTRIBUTION OF PRIMARY AND SECONDARY MASSES

In Fig. 23, we show the cumulative distribution functions of the m_1 and m_2 distributions inferred using the (m_1, m_2)-PixelPop model, with a focus on the high-mass range. The plot reveals that only a small fraction of mergers have $m_2 \gtrsim 40\,{\rm M}_\odot$, whereas a non-negligible fraction of BBHs have $m_1 \in [50\text{–}100]\,{\rm M}_\odot$. In particular, we find that 99.9% of BBHs have $m_2 \lesssim 57.9^{+38.7}_{-10.2}\,{\rm M}_\odot$. Although the uncertainty is relatively large due to the highly flexible assumptions of the PixelPop model, this finding is consistent with the GWTC-4.0 results (Tong et al. 2025b).

I. THREE-SUBPOPULATION MODEL

We also explore a model that allows for three subpopulations at different m_1 ranges, as proposed in Banagiri et al. (2025b). The three subpopulations differ in either their mass-ratio distributions, their spin-magnitude distributions or both. We refer to this

Table 15. Priors for the $\chi_{\rm eff}$ THREE TRANSITIONS model.

Parameter	Description	Prior
μ	Mean of the Gaussian component	U(-1,1)
$\log_{10}\sigma$	Logarithm base 10 of the standard deviation of the Gaussian component	U(−2, 1)
$\tilde{m}_{\rm low}$	the transition mass of the low-mass spinning subpopulation	U(5, 30)
$\tilde{m}_{\rm mid}$	the interval of the mass of the low-mass spinning subpopulation	U($\tilde{m}_{\rm low}$, $\tilde{m}_{\rm low}$ +30)
$\tilde{m}_{\rm high}$	the interval of the mass of the low-mass spinning subpopulation	U($\tilde{m}_{\rm mid}$, $\tilde{m}_{\rm mid}$ +80)
$\xi_{\text{low-mass}}$	Mixture fraction of the low-mass spinning subpopulation	U(0, 1)
$\xi_{\text{high-mass}}$	Mixture fraction of the high-mass spinning subpopulation	U(0, 1)
$\chi_{\rm min}^{\text{low-mass}}$	Minimum $\chi_{\rm eff}$ of the low-mass spinning subpopulation	U(−1, 1)
$\chi_{\rm max}^{\text{low-mass}}$	Maximum $\chi_{\rm eff}$ of the low-mass spinning subpopulation	U(−1, 1)
$\chi_{\rm min}^{\text{high-mass}}$	Minimum $\chi_{\rm eff}$ of the high-mass spinning subpopulation	U(−1, 1)
$\chi_{\rm max}^{\text{high-mass}}$	Maximum $\chi_{\rm eff}$ of the high-mass spinning subpopulation	U(−1, 1)

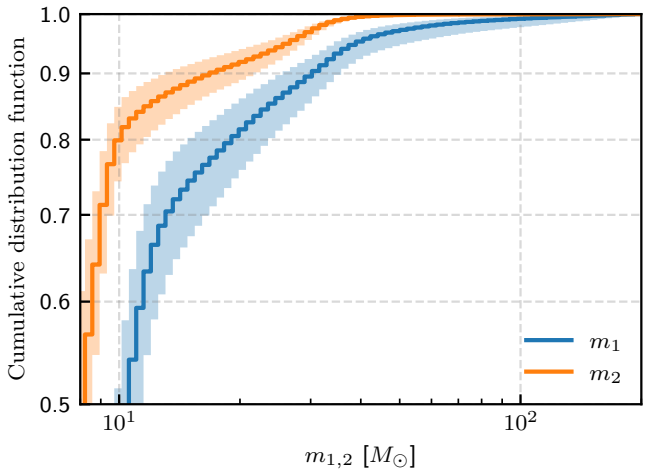

Figure 23. The cumulative distribution function of m_1 distribution and m_2 distribution using the (m_1, m_2)-PIXELPOP model, focusing on the high-mass range.

model as THREE-SUBPOPULATION model. The mass-ratio distribution of THREE-SUBPOPULATION model is modeled as:

$$p(q) \propto \begin{cases} q^{\beta_0}, & \text{if } m_1 \leq m^t_{\mathcal{AB}}, \\ q^{\beta_1}, & \text{if } m^t_{\mathcal{AB}} \leq m_1 \leq m^t_{\mathcal{BC}}, \\ \mathcal{N}(q \mid \mu_q, \sigma_q), & \text{if } m_1 > m^t_{\mathcal{BC}}, \end{cases} \tag{I27}$$

and the spin-magnitude distribution as:

$$p(\chi) \propto \begin{cases} \mathcal{N}(\chi \mid \mu_{\chi_0}, \sigma_{\chi_0}), & \text{if } m_1 \leq m^t_{\mathcal{BC}}, \\ \mathcal{N}(\chi \mid \mu_{\chi_1}, \sigma_{\chi_1}), & \text{if } m_1 > m^t_{\mathcal{BC}}. \end{cases} \tag{I28}$$

The priors for the parameters of the THREE-SUBPOPULATION model are summarized in Tab. 16. We employ the same spin tilt and redshift distributions as the basic mass model for all three subpopulations.

Consistent with GWTC-4.0 results in Banagiri et al. (2025b), we find that the high-mass subpopulation has significantly flatter mass-ratio distribution (Fig. 9).

Table 16. Priors for the THREE-SUBPOPULATION model.

Parameter	Description	Prior
$m^t_{\mathcal{ZA}}$	First potential transition mass	U(5, 20) $M_\odot$
$m^t_{\mathcal{AB}}$	Second potential transition mass	U(20, 65) $M_\odot$
$m^t_{\mathcal{BC}}$	Third potential transition mass	U(30, 75) $M_\odot$
β^i_q	Mass-ratio power-law index of the i-th subpopulation	U(−6, 11)
μ_q	Mean of the mass ratio distribution of the subpopulation	U(0.01, 1)
σ_q	Width of the mass ratio distribution of the subpopulation	U(0.01, 1)
μ^i_χ	Mean of the spin-magnitude distribution of the i-th subpopulation	U(0, 1)
σ^i_χ	Width of the spin-magnitude distribution of the i-th subpopulation	U(0.005, 2)
σ_1	Width of the first peak	U(0, 5)
κ_z	Power-law index on comoving merger rate evolution	U(−8, 8)
$m_{\rm high}$	Maximum mass for distribution, which is pinned to $m_{\rm high} = 200\,{\rm M}_\odot$ for this model	$\delta(m_{\rm high} - 200)$

J. PRIMARY AND SECONDARY MASS MARGINALS: PIXELPOP AND BINNED GAUSSIAN PROCESS COMPARISON

In this appendix, we compare the primary- and secondary-mass marginals inferred using the (m_1, m_2) variant of PIXELPOP and

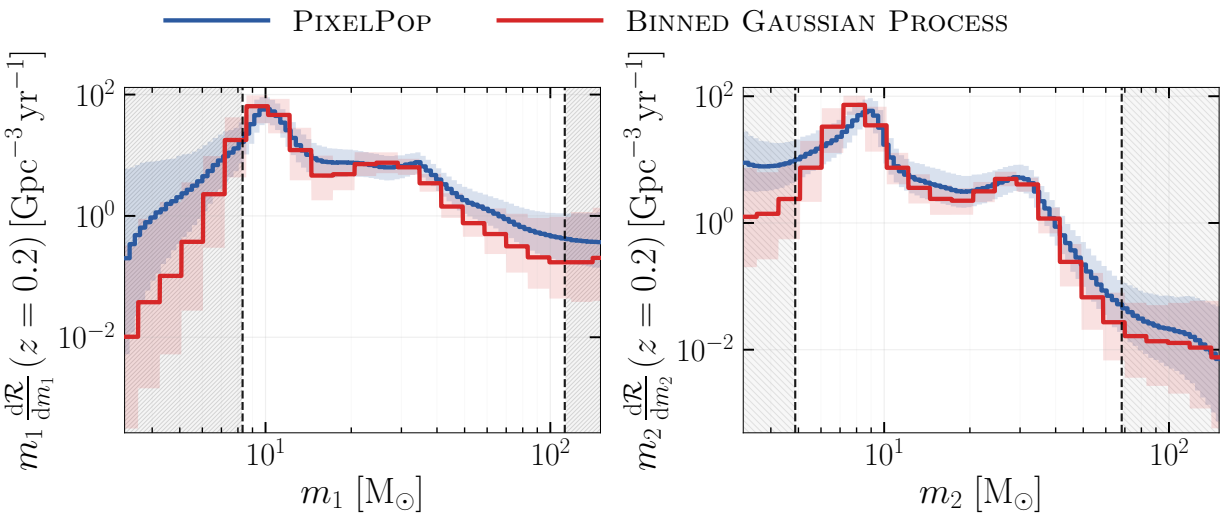

Figure 24. We compare the primary- and secondary-mass marginals from (m_1, m_2)-PIXELPOP and the $(m_1, m_2, \chi_{\rm eff})$ variant of BINNED GAUSSIAN PROCESS, marginalizing over all other parameters and evaluating at $z = 0$. The two approaches are in good agreement, showing the robustness of our results.

the $(m_1, m_2, \chi_{\rm eff})$ variant of BINNED GAUSSIAN PROCESS. While the two approaches differ in their dimensionality and smoothing assumptions, they provide an important cross-check of the inferred mass distribution. As shown in Fig. 24, the resulting m_1 and m_2 marginals are broadly consistent across the two methods.